

Mechanical design for satellite quantum communication

Mechanical design of 3U CubeSat

Luís Pedro Ramalho Barbosa

Thesis to obtain the Master of Science Degree in

Mechanical Engineering

Supervisors: Prof. Luís Alberto Gonçalves de Sousa
Prof. Emmanuel Zambrini Cruzeiro

Examination Committee

Chairperson: Prof. Paulo Rui Alves Fernandes
Supervisor: Prof. Luís Alberto Gonçalves de Sousa
Member of the Committee: Prof. Ricardo José Fontes Portal

December 2023

Declaration

I declare that this document is an original work of my own authorship and that it fulfills all the requirements of the Code of Conduct and Good Practices of the Universidade de Lisboa.

Acknowledgments

Foremost, I want to thank my family for supporting me throughout my academic journey in mechanical engineering, from my bachelor's to my master's degree. I couldn't have done it without them.

I'm also grateful to my dissertation supervisors, Prof. Luís Sousa and Prof. Emmanuel Cruzeiro, for their guidance, knowledge, and insights.

I want to give a special thanks to Ph.D. student Pedro Mendes for helping me with the quantum communication technical requirements, and to the ISTSat-1 team for giving me a great starting point for my project.

Finally, I want to thank all my friends who have helped me grow throughout my life and academic journey. Your support has been invaluable.

Thank you all!

Abstract

In the current era of increasing CubeSat space launches, traditional communication systems that rely on radio frequency are becoming inadequate for transmitting large amounts of data securely and quickly. Quantum communications systems offer a much more capable, faster, and secure way of transferring data cost-effectively.

The primary objective of this thesis is to design a 3U CubeSat and evaluate the feasibility of using commercial off-the-shelf components in a 3U CubeSat structure for a quantum communication downlink experiment between space and Earth. The quantum communication system is developed and provided by the Quantum Photonics Laboratory (QuLab) of Instituto de Telecomunicações - Lisboa.

The CubeSat's preliminary design has been created and analysed with a specific focus on the structural design. The integrity and stability of the CubeSat during launch have been evaluated, and multiple parts have been designed to fit the quantum communication optical system. The precise alignment of the dichroic mirrors and lasers is crucial for the system's successful operation.

Furthermore, Finite Element Analysis tools have been utilized to conduct stress, modal, and random vibration analyses to determine the mechanical behaviour of the CubeSat and identify potential weak spots. The preliminary design has successfully passed the static analysis loading, with all stresses being below the materials' yield stress. The modal analysis predicted a first resonance frequency of 283,66 Hz, which is above the minimum required by the launching entity of 115 Hz. Due to hardware limitations, the random vibration analysis was conducted only for the Z-axis, and the maximum stress obtained was well below the material's yield strength.

Keywords

CubeSat; Modal analysis; Quantum communication; Random Vibration analysis; Static analysis;

Resumo

Na era atual dos crescentes lançamentos de CubeSat's para o espaço, os sistemas de comunicação tradicionais que dependem de radiofrequência estão a tornar-se inadequados para transmitir grandes quantidades de dados com segurança e rapidez. Os sistemas de comunicação quântica oferecem uma maneira mais eficaz, rápida e segura de transferir dados com boa relação custo-benefício.

O principal objetivo desta dissertação é projetar um CubeSat 3U e avaliar a viabilidade de usar componentes "off-the-shelf" num CubeSat 3U para a demonstração de comunicação quântica entre o CubeSat no espaço e a Terra. O sistema de comunicação quântica no qual esta dissertação se baseia, foi elaborado e fornecido pelo Quantum Photonics Laboratory (QuLab) do Instituto de Telecomunicações - Lisboa.

O projeto preliminar do CubeSat foi criado e analisado com foco específico no projeto estrutural. A integridade e estabilidade do CubeSat durante o lançamento foram avaliadas e várias peças foram projetadas para se adequarem ao sistema ótico de comunicação quântica. O alinhamento dos vários espelhos e 'lasers' é crucial para a operação bem-sucedida do sistema.

Além disso, ferramentas de análise de elementos finitos foram utilizadas para realizar análises estruturais, modais e vibrações aleatórias para determinar o comportamento mecânico do CubeSat e identificar potenciais pontos fracos. O projeto preliminar passou com sucesso no carregamento da análise estática, com todas as tensões abaixo da tensão de cedência dos vários materiais. A análise modal previu uma primeira frequência de ressonância de 283,66 Hz, valor acima do mínimo exigido pela entidade lançadora de 115 Hz. Devido a limitações de hardware, a análise de vibrações aleatórias só foi realizada para o eixo Z, sendo que a tensão máxima obtida é inferior à tensão de cedência do material.

Palavras Chave

CubeSat; Análise Modal; Comunicação quântica; Análise de Vibrações Aleatórias; Análise estática

Contents

1	Introduction	1
1.1	Motivation	2
1.2	Satellites overview	3
1.2.1	CubeSats	4
1.2.2	Existing quantum communication missions	6
1.3	ISTSat-1	7
1.4	Overview of QuantSat-PT mission	8
1.5	Thesis objectives and outline	9
1.5.1	Objectives and Methodology	9
1.5.2	Thesis Outline	10
2	Literature review	11
2.1	State-of-the-art	12
2.1.1	Monocoque Construction	13
2.1.2	Modular Frame Designs	14
2.1.3	Custom structures	14
2.2	Finite Element Analysis	15
2.3	Static analysis	16
2.4	Modal analysis	16
2.5	Random vibrations' analysis	18
2.6	Fasteners	20
3	Design Requirements and Constraints	21
3.1	Mission specific requirements	22
3.2	Structural requirements	22
3.3	Launch and deployment constraints	24
4	Structural design	25
4.1	Design approach	26
4.2	Final design	28

4.2.1	Materials	29
4.2.2	Main structure	31
4.2.3	ISTSat-1 payload	32
4.2.4	Quantum communication payload	34
4.2.5	Dichroic mirror, FSM, QuadCell & Collimator	35
4.2.6	Lasers	36
4.2.7	Camera and Telescope	36
4.2.8	Reaction Wheels	37
4.2.9	FPGA and Reaction Wheels control PCBs	38
4.2.10	Solar panels and antennas	38
4.2.11	Fasteners	40
4.2.12	Center of Gravity and Moments of Inertia	41
5	Finite Element Analysis	42
5.1	Model idealization	43
5.1.1	Main structure idealization	44
5.1.2	PCB stack and other PCBs idealization	45
5.1.3	Idealized model	46
5.2	Materials	47
5.3	Loads and Boundary conditions	48
5.3.1	Restraints	48
5.3.2	Loads	49
5.4	Mesh generation	49
5.4.1	Convergence study	51
5.5	Static analysis	55
5.6	Modal analysis	59
5.6.1	Free-Free configuration	60
5.6.2	Hard-Mounted configuration	61
5.7	Random vibrations analysis	63
6	Conclusions	66
6.1	Conclusions	67
6.2	Achievements	68
6.3	Future Work	68
	Bibliography	68
A	Static analysis negative orientation (-x,-y,-z)	73

B Modes - Hard mounted	77
C Remote loads	85
D Technical drawing	87

List of Figures

1.1	Sputnik 1	3
1.2	CubeSat family	4
1.3	Poly-PicoSatellite Orbital Deployer	5
1.4	Nanosatellites launches by type	5
1.5	QUBE-II (left) and QUBE-I (right)	6
1.6	NanoBob Computer Aided Design (CAD)	7
1.7	ISTSat-1	8
1.8	Quantum Communication components layout	9
2.1	3D printed carbon fiber composite CubeSat frame	13
2.2	Pumpkin “chassis walls” CubeSat structure	13
2.3	EnduroSat 3U CubeSat structure	14
2.4	Mass-spring system	16
2.5	Mass-spring-damper system	17
2.6	Sample Acceleration Spectral Density (ASD) and Normal distribution plots	19
3.1	NASA General Environmental Verification Standard (GEVS)	24
4.1	2U CubeSat iteration	26
4.2	3U CubeSat iteration	27
4.3	3U CubeSat iteration with the improved optical system and lasers	27
4.4	3U Quantum Communication CubeSat CAD	28
4.5	CubeSat partially exploded view	29
4.6	Quantum Communication Payload	29
4.7	CubeSat main structure	32
4.8	Upgraded ISTSat-1 Printed Circuit Board (PCB) Stack (old on the left and new on the right)	32
4.9	Detailed PCBs	33
4.10	Quantum Communication 1st & 2nd stages section views	34

4.11 Dichroic mirror (a), Fast Steering Mirror (FSM) (b), QuadCell (c) & Collimator (d) assemblies	35
4.12 1350 & 1550 nm Laser assemblies	36
4.13 Camera and Telescope assembly	37
4.14 Reaction Wheels assembly	37
4.15 FPGA & Reaction Wheels PCBs	38
4.16 Solar panels	39
4.17 Very High Frequency / Ultra High Frequency (V/UHF) dipole antenna	39
4.18 ISO 7046 and ISO 7045 fasteners	40
4.19 CubeSat Center of Gravity (CoG)	41
5.1 Original vs idealization	43
5.2 Main structure idealization (removed fillets, simplified countersunk holes and delimited area for roller/slider fixture)	44
5.3 Dichroic mirror (a), FSM (b), QuadCell (c) & Collimator (d) assemblies idealization	45
5.4 ISTSat-1 upgraded PCB stack simplification (from solid to shell elements on PCBs, PC104 connector idealization)	46
5.5 Idealized model	47
5.6 Considered boundary conditions (yellow faces fixed and blue faces roller/slider)	49
5.7 Initial mesh	51
5.8 Free-Free 7th Mode Frequency convergence	52
5.9 Hard-Mounted 1st Mode Frequency convergence	53
5.10 Mesh refinement around the middle hole in Rib-3 (from left to right)	53
5.11 von Mises stress convergence around the middle hole in Rib 3	54
5.12 Idealized converged mesh	55
5.13 CubeSat Static loading X-axis von Mises stress	56
5.14 CubeSat Static loading X-axis displacement	56
5.15 CubeSat Static loading Y-axis von Mises stress	57
5.16 CubeSat Static loading Y-axis displacement	57
5.17 CubeSat Static loading Z-axis von Mises stress	58
5.18 CubeSat Static loading Z-axis displacement	58
5.19 Free-Free - 7th vibration mode	61
5.20 Hard-Mounted - 1st vibration mode	62
5.21 Effective mass participation factor	63
5.22 CubeSat Random Vibrations loading Z-axis RMS von Mises stress	64
5.23 CubeSat Random Vibrations loading Z-axis RMS displacement	64

A.1	CubeSat Static loading -X-axis von Mises stress	74
A.2	CubeSat Static loading -X-axis displacement	74
A.3	CubeSat Static loading -Y-axis von Mises stress	75
A.4	CubeSat Static loading -Y-axis displacement	75
A.5	CubeSat Static loading -Z-axis von Mises stress	76
A.6	CubeSat Static loading -Z-axis displacement	76
B.1	Mode 2 - 310,69 Hz	77
B.2	Mode 3 - 318,50 Hz	78
B.3	Mode 4 - 330,85 Hz	78
B.4	Mode 5 - 344,44 Hz	79
B.5	Mode 6 - 377,49 Hz	79
B.6	Mode 7 - 399,52 Hz	80
B.7	Mode 8 - 401,54 Hz	80
B.8	Mode 9 - 415,78 Hz	81
B.9	Mode 10 - 493,29 Hz	81
B.10	Mode 11 - 496,92 Hz	82
B.11	Mode 12 - 500,30 Hz	82
B.12	Mode 13 - 504,81 Hz	83
B.13	Mode 14 - 515,87 Hz	83
B.14	Mode 15 - 523,39 Hz	84

List of Tables

1.1	Types of satellites categories by size and weight	3
1.2	CubeSat Configurations	4
3.1	Center of gravity locations measured from CubeSat geometric center	23
3.2	Fundamental frequencies and Quasi Static loads for CubeSats according to Ariane 6 User's Manual	24
3.3	NASA GEVS	24
4.1	Recommended materials by CubeSat Design Specification (CDS)	30
4.2	Selected materials	31
4.3	Parts description	35
4.4	Fasteners types, sizes, lengths, materials, preload forces, and required torque	40
4.5	Center of gravity with respect to the geometric center	41
4.6	Moments of inertia properties	41
5.1	FE model materials' mechanical properties	48
5.2	Mesh Element Type, Material, and Thickness for each component	50
5.3	Free-Free 7th Mode Frequency convergence	52
5.4	Hard-Mounted 1st Mode Frequency convergence	53
5.5	von Mises stress convergence around the middle hole in Rib 3	54
5.6	Static loading maximum stresses and displacements	59
5.7	Minimum Factor of Safety	59
5.8	Fundamental modes in free-free configuration	60
5.9	Fundamental modes in hard-mounted configuration	61
C.1	Remote loads	86

List of Symbols

Greek symbols

α	Coefficient of thermal expansion
ϵ	Strain
ρ	Density
σ_P	Proof strength
σ_u	Ultimate strength
σ_y	Yield strength
τ	Shear strength
ν	Poisson's ratio
ω	Angular frequency

Roman symbols

A	Area
c	Damping coefficient
$[C]$	Damping matrix
d	Diameter
E	Elastic modulus
F	Force
F_i	Preload force
f	Frequency
G	Shear modulus
k	Stiffness
$[K]$	Stiffness matrix
m	Mass
$[M]$	Mass matrix
p	Pitch
T	Torque
t	Time
$[u]$	Nodal displacement vector
X	Amplitude
x	Position
\dot{x}	Velocity
\ddot{x}	Acceleration

Acronyms

ADCS	Attitude Determination and Control System
ADS-B	Automatic Dependent Surveillance - Broadcast
ASD	Acceleration Spectral Density
CAD	Computer Aided Design
Cal Poly	California Polytechnic State University
CNC	Computer Numerical Control
CoG	Center of Gravity
CDS	CubeSat Design Specification
COM	Communications Processor and Data Storage
CTE	Coefficient of Thermal Expansion
COTS	Commercial off-the-shelf
DoF	Degree of Freedom
EOAM	Eletro-optic Amplitude Modulator
EOPM	Eletro-optic Phase Modulator
EPS	Energy Power System
ESA	European Space Agency
FE	Finite Element
FEA	Finite Element Analysis
FEM	Finite Element Method
FYS!	European Fly Your Satellite!
FPGA	Field Programmable Gate Array
FR-4	Flame Retardant Glass Epoxy Laminate

FSM	Fast Steering Mirror
GEVS	General Environmental Verification Standard
ISS	International Space Station
LEO	Low Earth Orbit
LVE	Launch Vehicle Entity
LV	Launching vehicle
MDOF	Multi Degree of Freedom
NASA	National Aeronautics and Space Administration
OBC	On-Board Computer
PA	Passive Attenuator
PC	Polarization controller
PL	Payload ADS-B
PBT	Polybutylene terephthalate
PCB	Printed Circuit Board
P-POD	Poly-Picosatellite Orbital Deployer
PSD	Acceleration Power Spectral Density
PDF	Probability Density Function
QuLab	Quantum Photonics Laboratory
QUESS	Quantum Experiments at Space Scale
QUBE	Quantum Undertaking with a Bremen Expedition
QKD	Quantum Key Distribution
QRNG	Quantum Random Number Generator
RF	Radio Frequency
RMS	Root Mean Square
SDOF	Single Degree of Freedom
SS	Stainless Steel
SSDL	Stanford University's Space Systems Development Laboratory
TTC	Telemetry, Tracking and Communications
V/UHF	Very High Frequency / Ultra High Frequency

1

Introduction

Contents

1.1 Motivation	2
1.2 Satellites overview	3
1.3 ISTSat-1	7
1.4 Overview of QuantSat-PT mission	8
1.5 Thesis objectives and outline	9

1.1 Motivation

In the vast expanse of space, the humble CubeSat stands tall as a messenger. Where radio waves once bridged worlds, quantum communication now weaves the fabric of an unbreakable cosmos.

In a world where information is the key to progress, the relentless pursuit of efficient and secure communication is an eternal endeavour. The use of quantum communication enables high-speed and secure data transmission, making it a promising technology for space exploration. It promises intrinsic security based on the laws of quantum physics.

Quantum Key Distribution (QKD) protocols enable two parties to produce a joint secret key either by sending quantum states from one end to the other, or by sharing a special type of quantum state, one which has the property of being entangled. A unique property of QKD is the ability to detect the presence of some third party trying to intercept/decipher its contents and if detected the communication is aborted [1].

The implementation of QKD in a CubeSat poses a great challenge given the size and budget limitations. QKD poses three primary obstacles: the need to integrate it with current infrastructure, the distance photons must travel, and the necessity of justifying its implementation. While the security of QKD is sound in theory, putting it into practice can prove challenging due to equipment imperfections [2]. The first mission to demonstrate QKD was done by Chinese mission Micius [3] as part of the **Quantum Experiments at Space Scale (QUESS)** mission. Other quantum communication CubeSats missions are under development such as Qube [4], Qube-II [5], NanoBob [6].

Historically, CubeSats have utilized **Radio Frequency (RF)** communication systems that possess limited bandwidth capabilities, ranging from 10 to 200 Mbps, which necessitate an expensive and lengthy licensing process. The overcrowded RF airwaves are also prone to interference, interception or jamming [7]. However, with the advent of quantum communication, a more advanced and efficient mode of communication has emerged.

Quantum communication uses a narrow optical beam, which results in minimal interference with ground systems, although climate conditions can easily affect the system's performance (presence of clouds). Additionally, this mode of communication is not regulated, providing a more cost-effective and streamlined solution for CubeSat communication needs.

The motivation behind developing a Quantum communication CubeSat is to empower a new high-speed, secure data transmission that improves global communication infrastructures. In the form of proof-of-concept **Commercial off-the-shelf (COTS)** optics components and a CubeSat structure designed in-house.

1.2 Satellites overview

Satellites are man-made objects that orbit celestial bodies, such as planets and stars. They serve various purposes, such as scientific research (exploration of space and Earth), weather monitoring, communication, and navigation. The first artificial satellite launched into low earth orbit was Sputnik 1 (figure 1.1), on October 4th 1957 by the Soviet Union at the height of the space race between the USA and the Soviet Union (during Cold War) [8].

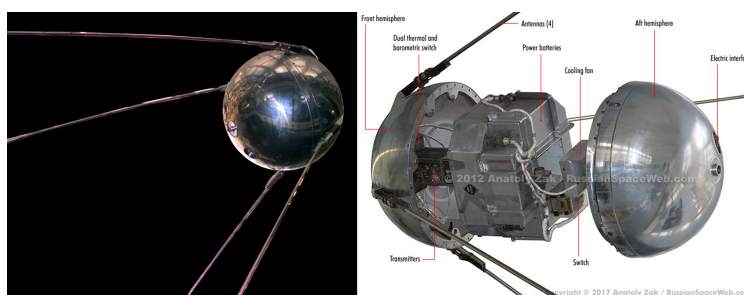


Figure 1.1: Sputnik 1 [9] [10]

Developing and deploying a standard satellite is a challenging and expensive process that only some parties are capable of performing. A conventional satellite is usually quite big and complex. As a result, satellite designers must make a trade-off between the satellite's capabilities, mission requirements, and the available budget. This delicate interplay between size, capabilities, and costs drives innovation in satellite design, with engineers striving to maximize functionality while staying within budgetary limits. There are multiple types of satellite categories concerning size, and weight as depicted in the table 1.1

Table 1.1: Types of satellites categories by size and mass [11]

Class	Mass (kg)
Femto	0.01 - 0.09
Pico	0.1 - 1
Nano	1.1 - 10
Micro	11 - 200
Mini	201 - 600
Small	601 - 1200
Medium	1201 - 2500
Intermediate	2501 - 4200
Large	4201 - 5400
Heavy	5401 - 7000
Extra-Heavy	>7001

1.2.1 CubeSats

Underlying the high cost and deployment times of conventional satellites, in 1999 Prof. Jordi Puig-Suari at California Polytechnic State University (Cal Poly), San Luis Obispo, and Prof. Bob Twiggs at Stanford University's Space Systems Development Laboratory (SSDL) collaborated in the creation of new class nanosatellites widely known as CubeSats developing a new standard called **CubeSat Design Specification (CDS)** [12]. The intent of the CubeSat project was to reduce cost and development time and increase accessibility to space, providing students and the overall academic community with hands-on experience in the design, manufacture and testing of space system hardware.

A CubeSat is a class of satellites that adopt a standard size and form factor, which unit is defined as 'U'. The unit 'U' is a CubeSat with 10x10x10 cm, CubeSats come in multiple configurations of stacked 'U' units as shown in table 1.2 and figure 1.2.

Table 1.2: CubeSat Configurations [12]

U configuration	Mass (kg)
1U	2.00
1.5U	3.00
2U	4.00
3U	6.00
6U	12.00
12U	24.00

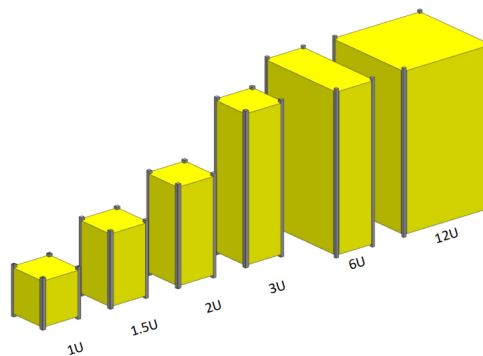


Figure 1.2: CubeSat family [12]

CubeSats are typically launched using Poly-Picosatellite Orbital Deployers (P-PODs), see figure 1.3. These deployers serve as a consistent platform for CubeSat launches. They are attached to launch vehicles and transport CubeSats to orbit. Once the launch vehicle receives the appropriate signal, the CubeSats are deployed. Some CubeSats are deployed directly by primary payloads, while most are launched from a vehicle or the International Space Station (ISS).

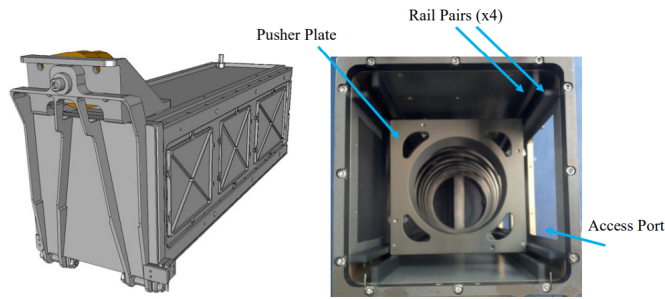


Figure 1.3: Poly-PicoSatellite Orbital Deployer [12]

By May 2023, 2105 CubeSats had already been launched [13], and even though the COVID-19 pandemic (2019-2020) caused a brief decline, there's still a noticeable rise in CubeSat launches (figure 1.4). It's evident that the popularity of CubeSats has been increasing in recent years, with both academic institutions and companies building multiple types of CubeSats for various purposes. The industry has also seen the emergence of companies offering commercial solutions for CubeSat structure and hardware COTS components.

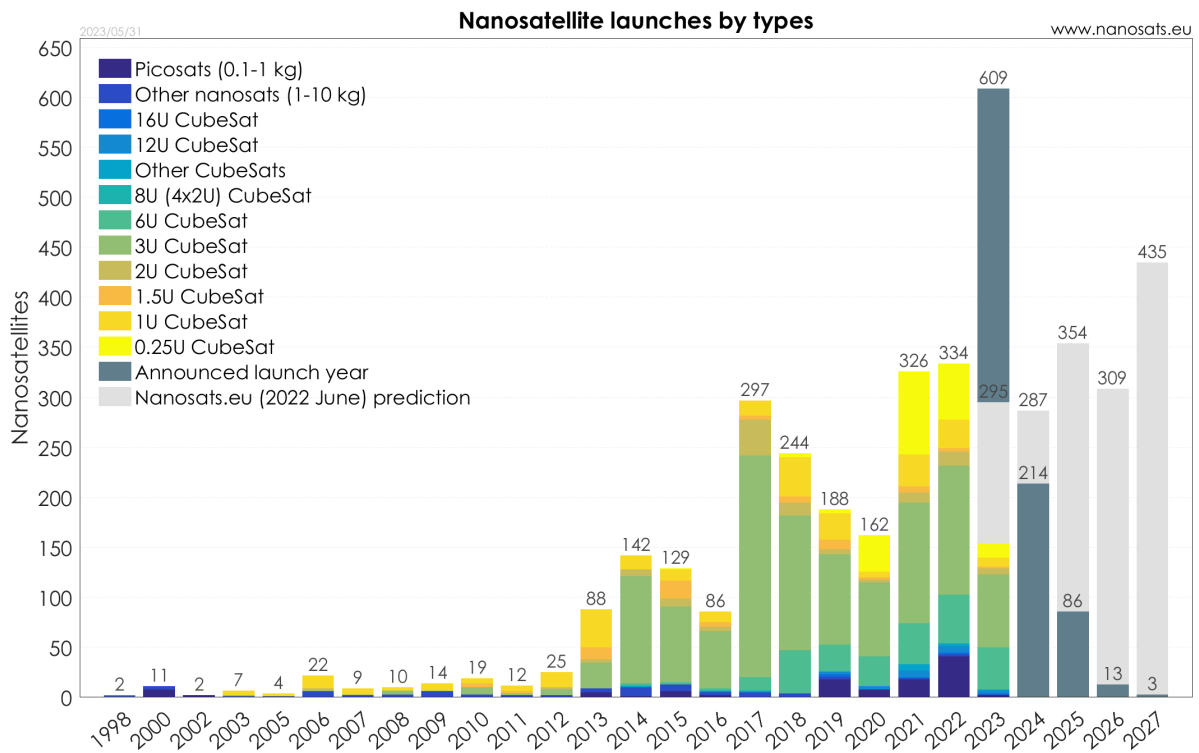


Figure 1.4: Nanosatellites launches by type (source: Nanosats database [13])

1.2.2 Existing quantum communication missions

Quantum communication systems have already demonstrated their capabilities in ground and space. In 2016, China launched the Micius mission [3], which is a quantum communication satellite named after the Chinese philosopher Mozi from the 5th century BC. The mission successfully demonstrated that QKD could be transmitted over long distances. The quantum keys were transmitted to ground stations in China and Austria, which were 1200 kilometres apart. The success of the Micius mission has opened up new possibilities for the development of a global quantum communications network. This network could be used to secure sensitive data, government communications, and financial transactions.

Quantum communication CubeSats under development:

The Quantum Undertaking with a Bremen Expedition (QUBE) mission [4] (figure 1.5), a European project, aims to create and launch a 3U CubeSat for conducting QKD experiments. The main objective is to examine the feasibility of QKD in space and its performance under the influence of the space environment. The launch is expected to take place in 2023.

The QUBE-II [5] (figure 1.5) is a continuation of the QUBE project, a European initiative that aims to launch a CubeSat to conduct quantum key distribution experiments. The CubeSat, which is scheduled to launch in 2024, is a 6U vessel that will transport two QKD sender modules and a quantum random number generator. The mission's goal is to enhance QKD capabilities in space, explore secure communication between satellites, develop novel QKD technologies, and promote awareness of quantum communications. The findings of the project will pave the way for future applications in the field of quantum communications.



Figure 1.5: QUBE-II (left) and QUBE-I (right) [5]

The NanoBob [6] (figure 1.6) mission is a 12U CubeSat project aimed at demonstrating QKD experiments between a CubeSat and a ground station. It will carry a Quantum Random Number Generator (QRNG) and a single-photon detector. The mission's success will be instrumental in developing a global quantum communications network. The NanoBob mission is a collaboration between academia and industry and highlights the growing interest in quantum communications and its potential applications.

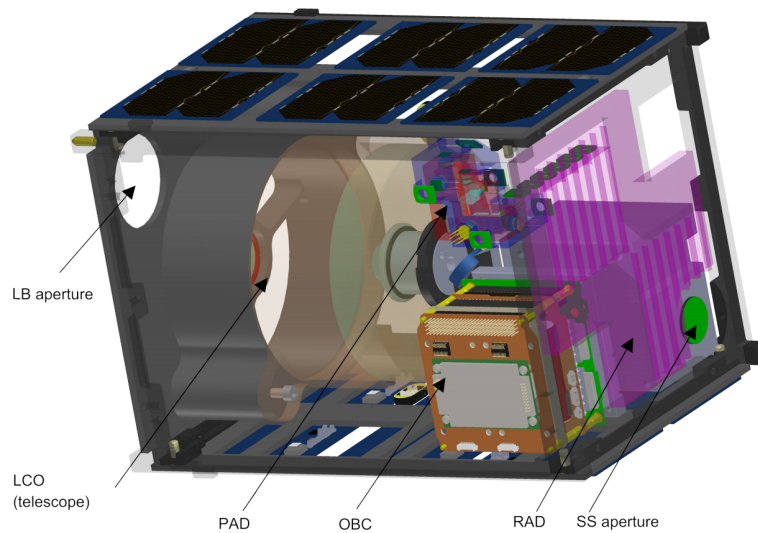


Figure 1.6: NanoBob Computer Aided Design (CAD) [6]

1.3 ISTSat-1

ISTSat-1 is an innovative CubeSat that has been developed by Portugal's ISTSat team. It is a significant milestone as it is the first CubeSat of its kind to be developed by an academic institution in the country. The CubeSat has been designed with a compact Automatic Dependent Surveillance - Broadcast (ADS-B) receiver and antenna that can effectively track commercial aircraft positions and status beyond line-of-sight communications.

The CubeSat is designed to work seamlessly with a rail design deployer, such as the P-POD and has multiple subsystems that are compacted in a Printed Circuit Board (PCB) stack supported by four axes to the main CubeSat structure. It is equipped with solar panels on all faces, except for the one where the ADS-B antenna is placed. Additionally, there is an Very High Frequency / Ultra High Frequency (V/UHF) antenna for RF communication underneath one of the solar panels.

Extensive testing campaigns have taken place throughout 2020-2023 to ensure the CubeSat is fully functional. It is expected to launch in December 2023, along with other CubeSats participating in the European Fly Your Satellite! (FYS!) project. The flight will hitch a ride on the new European Space

Agency (ESA)'s Ariane 6 maiden flight.

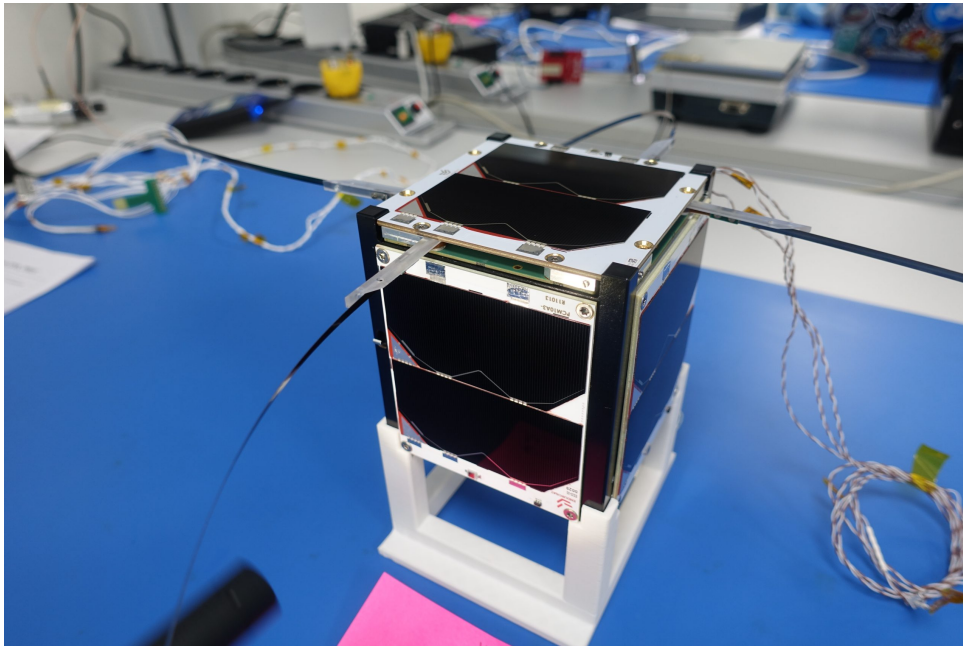


Figure 1.7: ISTSat-1 [14]

1.4 Overview of QuantSat-PT mission

The QuantSat-PT [15] initiative is a significant first step towards Portugal's ambitious goal of establishing quantum communication satellites and ground stations. By doing so, the country will attain self-reliance in technologies that support its sovereignty and participate in the upcoming European Quantum Communication Infrastructure. The mission's primary objective is to demonstrate a quantum communication system downlink using COTS equipment to point a 1550 nm laser with data to a ground station yet to be built. The quantum communication system is made up of two areas: the fiber optics area and the optical area.

The fiber optics area is composed of an Field Programmable Gate Array (FPGA) and various other components that work together to modify and regulate the downlink signal created by the 1550 nm laser. After passing through additional components like the Electro-optic Amplitude Modulator (EOAM), Polarization controller (PC), Electro-optic Phase Modulator (EOPM), Passive Attenuator (PA), and collimator, the signal is then sent to the optical area. Within this area, the beam is expanded and filtered through multiple dichroic mirrors to specific wavelengths. Finally, the signal is precisely aligned by a Fast Steering Mirror (FSM) and transmitted to the ground station.

Figure 1.8 displays a simplified diagram of the quantum communication system, illustrating the routes taken by the downlink and uplink beams. The CubeSat relies on a 1350 nm laser beam and a camera to

align with the ground station. The camera detects the ground station beam, and together with the laser beam, provides feedback for the FSM through a closed-loop control system. The CubeSat's pointing is achieved by utilizing reaction wheels in the Attitude Determination and Control System (ADCS).

Quantum communication can occur during both day and night, but it always depends on the climatic conditions and the visible window period to the ground station, which is approximately 10 minutes. Besides the quantum communication system, there is also a backup RF system to maintain a communication link with the ground station in case the quantum communication system fails.

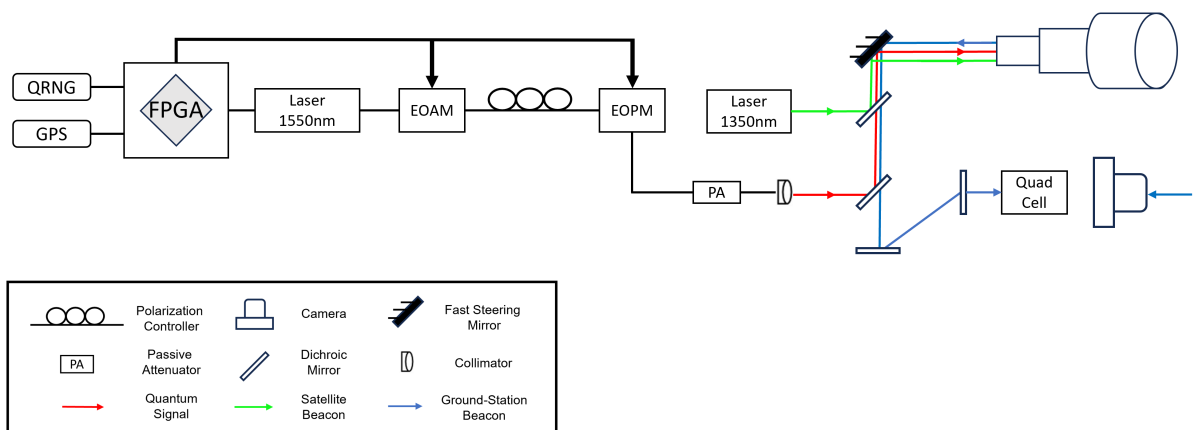


Figure 1.8: Quantum Communication components layout

1.5 Thesis objectives and outline

1.5.1 Objectives and Methodology

The objective of this thesis is to create a prototype mechanical design for a Quantum Communication 3U CubeSat. It should be noted that the quantum communication design is still being developed, and the mechanical design provided is only a preliminary look at what the final CubeSat may entail. This is due to the fact that there are numerous undefined constraints and components that have yet to be specified. The mechanical design and analysis will be based on the existing quantum communication concept idea developed by the Quantum Photonics Laboratory (QuLab) of Instituto de Telecomunicações - Lisboa.

To begin, we will assess the current State of the Art of CubeSat structures before delving into the primary design considerations and trade-offs. Ultimately, an initial detailed CAD model will be created using SolidWorks. Finally, a simplified Finite Element Method (FEM) model will be constructed based on the preliminary design and simplification assumptions.

The simplified FEM model will undergo Modal, Static, and Random Vibrations' analysis using the SolidWorks Simulation package, an integrated Finite Element Analysis (FEA) tool in SolidWorks.

The decision to use SolidWorks was based on the current stage of the design process, which requires seamless integration with other software packages to enable swift iterations of the design. This approach can significantly streamline the design process and minimize the time and inconvenience of transferring models between different programs, which can frequently result in mating errors and other challenges. It's critical to acknowledge that other FEA software may be utilized during the final design phase for improved analysis tuning and outcomes.

However, it's important to keep in mind that the design inputs directly drive the outputs we get from the model. This applies to all FEA tools.

In summary, the goals of this thesis are:

- Create and develop the preliminary design of a 3U CubeSat for Quantum Communication, incorporating the existing IST-Sat1 [16] mission (in one of the U units);
- Create a Finite Element (FE) model and perform a Modal, Static, and Random Vibrations analysis;
- Deliver a validated FE model for future design iterations and possible experimental test campaigns;

1.5.2 Thesis Outline

This thesis is organized as follows:

In **Chapter 1**, the motivation, an introduction to CubeSats and mission overview is presented.

In **Chapter 2**, the State of the Art and a literature review about the main concepts behind the mechanical design and analysis using FEA tools.

In **Chapter 3**, the design requirements and constraints set by mission goals and relevant standards.

In **Chapter 4**, the CubeSat mechanical design from main frame to internal components.

Chapter 5, focuses on the structural analysis (Static, Modal, Random Vibrations) using a FEM tool.

Chapter 6, summarizes the work completed, main achievements and challenges.

2

Literature review

Contents

2.1 State-of-the-art	12
2.2 Finite Element Analysis	15
2.3 Static analysis	16
2.4 Modal analysis	16
2.5 Random vibrations' analysis	18
2.6 Fasteners	20

This chapter provides a comprehensive overview of the state-of-the-art and theoretical background needed for the scope of this thesis. The topics covered in the theoretical background are based on [17–20].

2.1 State-of-the-art

When creating CubeSats, it is crucial to consider their ability to endure the harsh conditions of space, such as extreme temperatures, radiation, micrometeoroids, and the stresses and vibrations of launch. The advancement of CubeSat technology, through the development of new materials, manufacturing techniques, and technologies, is constantly evolving to enhance its capabilities and affordability. Standardization of CubeSats simplifies their production and deployment, allowing for the creation of common subsystems and components like ADCS and communication systems. This results in a uniform main structure design and module compatibility, with companies concentrating on creating commercial off-the-shelf (COTS) parts like chassis, antennas, reaction wheels, and solar panels.

Currently, CubeSats are constructed using three methods: commercially available structures (COTS), custom-machined structures, or 3D printed components [21]. COTS structures are tailored to the CubeSat market, simplifying mission development when subsystems, payload requirements, and complexity align with the intended design. Custom-machined structures provide greater flexibility for designing mission-specific systems and payloads. Generally, commercially available structures are designed for low-Earth orbit applications with limited mission durations, and radiation protection from the Van Allen Belts is the only shielding requirement.

CubeSats use lightweight materials such as aluminium alloys or composites to minimize launching costs. The development of 3D printing has revolutionized CubeSat design and manufacturing, enabling the creation of complex geometries that were impossible with traditional techniques [22]. This also allows for the production of hollow and composite material parts. Figure 2.1 shows a composite CubeSat frame with topological optimization. This composite frame weights only 200,6 grams, which is 49,7% reduction when compared to aluminium ones produced by traditional manufacturing methods.

While the mechanical design of the main CubeSat structure adheres to strict standards, there is still room for creativity in the design, choice of materials, and manufacturing methods used. Several companies now offer CubeSat primary structures, machined from aluminium alloys like 6061 or 7075, with various mounting locations for components to provide spacecraft configuration flexibility. The most common frames are 1U, 3U, and 6U, with 12U frames becoming more widely available.

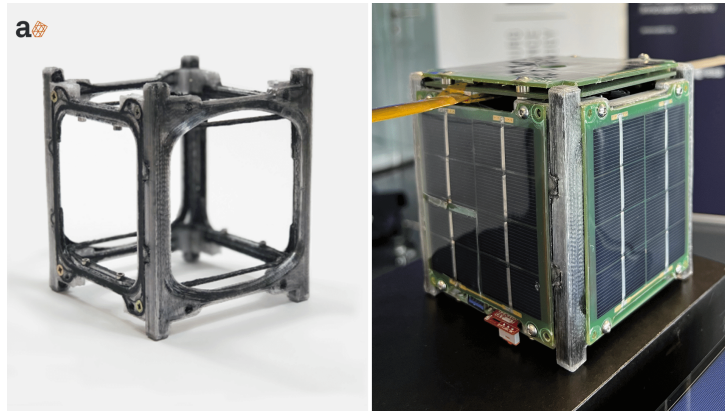


Figure 2.1: 3D printed carbon fiber composite CubeSat frame [22]

2.1.1 Monocoque Construction

Monocoque structures bear weight, have a long history in aviation and are also used in small spacecraft designs for various purposes. These include maximizing internal space, increasing volume for heat sinks or sources, and allowing for more mounting points. Monocoque construction is widely used, and "extruded" designs can be easily created through Computer Numerical Control (CNC) machining, water jet, or laser cutting.

Pumpkin was the first to use sheet metal for CubeSat structures in 2000. For many applications, this unique approach still reigns supreme in terms of strength-to-weight ratio, internal volume available, simplicity in design, and minimal use of fasteners. The "core" of each structure, known as the Chassis Walls, is a single piece of folded and riveted precision sheet metal, and comes in various lengths [23] (figure 2.2).



Figure 2.2: Pumpkin "chassis walls" CubeSat structure [23]

2.1.2 Modular Frame Designs

Modular frames are the go-to choice for rapid deployment missions, thanks to their adaptable internal design that conforms to the CubeSat standard's external dimensions. This feature is particularly crucial when using a standardized and reusable dispenser for deploying the CubeSat. However, it's important to keep in mind that open frames are not ideal for high-radiation environments, limiting their use to low-Earth orbit. Furthermore, designers must consider the thermal mass requirements, given that modular frames are generally lightweight.

EnduroSat [24] developed CubeSat structures in sizes ranging from 1U to 8U. These structures are made of lightweight aluminium alloy and have a hard-anodized finish for corrosion resistance (figure 2.3). The 3U structure weighs 340g and costs €3600 for the version with cutouts for roller switches.



Figure 2.3: EnduroSat 3U CubeSat structure [24]

2.1.3 Custom structures

There has been a noticeable increase in the creation of small, tailor-made CubeSats that come with specific interface prerequisites. These prerequisites are mainly centred around the design of the payload. To ensure that the spacecraft stays safe, it is of utmost importance to have safety switches like "remove before flight" pins and footswitches. Furthermore, the spacecraft must be switched off while in the deployment dispenser and follow other safety requirements such as anodized aluminium rails, specific weight, centre of gravity, and external dimensions for canister or dispenser deployment to be successful. Generally, the rideshare integrator provides these requirements for the specific dispenser that will be used with the launch vehicle, while the launch vehicle provider gives the launch vibrational conditions.

2.2 Finite Element Analysis

In the field of engineering, FEA is often utilized as a numerical tool to simulate how a part or assembly will behave under specific conditions. While analytical methods may work for simple shapes, more complex shapes require a complex mathematical model to accurately describe their behaviour. This is where numerical methods, such as the Finite Element Method, prove to be a valuable resource.

The FEM achieves this by dividing a complicated space or domain (model geometry) into small volumes (the finite elements) in accordance with the respective formulation. The discretization process, called 'meshing', converts the integral form into a set of matrix equations that can be solved using appropriate matrix algebra. The FEA workflow can be divided into the following steps [19]:

1. **Converting CAD geometry to FEA geometry:** CAD models are often quite detailed and need to be simplified in order to provide an efficient use of computational resources. Therefore, the model needs to be idealized by for example suppressing or deleting geometry details not relevant to the type of analysis of interest;
2. **Creating a mathematical model:** Defining Loads and restraints, material properties and type of analysis;
3. **Discretization:** The mathematic model is discretized into FE that are characterized by nodes with multiple Degree of Freedom (DoF);
4. **Solution:** FE equations are solved and results are ready to be analysed;
5. **Post-processing:** Convert highly detailed and complex solution output into a form that the user can understand (plots, animations, etc.) and possibly impact their decision-making;

By combining the resulting equations into a combination of FE referred to as the 'mesh', which consists of interconnected nodes compatible with each other, the whole domain behaves as a single structure, which can be analysed in its entirety. Each element's behaviour is fully characterized by its node displacements. The application of the principle of the minimum total potential energy leads to the formulation of the fundamental FEA equation:

$$[K][u] = [f] \quad (2.1)$$

where $[K]$ is the stiffness matrix, $[f]$ is the vector of nodal loads, $[u]$ is the unknown vector of nodal displacements.

2.3 Static analysis

Static analysis assumes that loads on a structure remain constant over time and that the structure's response to these loads is steady. This technique aims to determine the displacements, stresses, and strains of a structure when subjected to static loads. The approach assumes that all loads are gradually applied until they reach their maximum amplitude, at which point they remain constant. Inertial and damping forces are disregarded because they result in negligible accelerations and velocities. By solving equation 2.1 for the system, the displacements for all degrees of freedom can be determined.

2.4 Modal analysis

Modal analysis is a technique used to study the dynamic behaviour of a structure, it is helpful in determining a structure's natural frequencies, mode shapes, and damping factors. Natural frequencies indicate the frequencies at which the structure will vibrate in the absence of driving forces, while mode shapes represent the structure's shape at each natural frequency, and they are determined by the material properties and boundary conditions. Knowing the natural frequency of a system is crucial in preventing resonances that may eventually lead to catastrophic failure. Structures under resonant-frequency-loading conditions can fail as the force amplitude increases over time. There have been many catastrophic examples of this in history, with one famous example being the Tacoma Narrows Bridge collapse in 1940 [25]. Damping factors measure how quickly the structure will return to its original state after being disturbed. See Figure 2.4, which displays a one-directional mass-spring system, also known as a Single Degree of Freedom (SDOF) system.

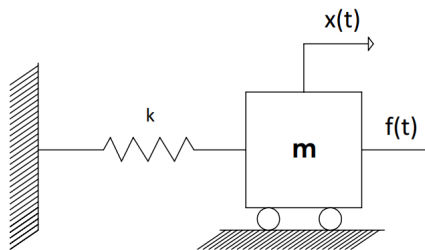


Figure 2.4: Mass-spring system

The application of Newton's Second Law to the system results in 2.2.

$$m\ddot{x} + kx = f(t) \quad (2.2)$$

where \ddot{x} is the acceleration of the mass, and it is equal to the second derivative of x with respect to

time, K is the stiffness of the spring.

When a mass is displaced and released, it will vibrate with decreasing amplitudes until it comes to a stop. This is called damping, caused by energy loss through friction and other effects. Viscous damping is when the damping force is proportional to velocity. Figure 2.5 depicts a damped SDOF system.

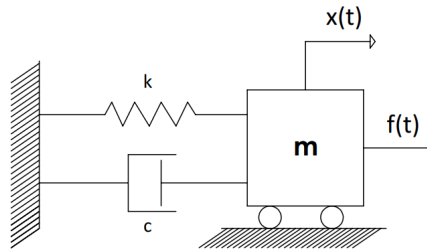


Figure 2.5: Mass-spring-damper system

In a Multi Degree of Freedom (MDOF) system, the equations of motion are expressed in matrix form. When damping is considered, the result is:

$$[M]\{\ddot{x}\} + [C]\{\dot{x}\} + [K]\{x\} = \{f(t)\} \quad (2.3)$$

where, M is the mass matrix, C the damping matrix and K the stiffness matrix

Modal analysis is concerned with the study of free and undamped vibrations. This refers to the case where there is no external excitation, i.e., $f(t) = 0$, and no damping, i.e., $[C] = 0$. As a result, equation 2.3 can be simplified to:

$$[M]\{\ddot{x}\} + [K]\{x\} = \{0\} \quad (2.4)$$

Considering that:

$$x = X \sin(\omega t) \quad (2.5)$$

Equation 2.4 takes the form:

$$([K] - \omega^2[M])\{X\} = \{0\} \quad (2.6)$$

The equation 2.6 has a trivial solution, $\{X\} = \{0\}$ which signifies no movement. Instead, exploring non-zero solutions leads to an eigenvalue problem. By doing so, it becomes possible to determine the various modal frequencies and their corresponding modal shapes of vibration.

$$\det([K] - \omega^2[M]) = 0 \quad (2.7)$$

By solving equation 2.7, we can obtain the eigenfrequencies of the system, which represent the nat-

ural frequencies for each mode.

Note that the equation 2.6 has as many solutions as the number of DoF of the system, ω^2 is the eigenvalue, and X is the eigenvector.

The natural frequency in hertz (Hz) can be calculated with the eigenvalue as follows:

$$f = \frac{\omega}{2\pi} \quad (2.8)$$

The natural frequency of a SDOF system can also be calculated, knowing the system's stiffness and its mass by applying the following formula:

$$\omega_n = \sqrt{\frac{k}{m}} \quad (2.9)$$

where k is the system's stiffness and m its mass.

2.5 Random vibrations' analysis

Up until now, the excitations we've dealt with have been known in advance. These are examples of deterministic excitations, meaning we can predict their values exactly given a specific time.

However, many physical excitations are random and cannot be described with explicit time descriptions, common examples are rockets, earthquakes, aerodynamic forces, and rough roads and seas. The reactions to these excitations are unpredictable and therefore nondeterministic.

A stochastic process is a collection of random variables that describe a physical phenomenon, such as a function of time or frequency. Each record is unique, making it impossible to analyse every possible record. Instead, we describe the process using statistical properties. In a random vibration study, each load is a random process, and thus the response of a model to these loads is also a random process described statistically.

The autocorrelation function (equation 2.10) is a tool for measuring how a signal changes over time or how correlated it is at two different points in time. It applies to a random signal called $x(t)$, which is denoted as $R(t)$. This function calculates the correlation between the values in a dataset at different time intervals. It is determined by finding the expected value of the product of a random variable $x(t)$ and a time-shifted version of itself $x(\tau + t)$.

$$R(t) = x^2 = \lim_{T \rightarrow \infty} \frac{1}{T} \int_0^T x(\tau)x(\tau + t)d\tau \quad (2.10)$$

In many cases, the excitation vibrations go back and forth around zero, which means that the average

values, stress, and displacements are also zero. To overcome this problem, it is common to use Root Mean Square (RMS) values (shown in equation 2.11). The RMS value corresponds to one standard deviation of a normal distribution. The G_{rms} value is often used to indicate the total energy of a random vibration event and is a statistical metric that is useful for structural design and analysis purposes.

$$G_{rms} = \sqrt{\lim_{T \rightarrow \infty} \frac{1}{T} \int_0^T x^2 dt} \quad (2.11)$$

In order to analyse random vibrations, an Acceleration Power Spectral Density (PSD) is often used, as shown in equation (2.12). The PSD measures the power of a signal in relation to its frequency and is obtained by performing a Fourier transform of the autocorrelation function.

$$S_x(\omega) = \int_{-\infty}^{+\infty} R_x(\tau) e^{-i\omega\tau} d\tau \quad (2.12)$$

Through analysis of the PSD, we can identify the level of vibration energy present at varying frequencies. The figure shown in 2.6a is a frequently used PSD sample plot from National Aeronautics and Space Administration (NASA) General Environmental Verification Standard (GEVS) [26] for qualifying aerospace structures. The units of the PSD are $\frac{G^2}{Hz}$, and the shape of the graph indicates the average acceleration for each frequency. The area under the curve represents the RMS of the signal.

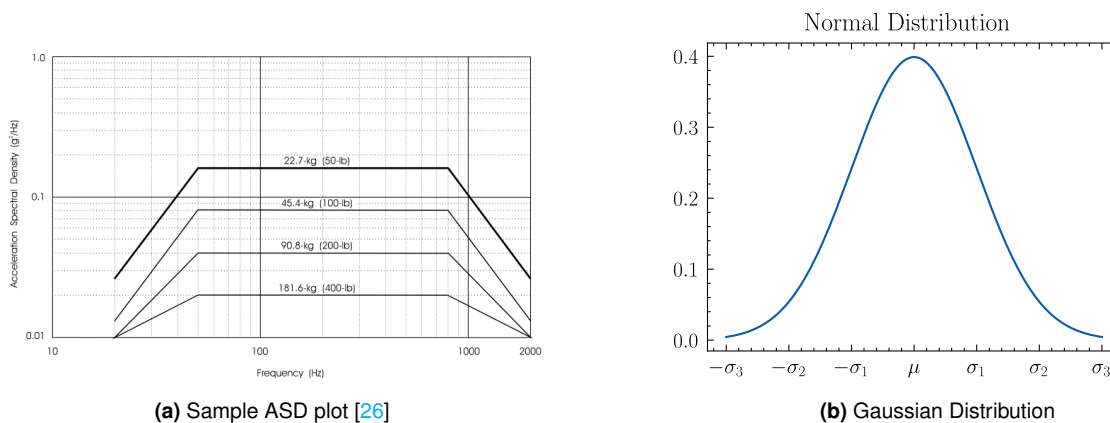


Figure 2.6: Sample Acceleration Spectral Density (ASD) and Normal distribution plots

Random vibrations exhibit magnitudes of acceleration, velocity, and displacement that follow a normal distribution, also known as a Gaussian distribution. The Probability Density Function (PDF) of this distribution is illustrated in Figure 2.6b, where the area under the curve corresponds to a probability of 1. The normal distribution is defined by two parameters: the mean, which represents the average value of the distribution, and the standard deviation, which measures the degree of dispersion in the distribution.

2.6 Fasteners

In order to connect multiple components, a fastener or bolt can be used. This connection can either be permanent through the plastic deformation of the fastener or non-permanent. When dealing with intricate structures like CubeSats, fasteners are often the primary method of joining. To ensure that the components remain secure during operation, it is essential to select and design the fasteners properly. A popular approach is to preload bolted joints with a torque specification, which helps these joints resist vibrations in the environment and prevents any unintentional overtightening that could damage the joint, component, or threads.

According to [20] the recommended preload force $F_i(N)$ for permanent joints is given by:

$$F_i = 0.9A_t\sigma_p \quad (2.13)$$

where A_t is the tensile area (m^2) of the bolt given by:

$$A_t = \frac{\pi}{16}(d_p + d_r)^2 \quad (2.14)$$

For ISO threads:

$$d_p = d_{nom} - 0.649519p \quad (2.15)$$

$$d_r = d_{nom} - 1.226869p \quad (2.16)$$

where d_{nom} is the nominal bolt diameter, d_p is the pitch diameter, d_r is the root diameter, p is the thread pitch, σ_p is the proof strength that can be obtained by consulting the SAE J1199-2013 standard [27] that defines the mechanical and material requirements for metric externally threaded steel fasteners. However, if unavailable, it can be approximated by:

$$\sigma_p = 0.85\sigma_y \quad (2.17)$$

where σ_y is the yield strength of the material.

The preload of a bolt is typically done by applying torque to the head or nut. This is because torque is easier to measure than applied force. The recommended torque $T(n.m)$ to be applied is given by the equation:

$$T = KF_id_{nom} \quad (2.18)$$

The value of K depends on the bolt material and size, with 0,2 being a commonly used value.

3

Design Requirements and Constraints

Contents

3.1 Mission specific requirements	22
3.2 Structural requirements	22
3.3 Launch and deployment constraints	24

The aim of this chapter is to clearly outline the requirements and limitations for creating the preliminary design of the 3U quantum communication CubeSat.

As mentioned in the section 1.4, the primary goal of this thesis is to develop a preliminary design for the CubeSat that includes the ISTSat-1 functionality and a new quantum communication system. During launch, CubeSats face a challenging environment, so they must be able to withstand various types of solicitations, such as quasi-static accelerations, sine and random vibrations, acoustic forces and shock. Typically, the design requirements are specified by the Launch Vehicle Entity (LVE), with CubeSat Design Specification (CDS) and Nasa General Environmental Verification Standard (NASA GEVS) being the main standards for CubeSats. If a CubeSat meets these standards, it is highly likely to be qualified for almost any LVE.

3.1 Mission specific requirements

The CubeSat design for the **QuantSat-PT** mission must meet specific requirements for successful deployment in space. The mission requirements are listed below:

- The CubeSat structure should adhere to the design approach used for the already developed ISTSat-1 CubeSat;
- The CubeSat structure must have a 3U configuration, with 2U for the quantum communication payload and 1U for the revised ISTSat-1 payload;
- The CubeSat's communication optics components must be mounted on sturdy supports to prevent optical misalignments and component damage;
- The new CubeSat requires an ADCS active pointing system that makes use of reaction wheels;
- The new CubeSat must include additional solar panels and batteries compared to the existing ones in ISTSat-1;
- The CubeSat quantum communication system must follow the layout depicted in figure 1.8;

3.2 Structural requirements

The CDS [12] establishes the fundamental guidelines for designing CubeSats. It offers direction on CubeSat design to guarantee the safe operation and deployment of the system. It's important to note that the CDS may have stricter requirements than the launch provider, meaning that a CubeSat compliant with the CDS will likely meet most launch provider requirements.

Below are some of the relevant requirements [12] for this CubeSat:

- All components must remain connected to the CubeSat during launch, ejection, and operation;
- The origin of the CubeSat coordinate system is located at the geometric center of the CubeSat;
- A 3U CubeSat shall not have a mass greater than 6 kg, as stated earlier in table 1.2;
- The CubeSat configuration and physical dimensions shall conform with technical drawing (see Appendix D);
- Components should not protrude yellow shaded sides more than 6.5 mm normal to the surface from the plane rail (see Appendix D);
- Deployable components must be constrained during launch (e.g.RF antennas);
- Rails should have a minimum width of 8.5 mm from the edge of the rail to the first protrusion;
- Rails should have a surface roughness less than 1.6 μm ;
- The CubeSat structure should be made from aluminium alloy (e.g. 7075, 6061, 6082, 5005 and 5052);
- CubeSat exteriors in contact with dispenser rails shall be hard anodized to prevent cold welding;

Note that the list provided should not be considered exhaustive, as there are many additional requirements stemming from this and other applicable standards.

Table 3.1 displays the permissible positions of the Center of Gravity (CoG) concerning the geometric center of the CubeSat. It is important to note that for a 3U CubeSat setup, the acceptable range for the location of the CoG is within ± 2 cm for both X and Y axes, and within ± 7 cm for the Z axis.

Table 3.1: Center of gravity locations measured from CubeSat geometric center [12]

U configuration	X Axis	Y Axis	Z Axis
1U	+ 2 cm / -2 cm	+ 2 cm / -2 cm	+ 2 cm / -2 cm
1.5U	+ 2 cm / -2 cm	+ 2 cm / -2 cm	+ 3 cm / -3 cm
2U	+ 2 cm / -2 cm	+ 2 cm / -2 cm	+ 4,5 cm / -4,5 cm
3U	+ 2 cm / -2 cm	+ 2 cm / -2 cm	+ 7 cm / -7 cm
6U	+ 4,5 cm / -4,5 cm	+ 2 cm / -2 cm	+ 7 cm / -7 cm
12U	+ 4,5 cm / -4,5 cm	+ 4,5 cm / -4,5 cm	+ 7 cm / -7 cm

3.3 Launch and deployment constraints

At the time of its launch, the CubeSat is subjected to a series of intense loads that result from rapid acceleration, vibrations, and high-energy shock impulses that occur during rocket separation. The CubeSat is required to endure these loads without incurring any damage to its structural integrity and internal components. As of now, there is no confirmed launch date or specific Launching vehicle (LV) for the CubeSat. However, the Ariane 6 has been proposed as a potential option. To ensure proper deployment, a standardized dispenser such as the P-POD will be utilized.

Basic CubeSat specifications can be found in the CDS, but the Ariane 6 User's Manual for Multi-Launch Service [28] provides specific information on minimum fundamental frequencies to prevent dynamic coupling and quasi-static loads for all axes (see table 3.2).

Table 3.2: Fundamental frequencies and Quasi Static loads for CubeSats according to Ariane 6 User's Manual [28]

Spacecraft Axis	Fundamental Frequencies	Quasi Static Loads
X_{PL}	> 115 Hz	$\pm 10,0$ g
Y_{PL}	> 115 Hz	$\pm 10,0$ g
Z_{PL}	> 115 Hz	$\pm 10,0$ g

In order to ensure the CubeSat's resilience during launch, the payload is engineered to withstand random vibration loads in accordance with NASA's GEVS guidelines. For spacecraft weighing under 22,7 Kg, the general random vibration test levels for GEVS qualification can be found in Figure 3.1 and in table 3.3.

Table 3.3: NASA GEVS [26]

Frequency (Hz)	ASD (G^2/Hz)
20	0,026
20-50	+6 dB/oct
50-800	0,16
800-2000	-6 dB/oct
2000	0,026

General Random Vibrations Test Levels (NASA GEVS)

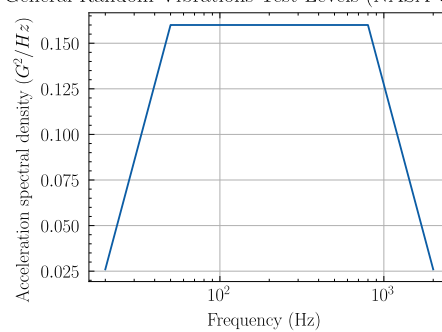


Figure 3.1: NASA GEVS [26] plot

4

Structural design

Contents

4.1 Design approach	26
4.2 Final design	28

This chapter provides a comprehensive overview of the CubeSat's structural design process, encompassing both its primary structure and internal payload components. A detailed description of ISTSat-1 and the newly developed quantum communication payload is presented. To allow visualization of the interior of the CubeSat, one of the lateral solar panels will always be hidden. This enables access to the internal design which would not be visible otherwise, the same applies to chapter 5.

4.1 Design approach

Throughout the design process, multiple difficulties were faced due to the various design approaches that could be taken. Initially, we aimed to fit the quantum communication system within a 1U unit, making the entire CubeSat a 2U size (including the ISTSat-1 payload). However, after creating the first version of the CubeSat and receiving constant feedback from the QuLab team, we realized that this was not feasible. The main issue was the size of the EOAM and EOPM, as they occupied almost 10cm in length, which is too long for a 1U unit. While they could still fit inside the CubeSat, there was not enough space to accommodate the optical fiber cables. In order to fit the optical fiber cables, they would have to be bent at a 90-degree angle, which is impossible as it would cause the fiber to break. Figure 4.1 displays the initial design iteration with some components already in place.

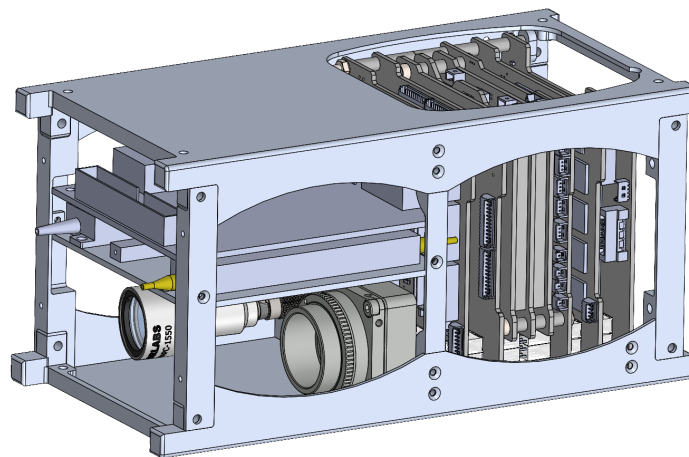


Figure 4.1: 2U CubeSat iteration

During the iterative design process, the placement of the optical components was carefully examined to optimize their configuration. However, it was discovered that some of the components were too large to be accommodated in an optimized configuration (collimator and polarization controller). As a result, these components were replaced with more suitable alternatives to facilitate the design process. It's worth noting that in the initial iteration, components such as the telescope, camera lens, dichroic mirrors,

lasers, and reaction wheels were not defined, and hence not included in the design process.

In the next iteration, the structure evolved to a 3U CubeSat design (see figure 4.2), which allowed to accommodate not only the EOAM and EOPM, along with other optical fiber connections, but also providing with enough space to install reaction wheels in the future. Reaction wheels require a significant amount of room.

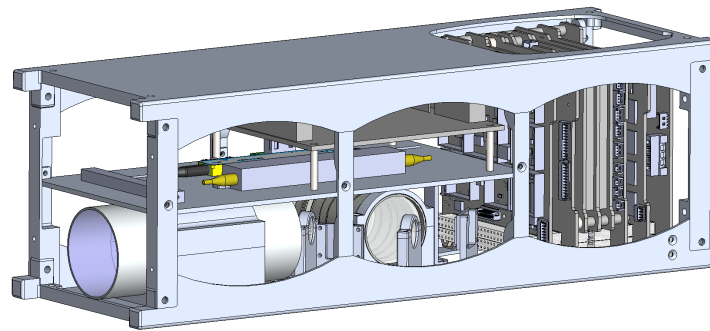


Figure 4.2: 3U CubeSat iteration

At this stage of the design process, the CubeSat has made significant progress. Most of the optical components have already been installed, leaving enough space for the remaining parts. However, during this phase, there were some improvements made to the functional concept and layout of the quantum communication system, which resulted in changes to the size, placement, and orientation of the telescope, camera, and FSM. The improved design is illustrated in Figure 4.3, while the final design will be presented in the next chapter. One of the side frames is hidden for better visualization.

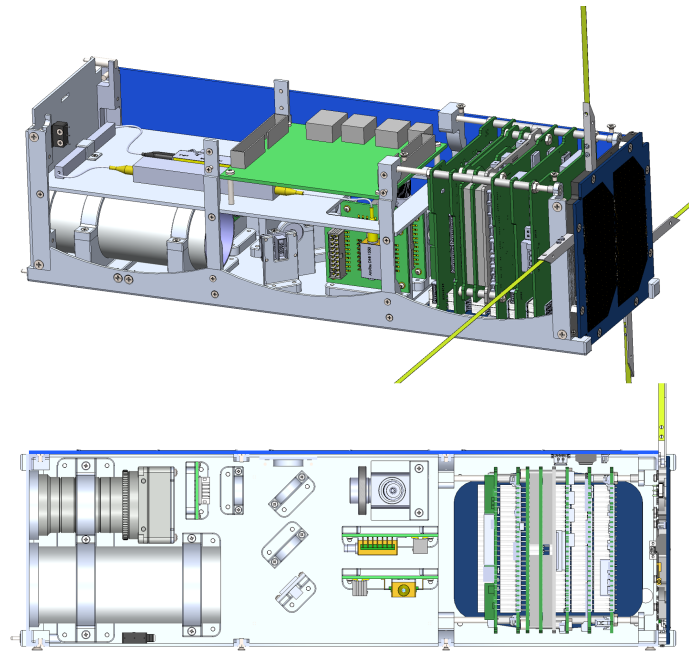


Figure 4.3: 3U CubeSat iteration with the improved optical system and lasers

4.2 Final design

During the preliminary design phase, the CubeSat was planned to have a quantum communication system payload taking up 2U of space, while the remaining U was allocated for an ISTSat-1 payload. The design process began by analysing the mission requirements. The mechanical design had to incorporate the existing ISTSat-1 payload while also accommodating the quantum communication system shown in figure 1.8. The complete CAD model of the CubeSat is depicted in Figure 4.4.

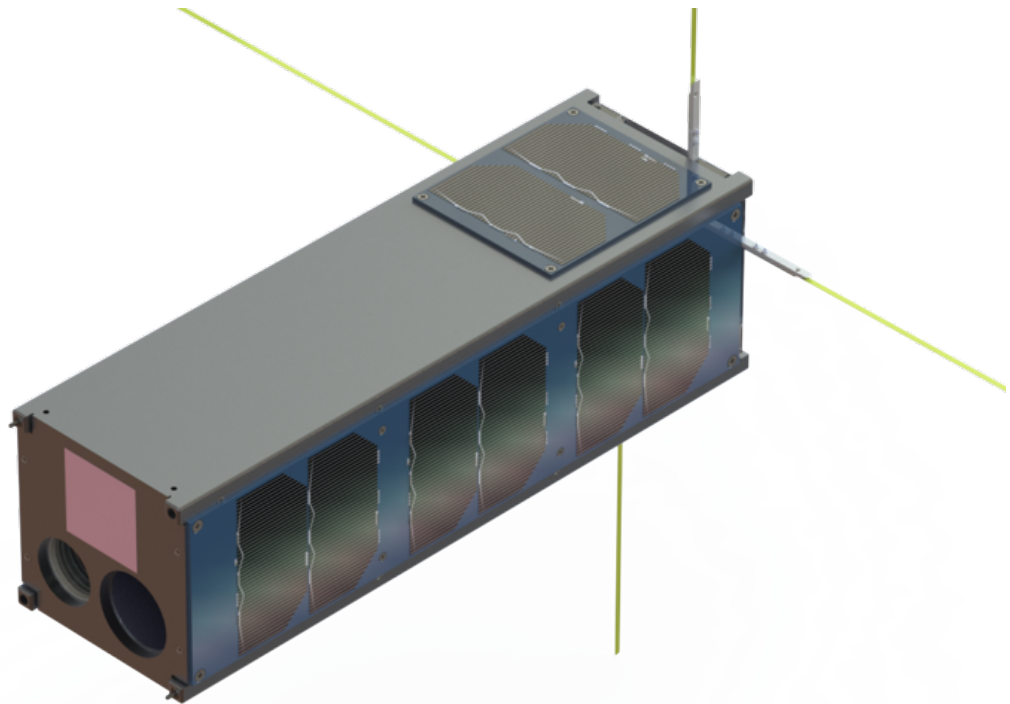


Figure 4.4: 3U Quantum Communication CubeSat CAD

The main structure design is based on the ISTSat-1 structure but with modifications such as expanding from 1U to 3U, adding new ribs, and increasing side frame thickness for improved structural rigidity, thread engagement and load distribution in the optics area alignment. A plate was also included to separate the fiber optical area from the optics area. In Figure 4.5, a partially exploded view of the CubeSat design is displayed with some level of detail. Note that although cable connections are not present, the design has taken this into consideration by providing enough space for these connections. Furthermore, Figure 4.6 provides a detailed view of the quantum communication system, revealing the layout of its main components.

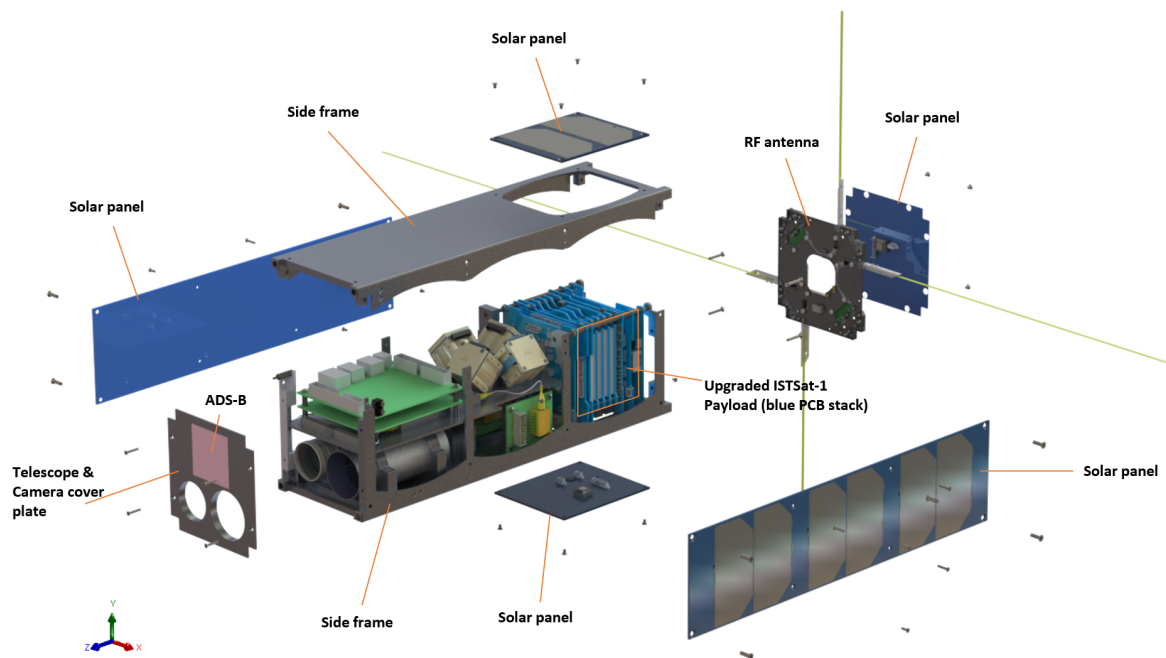


Figure 4.5: CubeSat partially exploded view

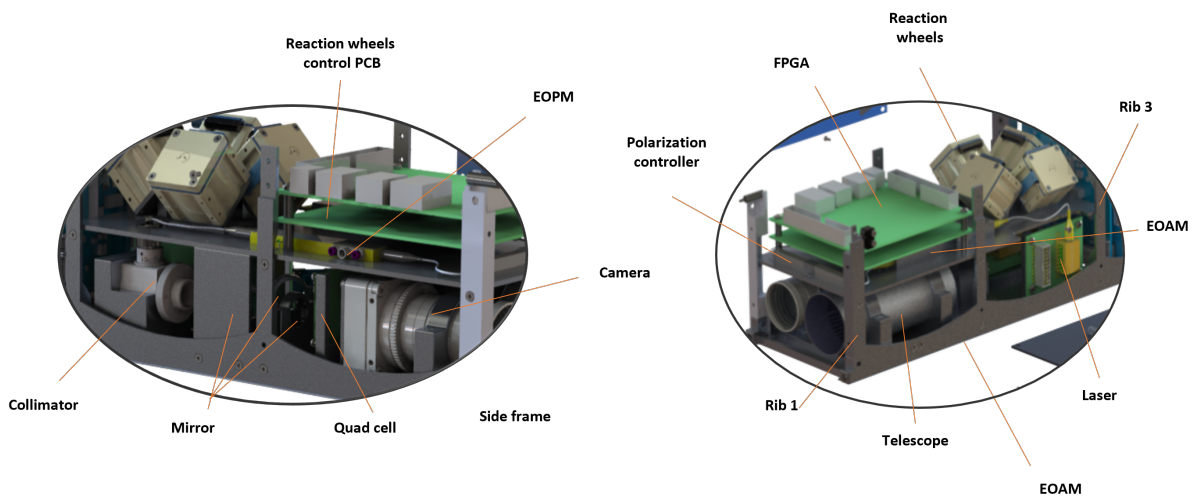


Figure 4.6: Quantum Communication Payload

4.2.1 Materials

Choosing the right materials for a CubeSat is crucial for both its structural integrity and overall cost. Aerospace structures face extreme conditions during launch and operation and therefore need to withstand a wide range of loads. Designers aim to find the best material with the optimal weight/performance ratio, which involves balancing weight and mechanical properties such as yield strength, ultimate

strength, young modulus, and coefficient of thermal expansion. However, with a wide range of materials available, this can be a challenging task. NASA's Material Selection for Aerospace Systems [29] although not specific to CubeSats, provides useful guidelines for material selection.

Aerospace structures like CubeSats are typically made of either aluminium alloys or composite materials. For the CubeSat's main structure and rails, specific aluminium alloys are required by the CDS, although other materials may be used with approval. Table 4.1 shows the recommended alloys and their mechanical properties, as specified by the CDS.

Table 4.1: Recommended materials by CDS

Material Properties	Aluminium alloys			
	5005 - H32	5052 - H34	6061 - T6	7075 - T6
$\rho(\text{kg/m}^3)$	2700	2680	2700	2810
$\sigma_y(\text{MPa})$	117	214	276	505
$\sigma_u(\text{MPa})$	138	262	310	570
E(GPa)	68,9	70,3	68,9	72
$\epsilon(\%)$	11	16	17	11
ν	0,33	0,33	0,33	0,33
G(GPa)	25,9	25,9	26,0	26,9
$\tau(\text{GPa})$	96,5	145	207	331
$\alpha(\mu\text{m}/(\text{m.K}))$	21,9	22,1	23,6	23,3

When contemplating different metals for the CubeSat, one might consider steel alloys. But, steel alloys pose challenges in terms of machining difficulty and higher density, making them heavier. Although they are more cost-effective and easily accessible than aluminium, steel is 2,5x denser (on average) than aluminium. However, the Coefficient of Thermal Expansion (CTE) of aluminium is greater, indicating that the tolerances of parts are more susceptible to alteration due to the expansion or contraction of the material caused by temperature fluctuations. When in Low Earth Orbit (LEO), temperature oscillations can be as high as 125 degrees Celsius in the sun and as low as -65 degrees Celsius in the shadow of the Earth [30]. This is crucial for the alignment and safety of numerous delicate dichroic mirrors and lenses in the optomechanical design.

The material chosen for this CubeSat frame structure was aluminium 7075-T6. Despite its higher cost, this alloy offers a superior strength-to-weight ratio and has a comparable density to other alloys listed in Table 4.1. Additionally, it has excellent yield strength and young modulus. All CubeSat components are made of this material except for the fasteners, PCBs axis, and spacers which are made of Stainless Steel (SS). The PCBs are made of composite Flame Retardant Glass Epoxy Laminate (FR-4), and the connectors PC104 are made of Polybutylene terephthalate (PBT) (plastic part) and brass (pins).

Other electronic components are assumed to also be made of PBT (note this is a simplification over the wide range of different materials used for PCB components). To prevent damage from high-stress concentrations, dichroic mirrors are secured with both the bezel and RTV adhesive, creating a flexible and dampened connection [31].

Refer to Table 4.2 for a complete list of materials used in this CubeSat.

Table 4.2: Selected materials

Material Properties	7075-T6	FR-4	PBT	SS A2-70
$\rho(\text{kg}/\text{m}^3)$	2810	1840	1300	8000
$\sigma_y(\text{MPa})$	505	276	-	450
E(GPa)	72	24(x) 21(y) 21(z)	193	200
ν	0,33	0,12(xy) 0,12(xz) 0,13(yz)	0,39	0,28
G(GPa)	26,9	10,71(xy) 10,71(xz) 9,29(yz)	-	77

4.2.2 Main structure

The CubeSat's main structure consists of eight ribs, a side cover plate, two side frames, and a plate that divides the different stages of the quantum communication payload. All of these parts are made of 7075-T6 aluminium alloy. The plate separating the quantum communication stages has a thickness of 2 mm, while the side frames have a thickness of 1,5 mm in their thinnest areas. Except for the "lower" side frame where the area where the optical mounts are fastened is thicker (3 mm) for better stiffness and countersink screw thread engagement. All second-stage components are mounted with M2 x 6 fasteners from the exterior to the interior of the thicker side frame.

As shown in figure 4.7, the main structure is assembled using countersunk M2 x 4 and M3 x 10 screws, so they are flush with the exterior faces. Additionally, an epoxy resin can be used between contacting faces to prevent the CubeSat from disintegrating if the fastener fails. As mentioned in section 3.2, the main structure's rails must be hard-anodized and have a maximum surface roughness of 1,6 μm . All of these parts require machining using a mill and drill press.

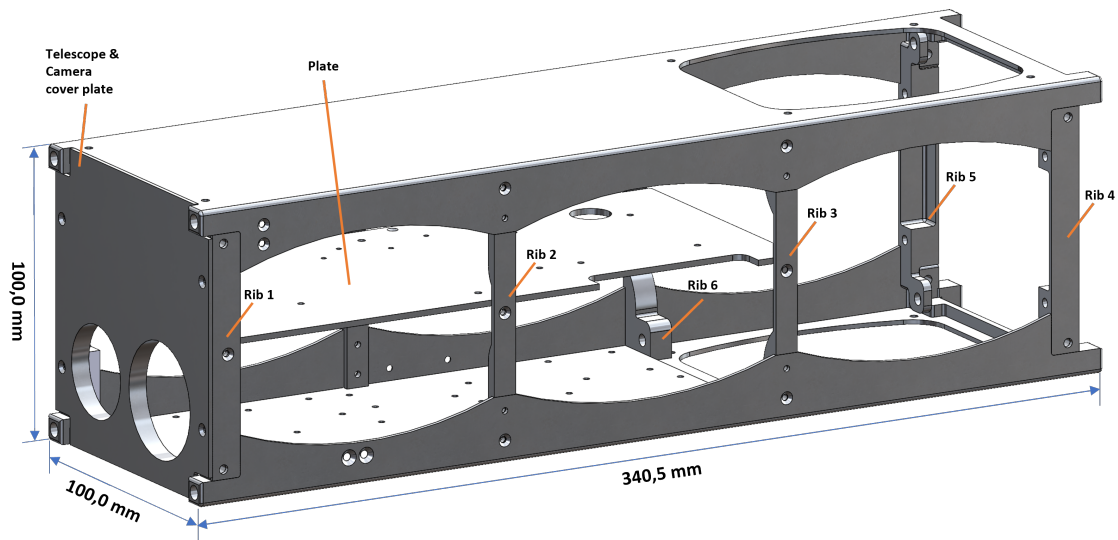


Figure 4.7: CubeSat main structure

4.2.3 ISTSat-1 payload

As previously stated, the new CubeSat design must incorporate ISTSat-1's PCB stack (figure 4.8 on the left) and its functionality. While the previous PCB stack had four batteries in two Printed Circuit Board (PCB), which was sufficient for that mission, the new CubeSat requires new electronic components and four reaction wheels for the already existing ADCS system.

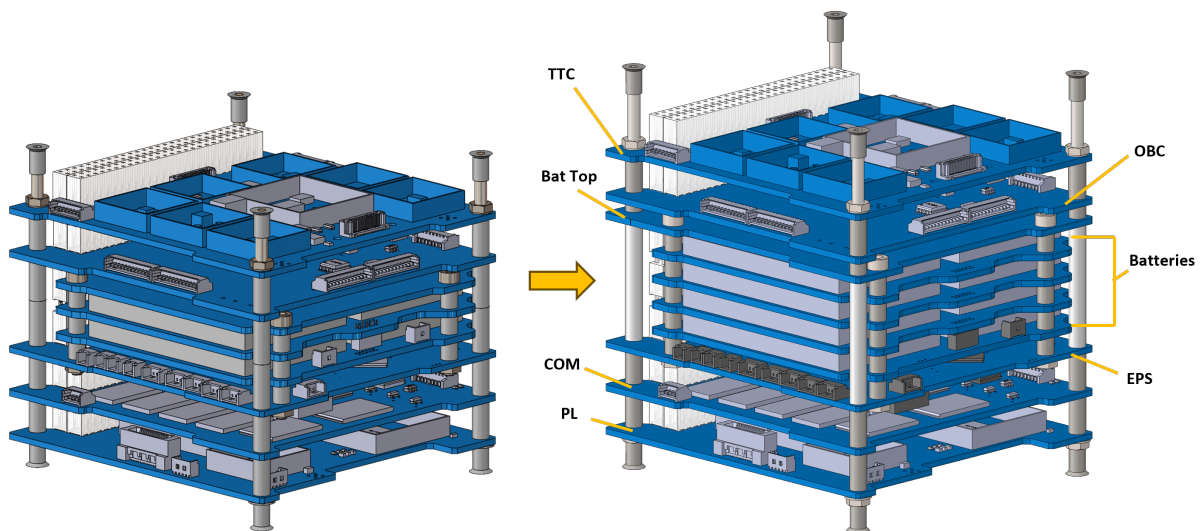


Figure 4.8: Upgraded ISTSat-1 PCB Stack (old on the left and new on the right)

This increases the power consumption, so it was decided to add four more batteries. This maximizes the available space in the U unit for power storage and allows for additional systems if necessary. Figure

4.8 shows the old and new PCB stack.

Note that the "Bat top PCB" has been improved by expanding the mounting points to the external axis. This stiffens the battery's assembly and increases its fundamental frequencies.

Figure 4.9 shows all PCBs in detail.

- **Telemetry, Tracking and Communications (TTC)** is responsible for maintaining the radio link with the ground station through modem modulation and demodulation, as well as providing an additional beacon module for redundancy.
- **On-Board Computer (OBC)** is responsible for CubeSat's processing power, performing necessary calculations for ADCS, data storage, and failure checking.
- **Energy Power System (EPS)** is responsible for managing CubeSat power by harnessing energy from solar panels, storing it in batteries, and supplying energy for all CubeSat systems. Eight lithium-ion polymer cells are attached to it.
- **Communications Processor and Data Storage (COM)** subsystem is responsible for handling communications with the ground station.
- **Payload ADS-B (PL)** receives broadcasted signals from commercial aircraft and translates them into messages.

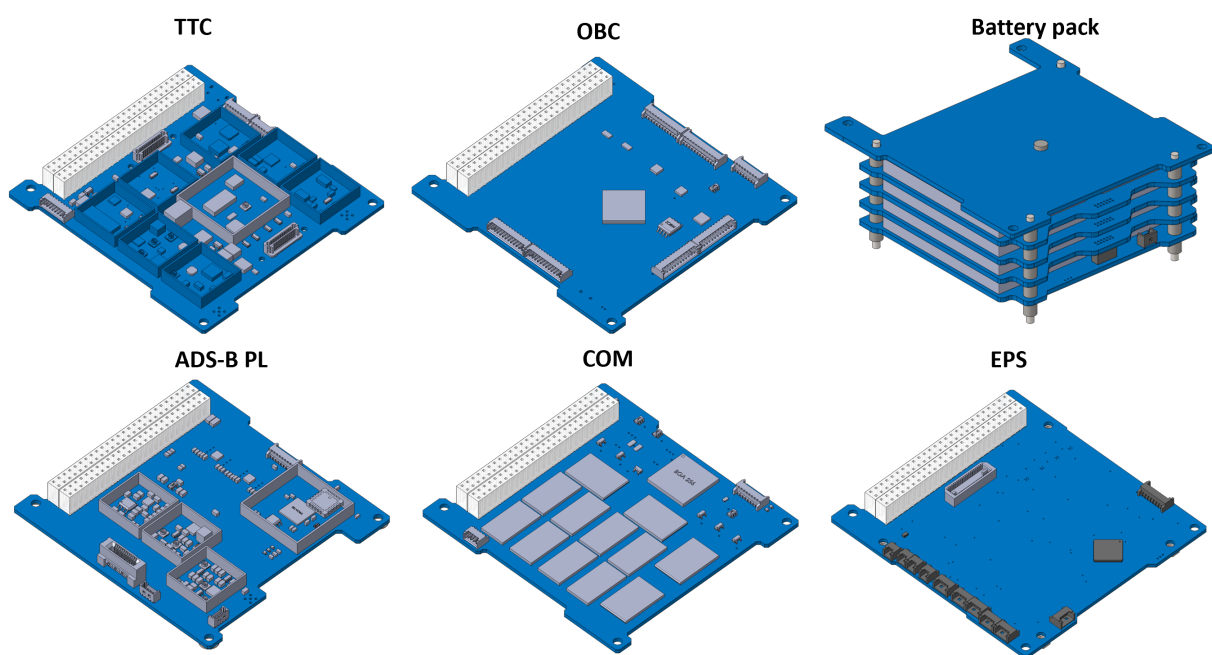


Figure 4.9: Detailed PCBs

4.2.4 Quantum communication payload

The quantum communication payload is designed according to the schematic shown in figure 1.8. Figure 4.10 displays a tilted side view of the overall system, with the 1st and 2nd stages showing the different component orientations.

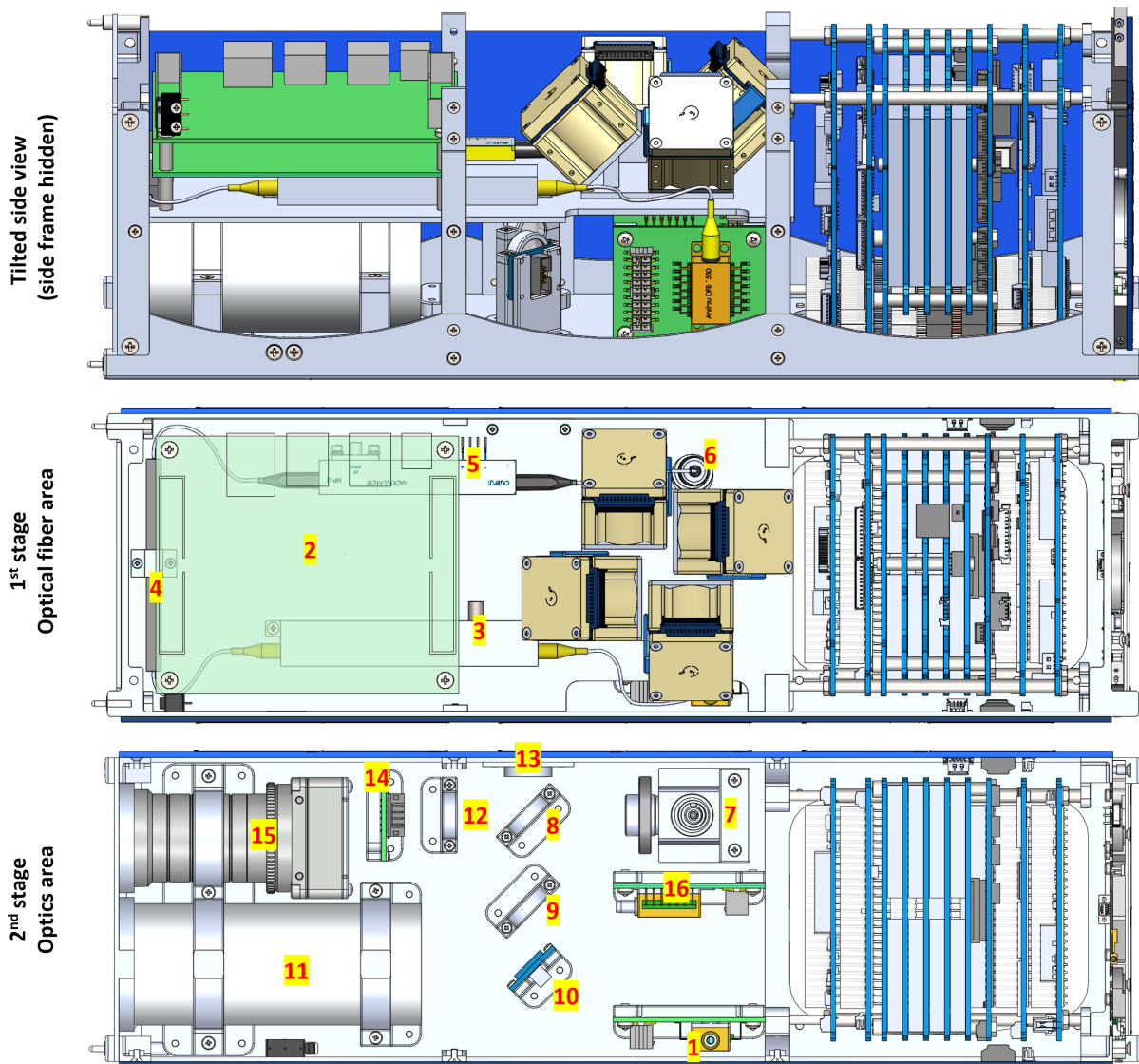


Figure 4.10: Quantum Communication 1st & 2nd stages section views

The 1st stage houses the optical fiber area components, including the FPGA (2), EOAM (3), PC (4), and EOPM (5). The signal then proceeds to the 2nd stage, where it is received by the PA (6) and collimator (7), and continues until exiting through the telescope (path from 7-11). For a more detailed path description, please refer to figure 1.8. It should be noted that the optical fibers were modelled for illustrative purposes only, and the axis of the various dichroic mirrors, FSM, and 1350 nm laser were

precisely aligned to minimize alignment issues.

The numbered components mentioned above are summarized in Table 4.3.

Table 4.3: Parts description

#	Part	#	Part
1	1550 nm Laser	9	Dichroic mirror
2	FPGA	10	Dichroic mirror
3	EOAM	11	Telescope
4	PC	12	Dichroic mirror
5	EOPM	13	Dichroic mirror
6	PA	14	QuadCell
7	Collimator	15	Camera
8	Dichroic mirror	16	1350 nm laser

4.2.5 Dichroic mirror, FSM, QuadCell & Collimator

The assembly of the dichroic mirror (figure 4.11 (a)) consists of five parts: the lower bezel, the upper bezel, the dichroic mirror and two FHC M1.6 x 4 screws.

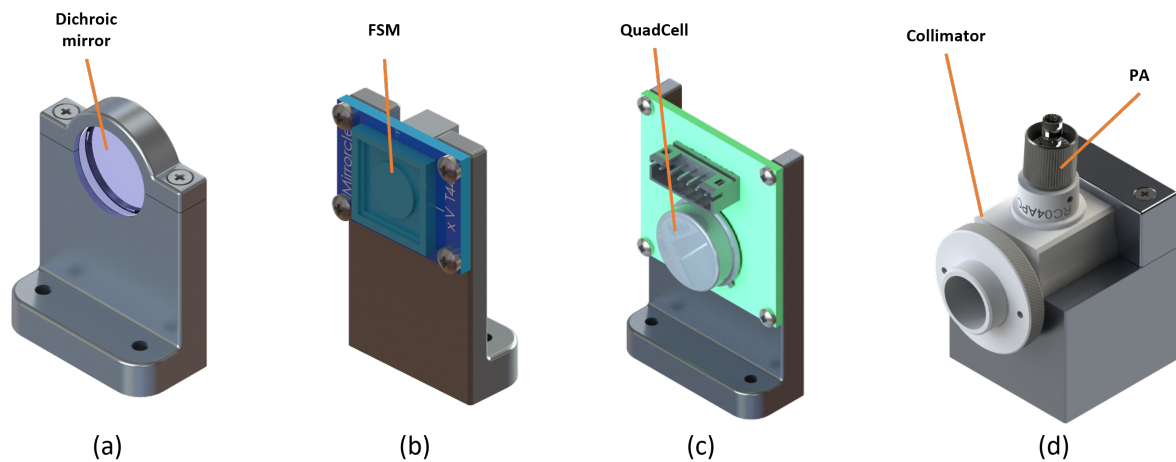


Figure 4.11: Dichroic mirror (a), FSM (b), QuadCell (c) & Collimator (d) assemblies

Aluminum 7075-T6 is the chosen material for its good mechanical properties, particularly its Coefficient of Thermal Expansion (CTE). This is crucial due to temperature fluctuations that occur in space, which were previously mentioned. The precise fit of this delicate component is achieved through Geometric Dimensioning and Tolerancing. Therefore, the assembled mount must provide an H6/g5 dimensional tolerance fitting (for a 12,5 mm diameter hole), which requires careful machining of these parts.

Figure 4.11 (b) and (c) depict the FSM and QuadCell assemblies, respectively. Both have a similar design, with the only difference being their application. In this case, they are mere PCBs. To secure the PCB, FHC M1.6 x 4 fasteners are used. It is essential to note that the QuadCell PCB was explicitly designed for this purpose.

Additionally, the collimator assembly comprises two bezels, the lower and upper, and is secured with two M2 fasteners on the back. The Geometric Dimensioning and Tolerancing of this and most of the parts of this CubeSat may follow general tolerance rules (ISO 2768 m-K).

4.2.6 Lasers

Figure 4.12 illustrates the two lasers used in this particular system. On the left, we have the 1350 nm laser which is crucial for the pointing system. In the middle, we have the 1550 nm laser which serves as the signal generator for the quantum system.

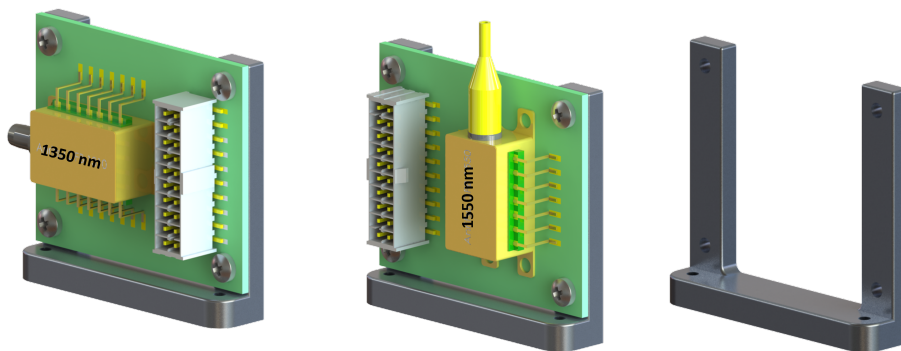


Figure 4.12: 1350 & 1550 nm Laser assemblies

These components are sold individually, without a pre-designed PCB. As a result, two PCBs were designed to suit the required component alignments and orientation, along with a mount (on the right) that can accommodate both versions. The PCBs are secured by four M2.5 x 6 fasteners.

4.2.7 Camera and Telescope

The camera and telescope are among the largest components of the setup, occupying a significant amount of space. Hence, they are assembled together, taking advantage of their cylindrical shape to use a bezel-based mount, as illustrated in Figure 4.13. Two mounts support these components, with one being common and interconnected to both, while the other is separate. The fittings are critical, and the H6/g5 is applied here as well. At the beginning of this work, the telescope make/model was not yet defined, so the presented telescope is an idealization with approximate dimensions of what the

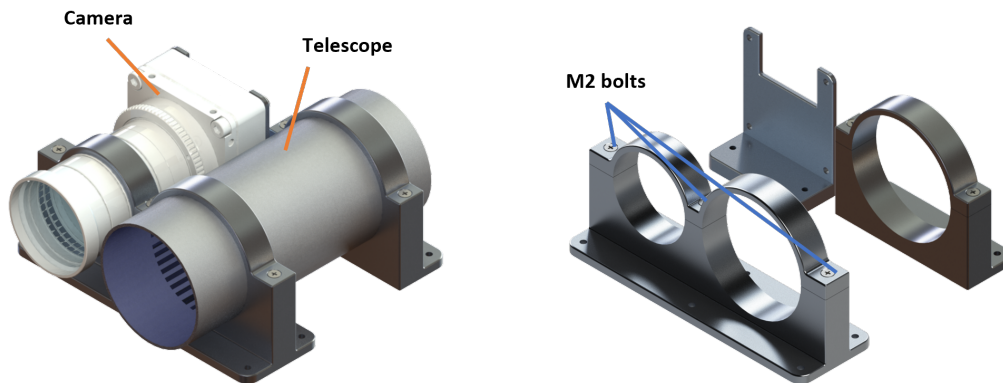


Figure 4.13: Camera and Telescope assembly

real one will be. However, minor adjustments to these mounts may be necessary to accommodate the appropriate telescope make/model. The bezels are secured using FHC M2 x 12 fasteners.

4.2.8 Reaction Wheels

The ISTSat-1's ADCS did not include reaction wheels, however, they are essential for pointing. Reaction wheels operate on the law of conservation of momentum and are responsible for the CubeSat's three-axis control.

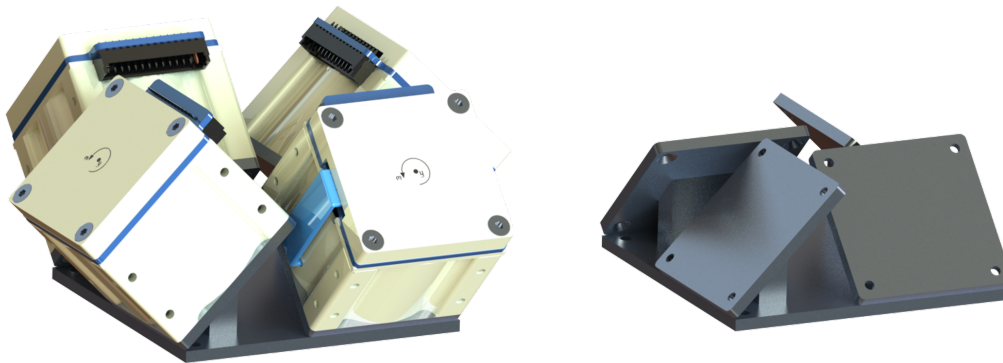


Figure 4.14: Reaction Wheels assembly

They eliminate the need for thrusters to apply torque. Reaction wheels operate at a constant rotation speed, providing the CubeSat with a large amount of stored angular momentum. This changes the rotational dynamics so that the CubeSat rotates in the opposite direction, resulting in angular motion (precession) of the CubeSat axis about the perpendicular axis. However, the attitude control by reaction wheels is limited by their rotational speed. Once they reach their maximum speed, they become saturated and can no longer affect the system dynamics.

João Revés in his master's thesis [32], developed an ADCS and selected the appropriate reaction wheel model and make, which are used in this preliminary design [33]. To have attitude control for all

three axes, three reaction wheels are required. However, the literature recommends using four reaction wheels displayed in a pyramidal layout [34], as shown in figure 4.14, to secure redundancy in all axes in case one fails prematurely. The reaction wheels assembly, shown in Figure 4.14, consists of a baseplate and four tilted support structures.

4.2.9 FPGA and Reaction Wheels control PCBs

Figure 4.15 displays two PCBs, the FPGA PCB and the denominated reaction wheels control PCB. The FPGA operates as the "computer" that processes quantum communication signals.

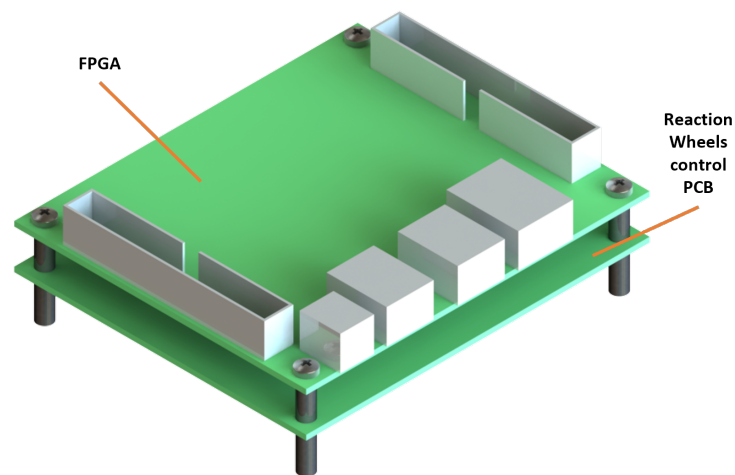


Figure 4.15: FPGA & Reaction Wheels PCBs

However, the visual representation only portrays larger components, such as USB and Ethernet ports. The reaction wheels control PCB was intentionally left empty, as the design requirements are unknown. Nonetheless, this space was accounted for during the preliminary design phase. The four SS axes, along with the spacers and fasteners, ensure that the PCBs are firmly secured in place to the main structure plate shown in figure 4.7.

4.2.10 Solar panels and antennas

ISTSat-1's CubeSat was equipped with five solar panels, containing two photovoltaic cells each. These panels were distributed among five faces, excluding the face with the ADS-B antenna. In the new design, to ensure that each face had at least one solar panel (except for the face with the camera and telescope aperture), an additional four photovoltaic cells were added to fill the empty space between side frames. These photovoltaic cells, manufactured by EnduroSat [35], can generate up to 1,2 W per cell in LEO. The power generated increased by 80% when the total area of the photovoltaic cells was increased from

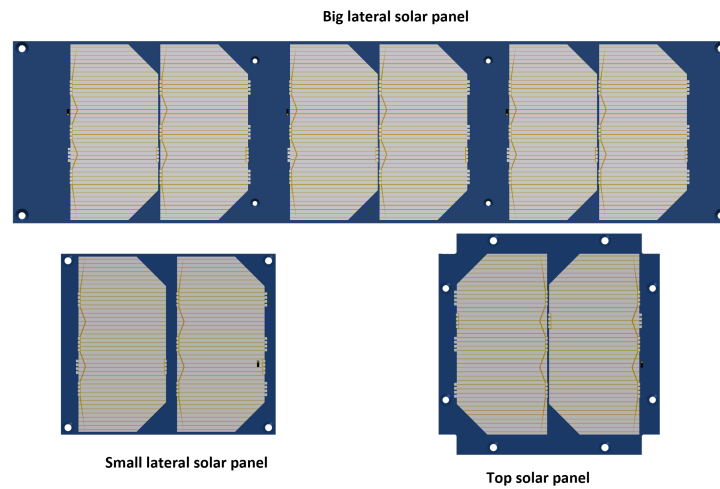


Figure 4.16: Solar panels

301,8 cm^2 to 543,24 cm^2 . This increase in power, from 12 W to 21,6 W, reduces charging time for the additional four battery cells.

In order to fit with the main structure, a "Big lateral solar panel" that is specifically designed (as seen in Figure 4.16) is necessary. However, additional design calculations are necessary to determine the requirements for this new CubeSat design. It should be noted that the number and layout of solar cells are solely for demonstration purposes, and no calculations have been made for the four extra batteries, as they fall outside the scope of this thesis.

The solar panels are securely fastened to the main structure using multiple M2 fasteners. They are also connected to the ISTSat-1 PCB stack via cables.

In Figure 4.17, the V/UHF dipole antenna is depicted in an open configuration. However, during launch, the antenna is retracted to fit inside the P-POD and is later opened in orbit with the help of a spring mechanism. The ADS-B antenna is built using a ceramic-PTFE laminate composite called Rogers Rt/duroid 6010 (refer to Figure 4.5, pink square) and attached to the "Telescope & Camera cover plate" by means of an adhesive.

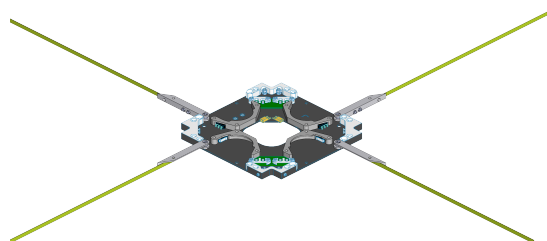


Figure 4.17: V/UHF dipole antenna

4.2.11 Fasteners

When it comes to CubeSat design, the selection of fasteners for connecting different components is crucial. As highlighted in Chapter 2.6, performing a preload calculation is imperative to ensure the correct assembly of the structure and to prevent any thread damage due to over-tightening. This study places particular emphasis on the external fasteners responsible for both securing and shaping the primary structure. However, it's worth noting that preload calculations were also conducted for the remaining fasteners. The material chosen for all these fasteners is A2-70 austenitic stainless steel, as indicated earlier in Table 4.2. Following the procedure of chapter 2.6, the proof strength is given by:

$$\sigma_p = 0.85 \times 450 = 382.5 \text{ MPa} \quad (4.1)$$

For an M2 x 0.40 fastener, the preload force is 793,01 N, and with a K of 0,2, the wrench torque is 0,317 N.m. Table 4.4 summarizes all the calculated torques.

Table 4.4: Fasteners types, sizes, lengths, materials, preload forces, and required torque

Fastener	Size	Length (mm)	Material	Preload force F_i (N)	Torque (N.m)
ISO 7046	M1.6 x 0.35	4	SS A2-70	485.79	0.155
ISO 7045/7076	M2 x 0.40	4 / 6 / 12	SS A2-70	793.01	0.317
ISO 7045	M2.5 x 0.45	6	SS A2-70	1296.98	0.648
ISO 7045/7076	M3 x 0.50	10	SS A2-70	1924.3	1.154

To summarize, the torque calculated is quite low and should be applied with caution using a certified torque wrench. Hand tightening can easily exceed this value and cause damage, so it's important to keep in mind the materials involved, which include SS for the fasteners and aluminium for most of the components. For a reliable grip, it is advisable to use a thread locker such as Loctite 242, 271 or VIBRA-TITE on all CubeSat fasteners. These have undergone space environment testing and offer additional protection against vibrations, particularly for fasteners in aerospace structures [36]. This design uses the fasteners specified in table 4.4 and figure 4.18.



Figure 4.18: ISO 7046 and ISO 7045 fasteners

4.2.12 Center of Gravity and Moments of Inertia

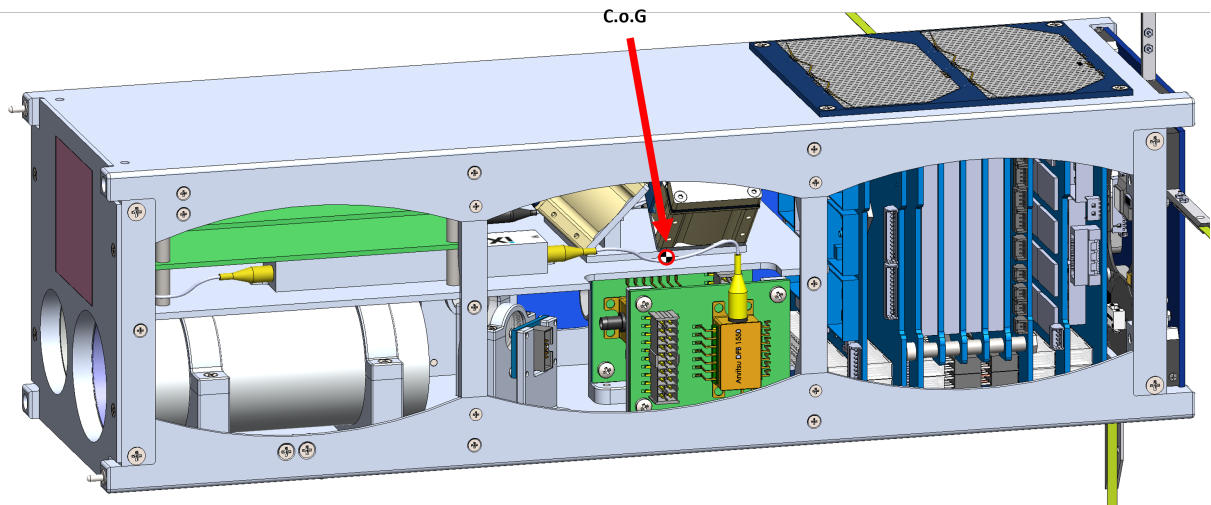


Figure 4.19: CubeSat CoG

The CubeSat's center of gravity (CoG) is located relative to its geometric center. The moments of inertia are measured at the CoG. Figure 4.19 illustrates the CoG's position. Tables 4.5 and 4.6 outline the properties. By examining these properties, it can be determined that the current CoG satisfies the requirement stated in chapter 3. This requirement mandates that the CoG must fall within ± 2 cm for both the X and Y axes and ± 7 cm for the Z axis. The mass of the CubeSat is estimated at 3,185 kg, which is well within the prescribed limit of 6 kg for a 3U CubeSat.

Table 4.5: Center of gravity with respect to the geometric center

Center of Gravity (cm)	
X	-0,87
Y	-0,42
Z	-0,82

Table 4.6: Moments of inertia properties

Moments of inertia ($kg.cm^2$)		Principal moments of inertia ($kg.cm^2$)	
I_{xx}	353,29	I_1	70,93
I_{yy}	361,14	I_2	353,29
I_{zz}	71,63	I_3	361,85

5

Finite Element Analysis

Contents

5.1 Model idealization	43
5.2 Materials	47
5.3 Loads and Boundary conditions	48
5.4 Mesh generation	49
5.5 Static analysis	55
5.6 Modal analysis	59
5.7 Random vibrations analysis	63

This chapter provides a comprehensive overview of the structural analysis of the CubeSat, which was conducted using the finite element analysis (FEA) software SolidWorks Simulation. The design underwent static, modal, and random vibration analyses. Additionally, the model idealization process, including the assumptions and simplifications made, as well as the boundary conditions applied, are discussed in detail. The obtained results are then analysed and interpreted.

5.1 Model idealization

In chapter 4, the design process resulted in a highly complex CAD model (see figure 5.1) that cannot be used for FEA due to the intricate details in multiple parts.

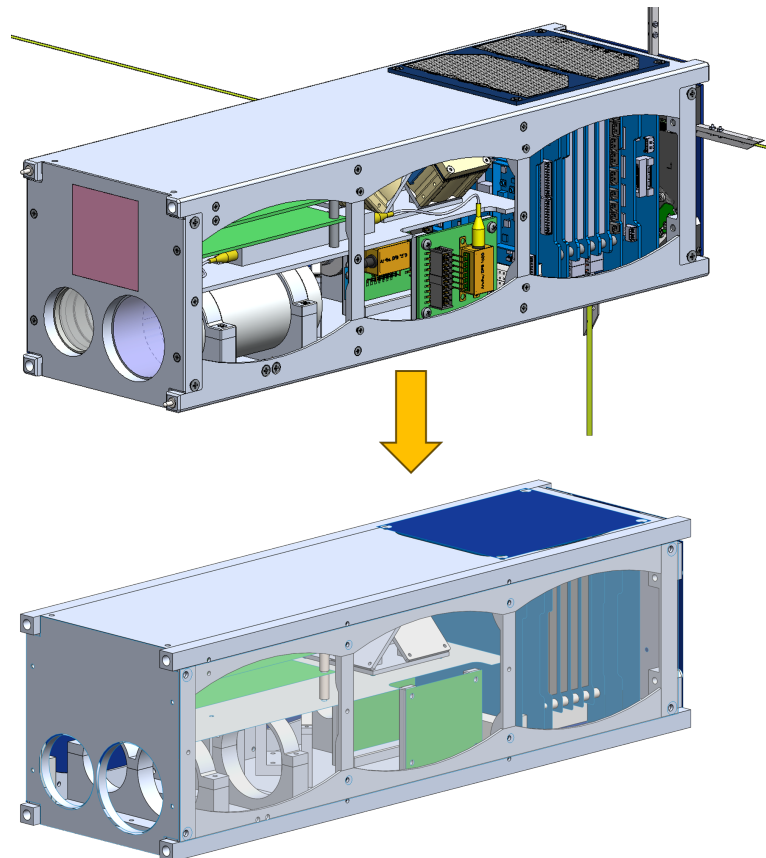


Figure 5.1: Original vs idealization

Taking into account the complexity of the model, it would require a large number of nodes and elements to account for every small detail, which in turn would demand an enormous amount of computational power. To avoid this, a model idealization is often performed, where the CAD model is simplified by using surfaces instead of solids to represent thin plates, or by deleting or suppressing geometry details that are not necessary for the analysis, such as nonfunctional fillets, or by removing components

that are not relevant for the analysis, such as COTS parts.

The idealization process results in a new CAD model for FEA. However, this process involves a trade-off between having a model that accurately represents real behaviour and the computational power and time constraints imposed by the level of detail. This model representativeness will be accessed later in this chapter.

5.1.1 Main structure idealization

The main structure of the CubeSat is made up of several components with curved edges, known as fillets, that serve to enhance the aesthetics and stress distribution of the design. Fillets are crucial in design because sharp edges and corners cause stress concentration. Although fillets decrease stress and improve ergonomics, they also increase mesh complexity.

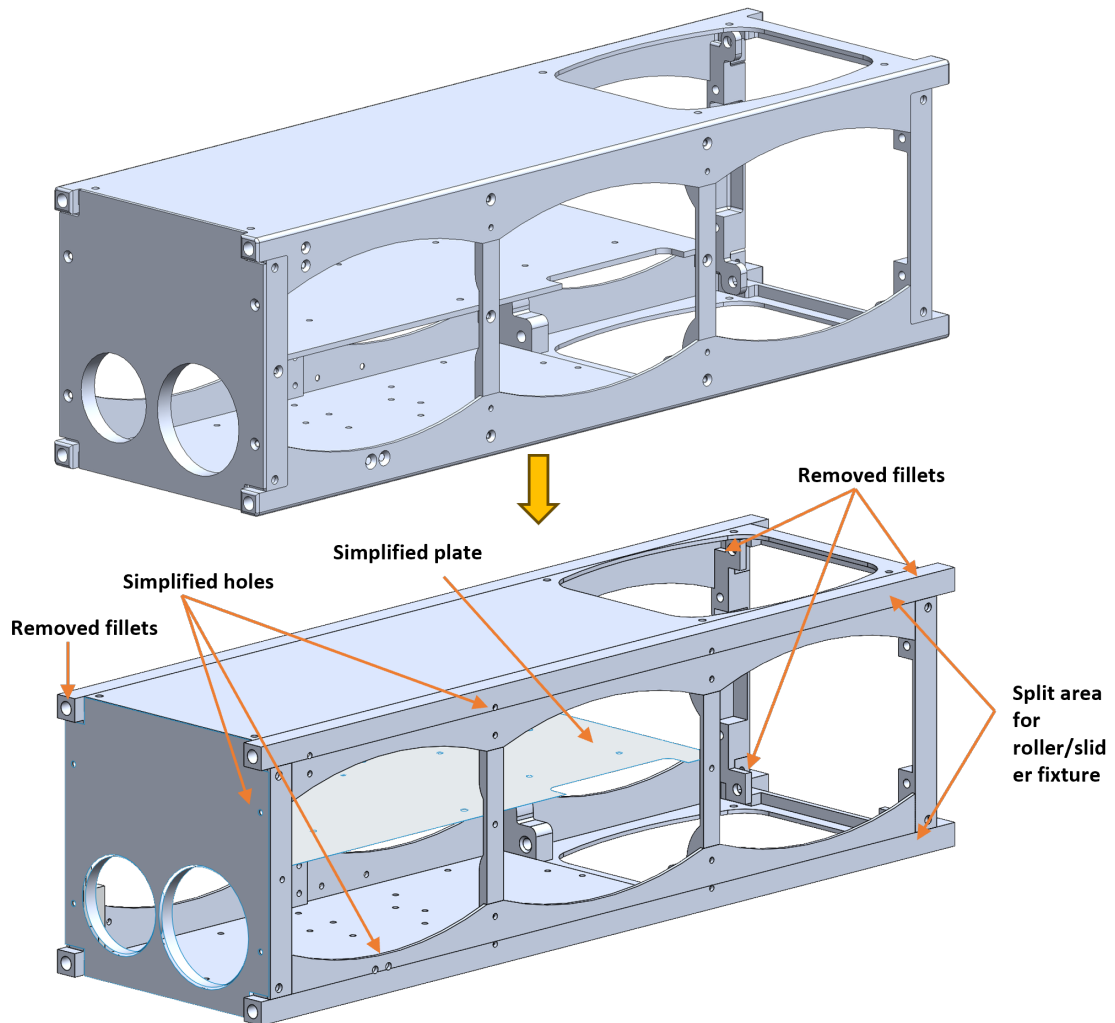


Figure 5.2: Main structure idealization (removed fillets, simplified countersunk holes and delimited area for roller/slider fixture)

Most of the fillets of this CubeSat are quite small, with a radius of only 1mm, which requires small elements in those areas to ensure mesh accuracy. However, considering the load that the CubeSat is exposed to, most of its small fillets are not stress concentrators and therefore do not cause any impact and can be removed. In addition, countersunk holes (chamfer) were changed to simple holes because of the necessary mesh refinement for acceptable simulation runtimes. It should be noted that the cover plate for the camera and telescope was converted from a solid to a surface part due to its small thickness. This was done to prevent meshing failure and element distortion. Figure 5.2 and figure 5.3 shows the idealization process of the main structure and internal optics components, where one can observe a more raw design.

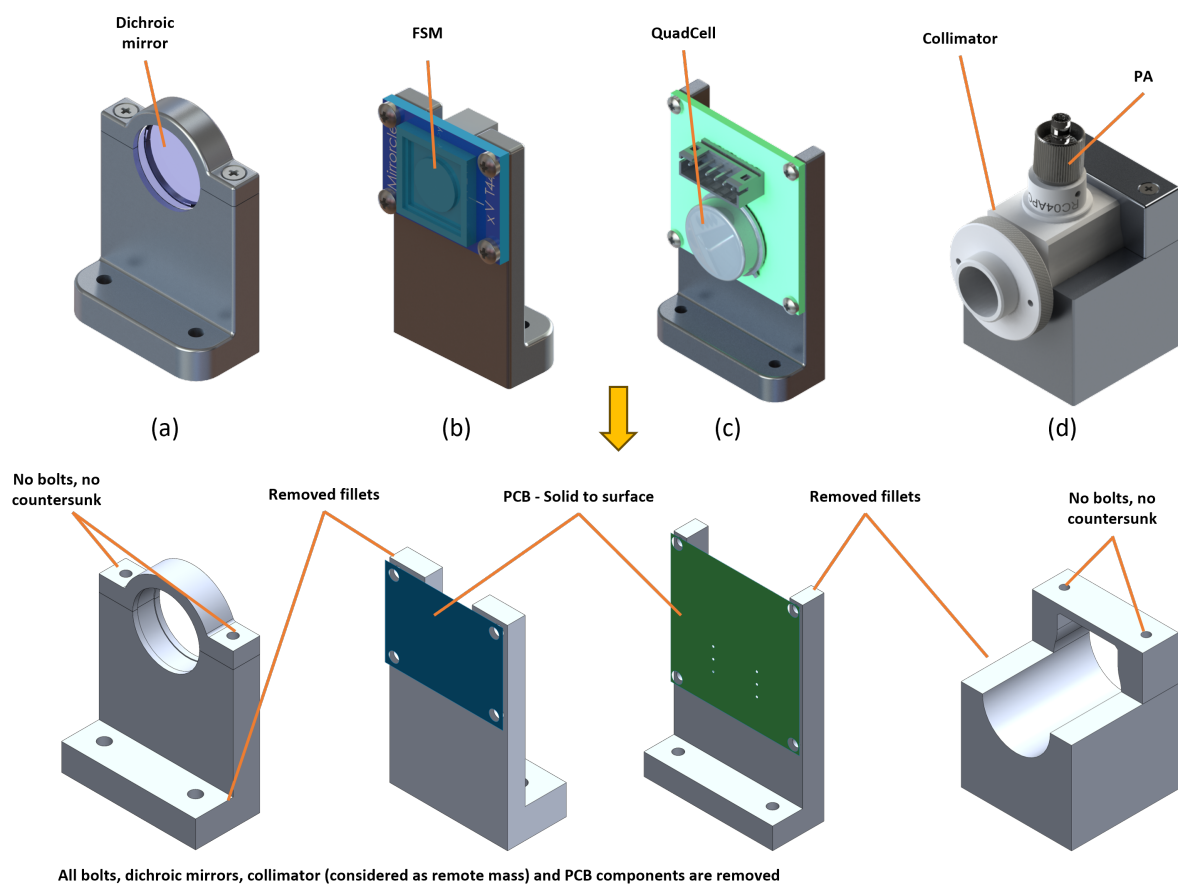


Figure 5.3: Dichroic mirror (a), FSM (b), QuadCell (c) & Collimator (d) assemblies idealization

5.1.2 PCB stack and other PCBs idealization

Detailed information about the PCB stack and other PCBs can be found in chapter 4. These PCBs are highly complex due to the multitude of tiny electronic components they contain, including chips, transistors, connectors, and resistors. Although these components are essential for the proper functioning of various systems, they cannot be included in the analysis due to their small size. Including them would

require a very small element size and create a difficult contact interaction with the larger elements of the PCB, leading to stress concentrations and element distortion.

While these components add minimal rigidity to the structure, they are still significant for the system's proper functioning. Instead of considering their geometries, they are included in the mass of the PCBs. The multiple solder holes are also neglected as they could cause stress concentrations and element distortion. However, there are some exceptions to this simplification. For example, the PC104 connectors' dimensions are more significant to the PCB dimension because they participate in the PCB interconnection, adding stiffness to the system and cannot be ignored. Hollow holes and pins are simplified to a solid box with the required height to reach the next PCB, which affects the system response.

Another exception is the battery cells, that are also idealized as solid blocks. Lastly, the PCBs are converted from solid bodies to surfaces.

As illustrated in Figure 5.4, the process of simplifying the other PCBs of the CubeSat involves converting them all into surfaces, creating a thinner appearance. To determine the mass of electronic components within the PCBs, new densities are calculated. This conversion to surfaces prevents element distortion and improves FE model efficiency. It is worth noting that the battery cells and PC104 may appear to be floating along with the spacers, which is a normal occurrence (no thickness rendered). To accurately simulate their behaviour, local contact interaction will need to be established.

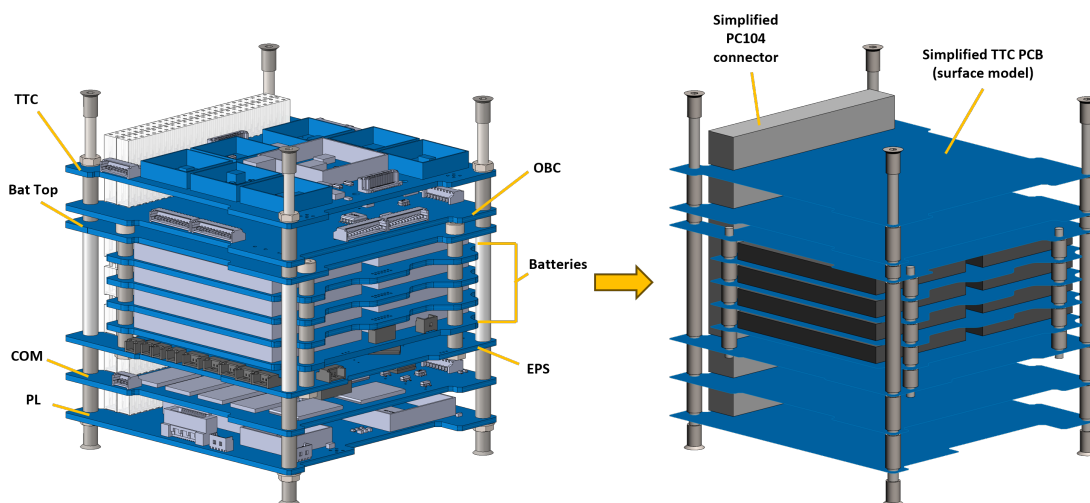
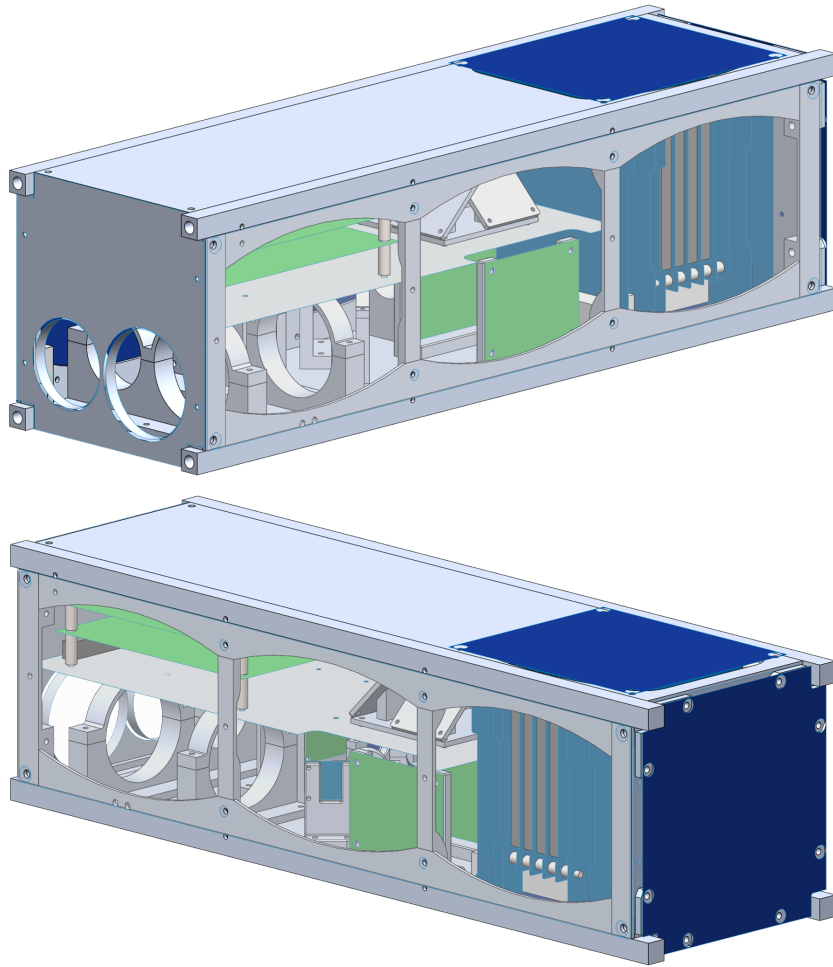


Figure 5.4: ISTSat-1 upgraded PCB stack simplification (from solid to shell elements on PCBs, PC104 connector idealization)

5.1.3 Idealized model

Following the simplification process, we obtained the idealized model showcased in figure 5.5. This model shows the removal of most fillets and the conversion of thin plates such as PCBs, plates, into surfaces. Additionally, several COTS parts like the camera, telescope, collimator, dichroic mirror, EOAM,

EOPM, and reaction wheels were removed, as they are not necessary for this analysis. However, they are considered as remote masses along with their weight and moment of inertia. All fasteners were excluded since the software does not require them to maintain the CubeSat assembled.



This lateral solar panel is hidden for better visualization

Figure 5.5: Idealized model

5.2 Materials

Once the ideal model has been established, the next step involves evaluating the materials to be used for the FEM analysis. These materials are similar to those mentioned in Chapter 4. The main frame of the model is made of Aluminium 7075-T6, while the mounts for the optics and reaction wheel are also made from the same material.

All the PCBs of the CubeSat are made of FR-4, which is an orthotropic material with direction-dependent properties. The only difference between the PCBs is the densities assumed for each one. The PC104 connectors are made of PBT, but the pins are neglected. The battery cells are composed

of various materials with different mechanical properties and are considered as blocks made of PBT. The mechanical properties of FR-4 are the same for all PCBs, except for the different densities. The considered FR-4 densities are the same as of the original ISTSat-1, since no changes were made to these particular PCBs, so the mass should be the same [37]. The mechanical properties of the FE model materials are listed in Table 1.

Table 5.1: FE model materials' mechanical properties

Material Properties	7075-T6	PBT	Stainless Steel	FR-4 (SP)	FR-4 (TTC)	FR-4 (OBC)	FR-4 (EPS)	FR-4 (COM)	FR-4 (PL)
$\rho(\text{kg/m}^3)$	2810	1300	8000	1840	6093	3913	5401	4174	3431
$\sigma_y(\text{MPa})$	505	-	450				276		
	505	-	450				276		
$E(\text{GPa})$	72	193	200				24(x) 21(y) 21(z)		
ν	0,33	0,39	0,28				0,12(xy) 0,12(xz) 0,13(yz)		
$G(\text{GPa})$	26,9	-	77				10,71(xy) 10,71(xz) 9,29(yz)		

5.3 Loads and Boundary conditions

5.3.1 Restraints

In order to ensure a precise and reliable modelling of the system, it is imperative to meticulously establish the correct boundary conditions. These conditions play a pivotal role in delineating the limits and constraints within which a system operates, thereby exerting a profound influence on the reliability of the results obtained.

A model characterized by excessive constraints may impede the natural movement and behaviour of the system, thus deviating from real-world scenarios. Conversely, a model with insufficient restraint may fail to faithfully replicate the actual system, leading to outcomes fraught with inaccuracy. Therefore, it is imperative to ascertain a realistic set of restraints to attain the utmost precision in results.

In this context, a thorough examination of the launch condition of the CubeSat is paramount. The CubeSat is initiated into its trajectory within a deployer akin to the P-POD, wherein it undergoes a process of confinement. Specifically, the CubeSat is secured at its base and along its lateral sides by means of rails. Consequently, the boundary conditions can be construed as being restrictive in the X and Y axes, while allowing for freedom of movement in the Z axis. It should be noted that the previously mentioned characterization may not be fully accurate due to the spring mechanism that is included to deploy the CubeSat in orbit. This mechanism applies pressure on the CubeSat, ensuring a secure fit against the deployer hatch. This added detail brings a nuanced complexity to the boundary conditions, which requires further consideration when modelling the process.

Figure 5.6 depicts the chosen boundary conditions, the yellow faces are fixed and the blue faces

have a roller/slider fixture meaning that they are restricted in X and Y.

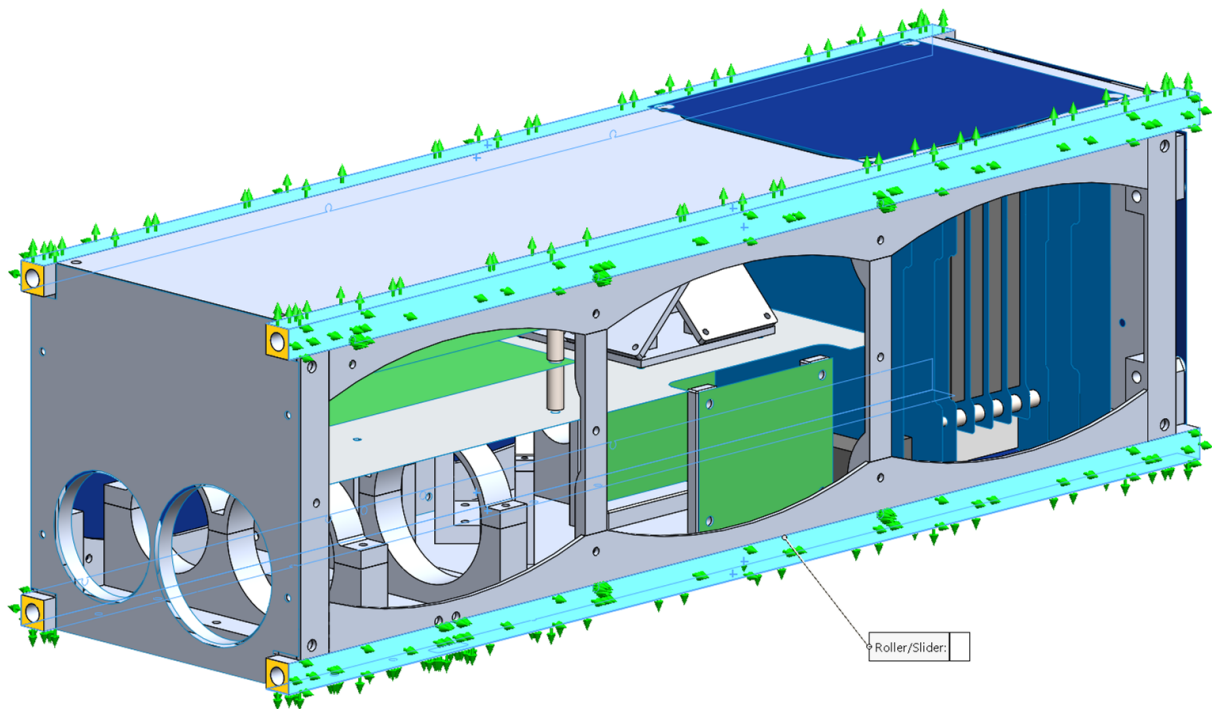


Figure 5.6: Considered boundary conditions (yellow faces fixed and blue faces roller/slider)

5.3.2 Loads

In addition to defining the model constraints, it's crucial to specify the load it will be subjected to. In this case, the only loads taken into account are the weights of the removed components, which are modelled as remote loads. These remote loads are applied to the system as rigid connections. Table C.1 in appendix C shows the remote loads considered, along with their locations and mass properties.

5.4 Mesh generation

Mesh generation is an important step towards creating an accurate FEM model and achieving precise results. The process of 'meshing' involves dividing a continuum system into multiple small elements called 'finite elements'. The choice of element type has a significant impact on computational time and final results. Therefore, components are discretized using either 1D elements, commonly used to represent beams, uniform area rods and screws, 2D elements used to represent surfaces, or 3D elements used to represent solids.

It should be noted that the PCB's axis was originally supposed to be considered as beam elements. However, SolidWorks is quite limited in terms of adding additional nodes, which meant that inefficient

and time-consuming workarounds had to be used since it only created two nodes for each axis. One workaround was to model this axis in multiple steps as structural elements, but the software still failed to create the interaction between the beam nodes and the respective PCB shell. For this reason, the PCB axis and spacers are modelled with solid elements. Additionally, due to the simplifications made for the idealized model, all countersunk holes were simplified. This restricted the application of SolidWorks connectors as fasteners since they need the chamfer to be defined, as a result, they are neglected in this study.

Table 5.2 shows the element type chosen for each component, as well as the materials and thicknesses in the case of surfaces.

Table 5.2: Mesh Element Type, Material, and Thickness for each component

Component	Mesh Type	Element Type	Material	Thickness (mm)
PL PCB	2D	Parabolic triangular element shell	FR-4	1,56
COM PCB	2D	Parabolic triangular element shell	FR-4	1,64
EPS PCB	2D	Parabolic triangular element shell	FR-4	1,48
FPGA	2D	Parabolic triangular element shell	FR-4	1,50
FSM PCB	2D	Parabolic triangular element shell	FR-4	1,57
OBC PCB	2D	Parabolic triangular element shell	FR-4	1,64
TTC PCB	2D	Parabolic triangular element shell	FR-4	1,56
Camera& Telescope cover plate	2D	Parabolic triangular element shell	7075-T6	1,00
Laser PCB	2D	Parabolic triangular element shell	FR-4	1,50
Lateral Mirror mount	2D	Parabolic triangular element shell	7075-T6	1,50
Plate	2D	Parabolic triangular element shell	7075-T6	2,00
QuadCell PCB	2D	Parabolic triangular element shell	7075-T6	1,50
Reaction wheel control PCB	2D	Parabolic triangular element shell	FR-4	1,50
Solar panels PCB	2D	Parabolic triangular element shell	FR-4	1,83
WavePlate mount	2D	Parabolic triangular element shell	7075-T6	1,00
Antenna simplified	2D/3D	Parabolic tetrahedral solid (3D) + shell (2D)	7075-T6	1,00
FSM mount	3D	Parabolic tetrahedral solid	7075-T6	-
Barrel nut	3D	Parabolic tetrahedral solid	SS	-
Battery	3D	Parabolic tetrahedral solid	PBT	-
Camera & Telescope mounts	3D	Parabolic tetrahedral solid	7075-T6	-
Collimator mount	3D	Parabolic tetrahedral solid	7075-T6	-
Dichroic mirror mount	3D	Parabolic tetrahedral solid	7075-T6	-
Lasers mount	3D	Parabolic tetrahedral solid	7075-T6	-
PC104	3D	Parabolic tetrahedral solid	PBT	-
PCBs axis	3D	Parabolic tetrahedral solid	SS	-
PCBs Spacers	3D	Parabolic tetrahedral solid	SS	-
QuadCell mount	3D	Parabolic tetrahedral solid	7075-T6	-
Reaction wheels mount	3D	Parabolic tetrahedral solid	7075-T6	-
Ribs	3D	Parabolic tetrahedral solid	7075-T6	-
Side frames	3D	Parabolic tetrahedral solid	7075-T6	-
WavePlate	3D	Parabolic tetrahedral solid	PBT	-

To create the mesh, all surface components were treated as shell elements, specifically Parabolic Triangular element shells. This was possible due to their small thickness-to-length and thickness-to-width ratios of each surface, which allowed for a simplified finite element model. However, creating a mesh and running the analysis is not sufficient to obtain reliable results in a reasonable computational time. To ensure trustworthy results, a mesh convergence study should be conducted. This study will provide a better understanding of the trend of the results. The mesh was created using SolidWorks

Blended curvature-based mesh. This method works by automatically adapting the element size to the local curvature of the geometries, resulting in a smooth mesh pattern. This allows for components with different element sizes to be meshed without the need for individual mesh control. Figure 5.7 displays the initial mesh without mesh controls.

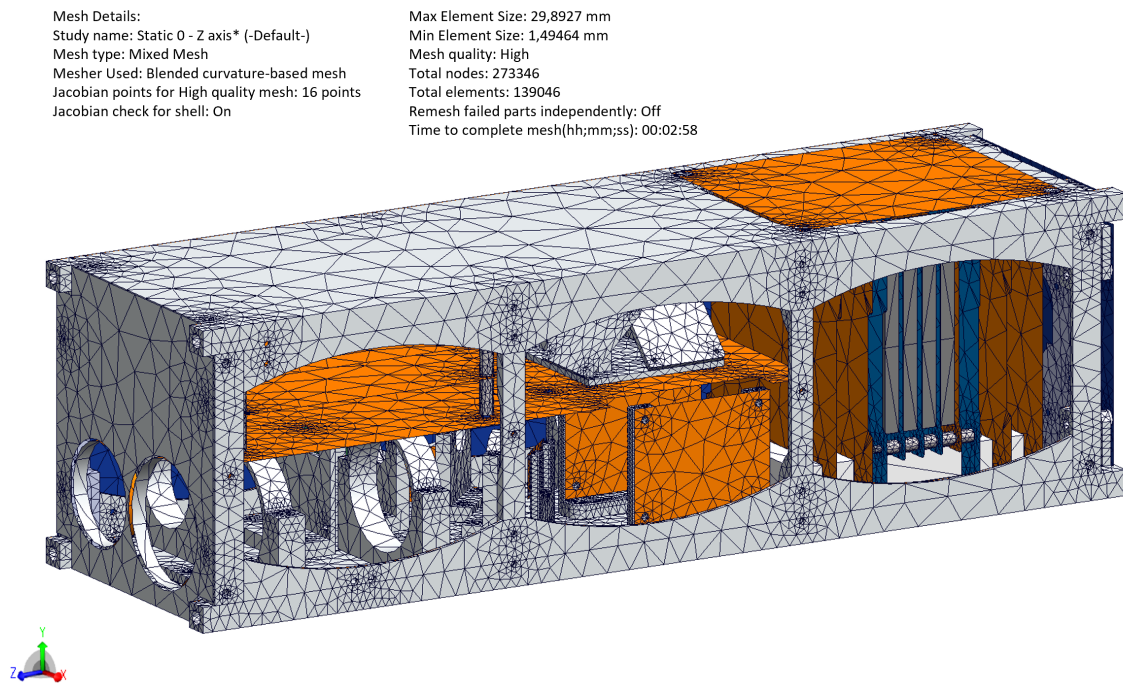


Figure 5.7: Initial mesh

As shown in figure 5.7, the meshing tool has done a good job. It demonstrates some level of mesh refinement around holes and curvatures. However, some components still required a finer mesh to better represent their response. For this reason, mesh controls were applied to all PCBs, the battery cells, and the PC104 connectors. This was necessary because some of the elements were either too large or too few (thickness) to achieve accurate stress variations. To demonstrate mesh independence, successive global mesh refinements were performed.

5.4.1 Convergence study

To begin the analysis of the model, a Modal analysis needs to be performed. This method helps in identifying the modes of vibration, which in turn, allows us to check the contact sets and local interactions between the components. If the assembly is modelled correctly, then the components will remain in their assigned positions. If not, they may "jump" from the assembly and give a small mode frequency value for that component. While the results of the modal analysis are not heavily dependent on the mesh, in-

creasing the number of elements and degrees of freedom reduces the artificial stiffness of the FE model, making it softer. We will start by performing a mesh convergence for the Free-Free configuration, after which we will move on to the Hard-Mounted configuration. The same mesh convergence parameters will be utilized for the static analysis mesh convergence. After the mesh refinement has converged, it will be utilized for all subsequent Static and Random Vibrations analyses.

Table 5.3 displays the results of a mesh convergence study relative to the first important vibration mode of the Free-Free configuration modal analysis. The study focused on the 7th mode since the first six modes are rigid body modes (zero frequency) which represent the system’s translation and rotations.

Table 5.3: Free-Free 7th Mode Frequency convergence

Iteration	Global Mesh size (mm)		# DOF	# Nodes	# Elements	7th Mode Frequency (Hz)	Total solution time (h:mm:ss)
	Max Element size	Min Element size					
1	29,8927	1,49464	2429352	757643	450659	292,84	00:09:56
2	25,783	1,28915	2594838	810754	480989	292,75	00:09:57
3	24,6615	1,23307	2650050	828485	491726	292,91	00:09:54
4	23,1669	1,15834	2726319	853138	506475	292,41	00:10:31
5	21,6722	1,08361	2774046	868091	515437	291,05	00:11:16
6	19,8039	0,990196	2886276	904169	537313	292,06	00:12:34
7	18,3093	0,915465	2975733	932074	554053	293,24	00:12:36

As shown in Table 5.3 and Figure 5.8, the 7th mode frequency is stable around 292/293 Hz.

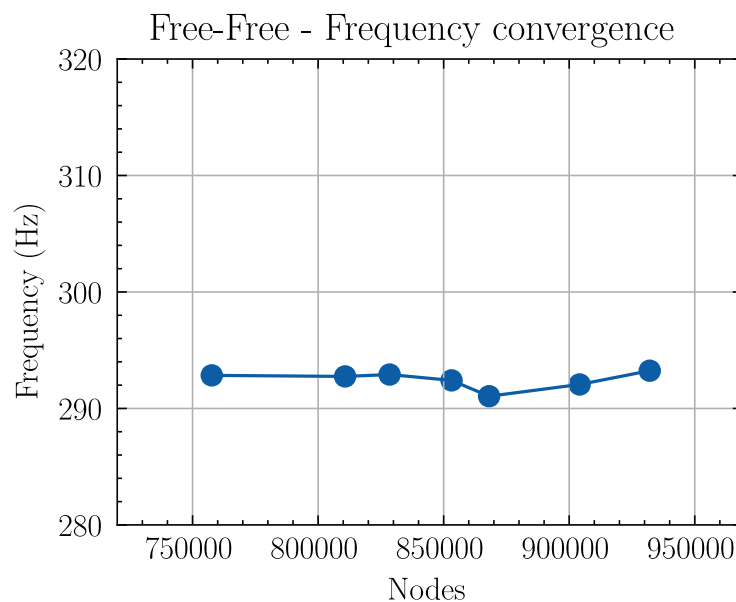


Figure 5.8: Free-Free 7th Mode Frequency convergence

The hard-mounted configuration follows the same procedure as the free-free configuration, with the only difference being the use of constraints that increase the system’s rigidity. Table 5.4 and Figure 5.9 shows a frequency stability of around 283 Hz.

Table 5.4: Hard-Mounted 1st Mode Frequency convergence

Iteration	Global Mesh size (mm)		# DOF	# Nodes	# Elements	1st Mode frequency (Hz)	Total solution time (h:mm:ss)
	Max Element size	Min Element size					
1	29,8927	1,49464	2422548	757279	450392	283,46	00:08:46
2	25,783	1,28915	2587284	810335	480692	283,57	00:09:43
3	24,6615	1,23307	2642361	828097	491452	283,7	00:10:07
4	23,1669	1,15834	2719010	852942	506335	282,84	00:09:56
5	21,6722	1,08361	2764389	867199	514769	281,19	00:10:49
6	19,8039	0,990196	2878058	903876	537078	282,87	00:10:37
7	18,3093	0,915465	2967047	931714	553813	283	00:11:01

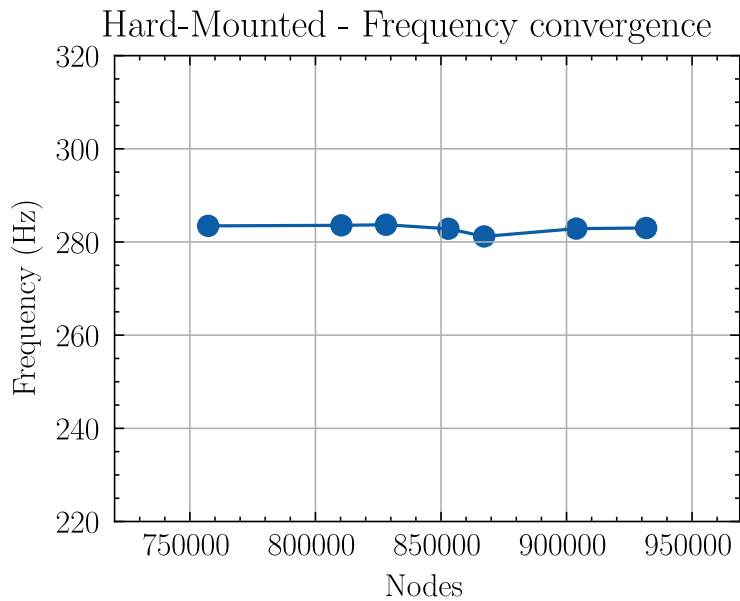


Figure 5.9: Hard-Mounted 1st Mode Frequency convergence

Verifying mesh convergence for every node in a model through static analysis is impractical. Instead, the convergence of the mesh is verified for a known zone of interest that is subjected to solicitation. In this case, a mesh convergence study was conducted on the middle hole of rib 3, which is subject to load from the structural plate during CubeSat acceleration.

Figure 5.10 displays successive mesh refinements around the hole, starting from the initial mesh on the left and ending with the final mesh on the right. From Table 5.5 and Figure 5.11, it can be seen that the maximum stress in this entity converges to a value of 7,5 MPa. It is important to note that in iteration 4, the stress value appears to be an outlier, since the total solution time for this iteration is almost double that of the other iterations.



Figure 5.10: Mesh refinement around the middle hole in Rib-3 (from left to right)

Table 5.5: von Mises stress convergence around the middle hole in Rib 3

Iteration	Global Mesh size (mm)		# DOF	# Nodes	# Elements	Max stress (MPa)	Total solution time (h:mm:ss)
	Max Element size	Min Element size					
1	29,8927	1,49464	2432550	757182	450308	7,525	00:13:12
2	25,783	1,28915	2599161	810380	480717	7,349	00:14:30
3	24,6615	1,23307	2654880	828160	491484	7,178	00:15:06
4	23,1669	1,15834	2731572	852834	506242	8,513	00:29:30
5	21,6722	1,08361	2779593	867765	515183	7,431	00:13:23
6	19,8039	0,990196	2891355	903351	536685	7,31	00:14:42
7	18,3093	0,915465	2982066	931266	553468	7,623	00:16:42

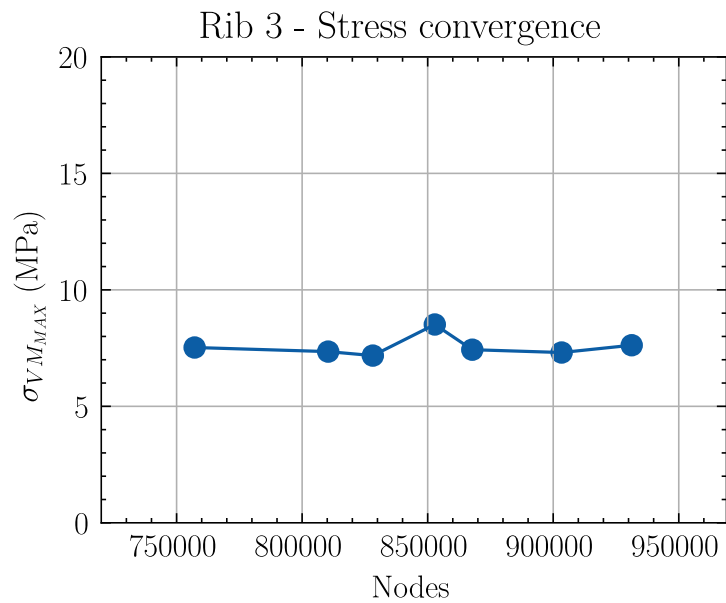


Figure 5.11: von Mises stress convergence around the middle hole in Rib 3

Based on the results obtained from the mesh convergence studies, it can be concluded that the mesh convergence error is less than one per cent. Therefore, the 7th mesh is considered highly accurate. As a result, this mesh will be used for all future studies, as it consists of a total of 931266 nodes and 553468 elements. Figure 5.12 shows the idealized converged mesh.

Mesh Details:
Study name: Static 6 - Z axis (-Default-)
Mesh type: Mixed Mesh
Mesher Used: Blended curvature-based mesh
Jacobian points for High quality mesh: 16 points
Jacobian check for shell: On
Mesh Control: Defined

Max Element Size: 18,3093 mm
Min Element Size: 0,915465 mm
Mesh quality: High
Total nodes: 931266
Total elements: 553468
Remesh failed parts independently: Off
Time to complete mesh(hh:mm:ss): 00:02:21

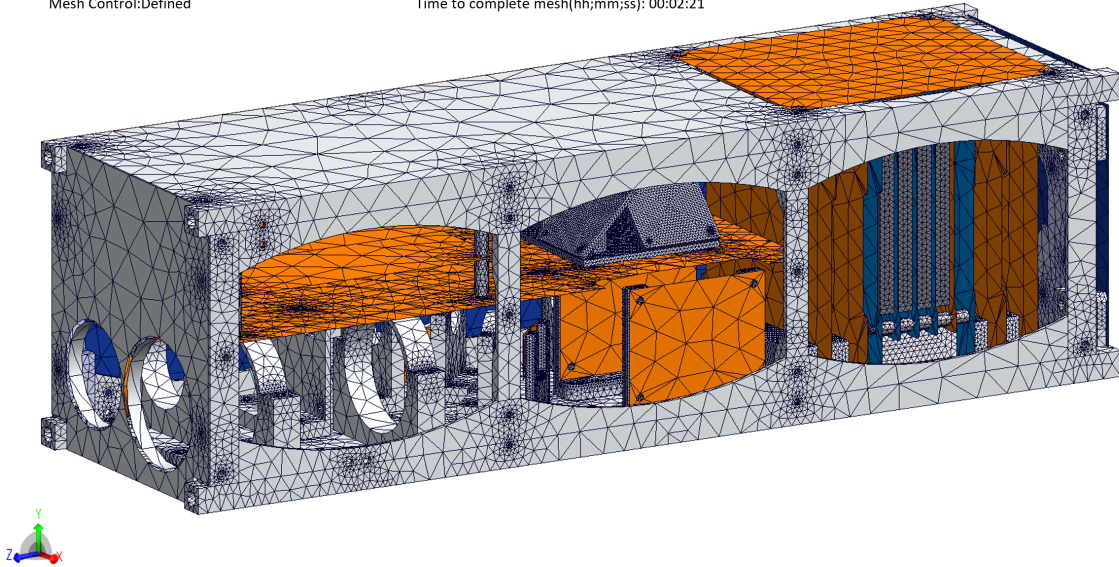


Figure 5.12: Idealized converged mesh

Upon comparison with the initial mesh, it is quite evident that several components have undergone local mesh refinements to achieve improved accuracy and precision. These refinements were mainly done on the PCBs, battery cells, PC104 connectors, and the overall global mesh, with the aim of ensuring the simulation results were as accurate and reliable as possible. It is worth noting that the mesh convergence study has confirmed the effectiveness of these refinements.

5.5 Static analysis

As highlighted in chapter 3, the CubeSat will experience accelerations of around 10g in all directions during launch. To ensure safety, a factor of safety of 2 is applied, resulting in a total load of 20g in the X, Y, and Z axes. It is worth noting that the acceleration can have two orientations, positive or negative, along each axis. In this study, all orientations will be considered. However, the plots for the negative orientations will only be presented in Appendix A.

It's important to note that the deformation scales of the von Mises and displacement plots are larger than one. This means that the visual deformations you see are exaggerated for easier result visualization. Therefore, when it appears that parts of the CubeSat are moving through the side frame and solar panels, it's just a visualization and not the actual deformation. In reality, the deformation is so small that it can't be noticed without the use of a big deformation scale factor.

Please note that during the analysis, the preload of fasteners was not considered due to the reasons mentioned earlier.

Below, you can find the equivalent von Mises stress and displacement for each axis orientation:

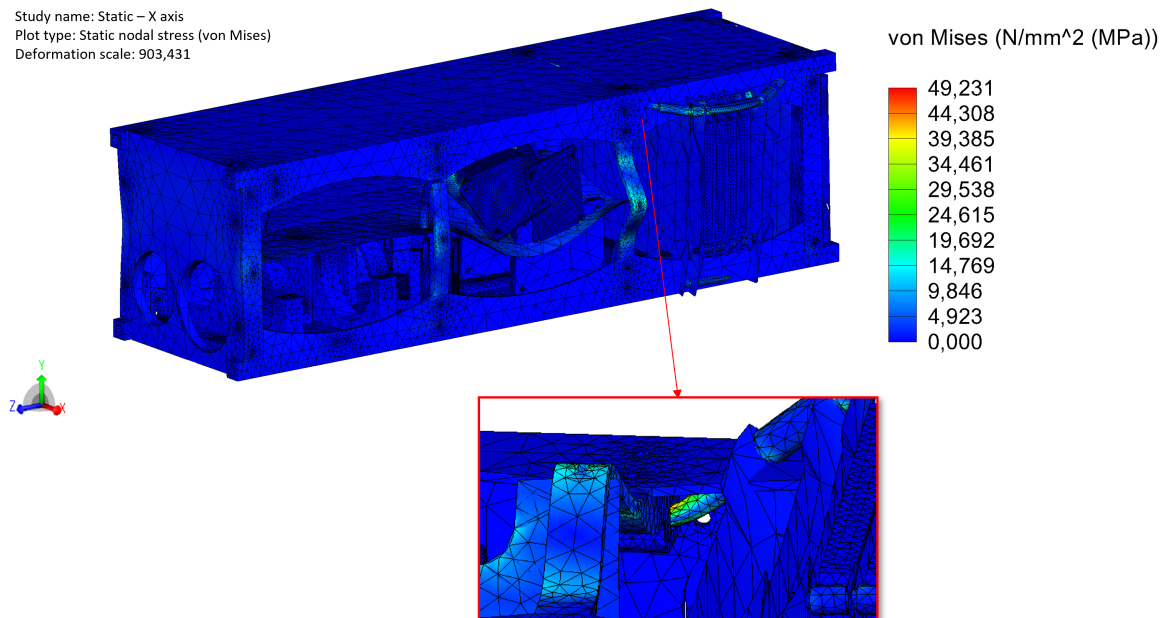


Figure 5.13: CubeSat Static loading X-axis von Mises stress

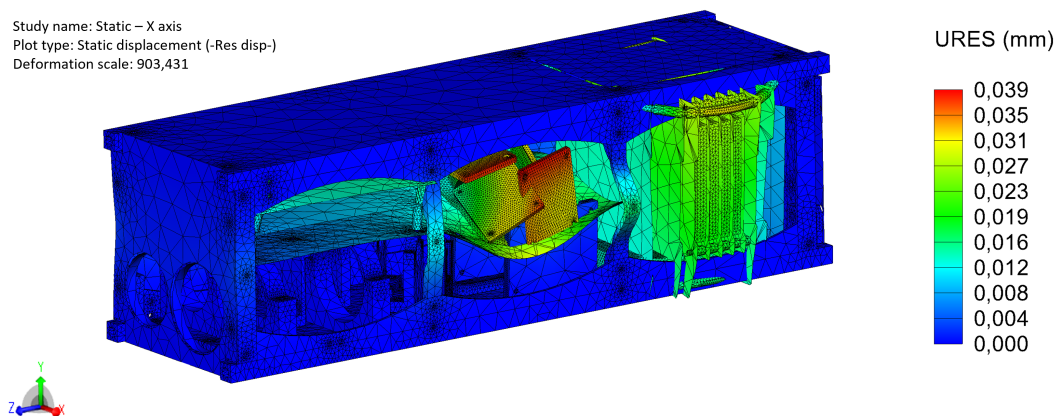


Figure 5.14: CubeSat Static loading X-axis displacement

During the X-axis static loading, the von Mises stress is highest in the vicinity of rib 3, specifically on one of the PCB stack axes. The stress value measures 49,231 MPa, but it is lower than the yield strength of the stainless steel used for the axes. Therefore, there is no need to worry about component failure or damage to other components, and it is considered safe. The maximum displacement is observed in the

reaction wheels mount, and the displacement value is 0,039 mm. You can refer to Figure 5.13 to see the precise location of the stress, and Figure 5.14 to see the location of the maximum displacement.

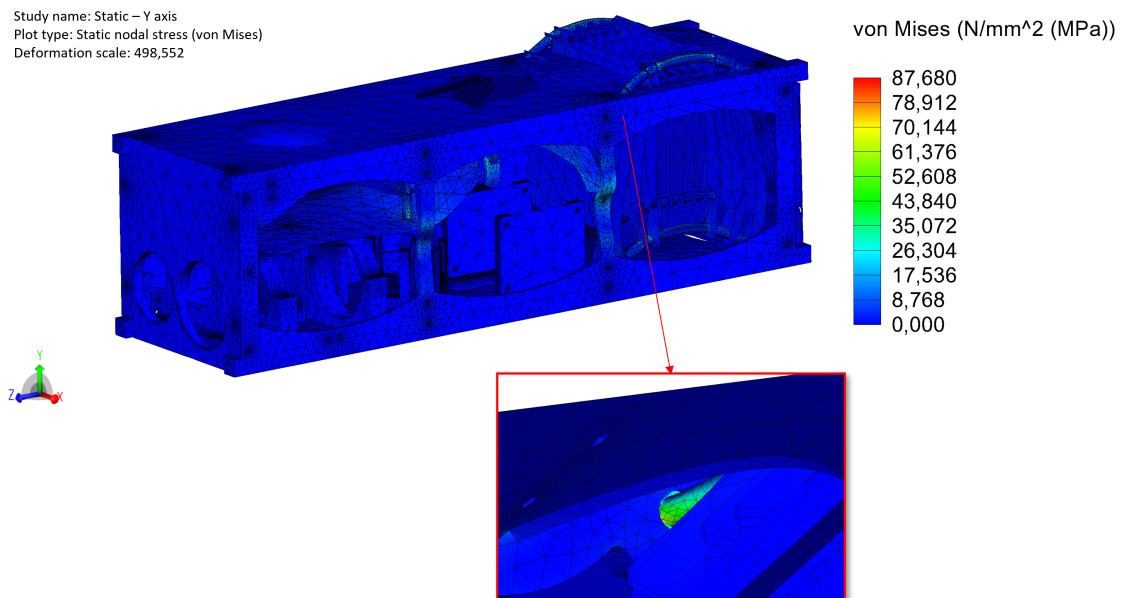


Figure 5.15: CubeSat Static loading Y-axis von Mises stress

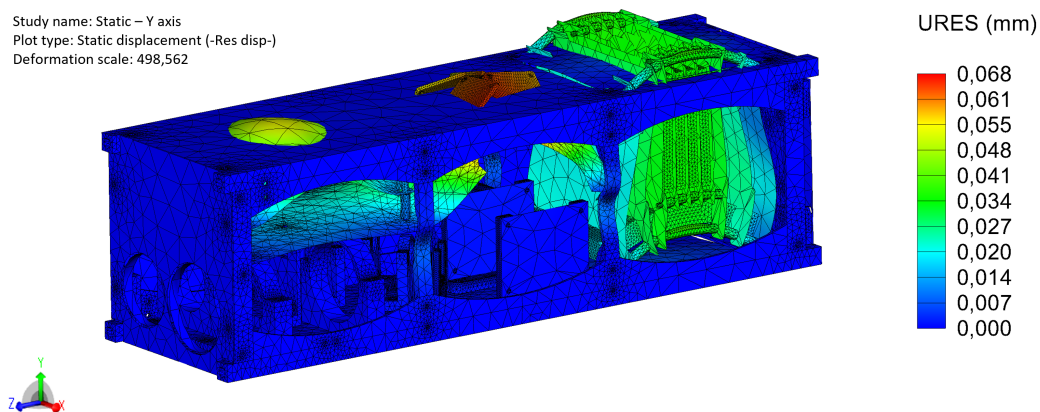


Figure 5.16: CubeSat Static loading Y-axis displacement

During the static loading on the Y-axis, the highest von Mises stress is found in the same location as the X-axis, near rib 3. The value of this stress is 87,680 MPa, which is still lower than the yield strength of the stainless steel used for the axes. You can see the exact location of this stress in Figure 5.15 and displacement in figure 5.16.

Additionally, the reaction wheel mount experiences the largest displacement, with a maximum value of 0,068 mm as it moves upwards.

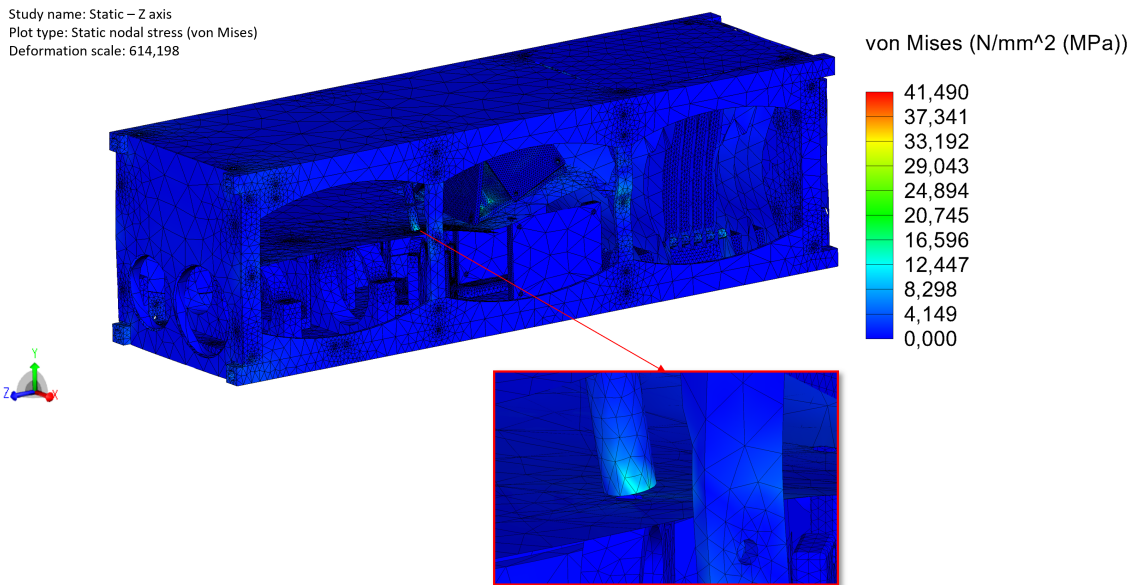


Figure 5.17: CubeSat Static loading Z-axis von Mises stress

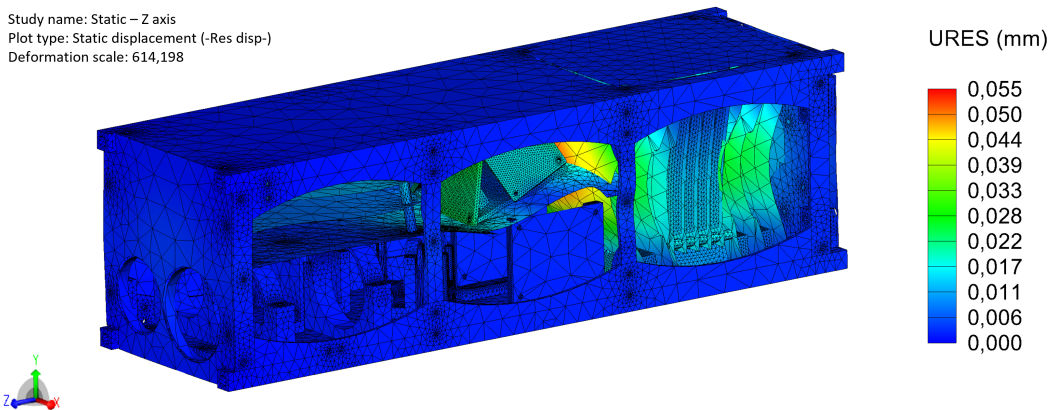


Figure 5.18: CubeSat Static loading Z-axis displacement

Lastly, when subjected to static loading on the Z-axis, the highest von Mises stress is observed in one of the FPGA PCB axes, measuring 41,490 MPa as shown in figure 5.17. In addition, the greatest displacement is perpendicular to the stack of PCBs in ISTSat-1, specifically in the TTC PCB. This particular component experiences the biggest deformation, with a displacement of 0,055 mm (figure 5.18).

Table 5.6 summarizes the maximum stresses and displacement for each loading configuration:

It is evident that the highest levels of stress and displacement occur due to the Y-axis loading. This type of loading affects the PCB stack, reaction wheels mount, and the FPGA PCB stack. However, it

Table 5.6: Static loading maximum stresses and displacements

Axis	+X	+Y	+Z	-X	-Y	-Z
Maximum von Mises Stress (MPa)	49,23	87,68	41,49	49,30	87,20	41,08
Maximum Displacement (mm)	0,039	0,068	0,055	0,039	0,068	0,055

should be noted that the stress level is below the material yield stress, which indicates that the component is functioning within its elastic region and will not experience any permanent deformation. Furthermore, the displacements obtained are on the order of hundredths of a millimetre, meaning that they will not have any impact on the components and can be disregarded. In terms of the negative orientations, the stress levels remain the same across all axes and in the same location (when compared to positive orientation), however, the displacements are in the opposite direction. Moreover, the factor of safety against failure is comfortably high. Table 5.7 illustrates the minimum factor of safety for each axis orientation in the static analysis.

Table 5.7: Minimum Factor of Safety

Axis	+X	+Y	+Z	-X	-Y	-Z
FOS	2,4	2,0	4,2	2,4	2,0	4,2

5.6 Modal analysis

In the initial stages of CubeSat development, modal analysis is conducted to ascertain its natural frequencies and susceptibility to resonance. The mode of vibration pertains to the body's movement in the absence of any external force or damping. This analysis comprises two simulations: free-free and hard-mounted.

The free-free simulation assesses the natural frequencies of the CubeSat without any restrictions, as if it were suspended in mid-air. This is critical in ensuring that the FE model is well-defined, and all components are appropriately constrained. Conversely, the hard-mounted simulation replicates the CubeSat's state when it is constrained within the deployer.

As per NASA's guidelines, the frequency range of interest is from 20Hz to 2000Hz, where the CubeSat experiences most of the stresses. While there may be several more vibration modes than those presented in the tables, the primary objective is to identify the modes that have the most significant impact on the structure and determine if they exceed 115 Hz (minimum fundamental frequency), as stated in chapter 3. It's worth noting that modal analysis doesn't offer any quantitative data on displacements and stresses. To prevent any misinterpretation, all plot legends are normalized so that the maximum displacement always equals 1.

5.6.1 Free-Free configuration

In the free-free configuration, only modes starting from the 7th are displayed. Modes 0 to 6 are rigid body modes representing translations and rotations along each axis. These modes have a frequency of 0 Hz and are not of interest.

Table 5.8, shows the first nine vibration modes along with their respective locations.

Table 5.8: Fundamental modes in free-free configuration

Mode	Frequency (Hz)	Effective modal mass fraction			Location
		X	Y	Z	
7	291,93	2,22E-13	1,13E-12	4,01E-11	Reaction Wheels
8	309,80	7,98E-13	2,86E-11	1,60E-11	Reaction Wheels
9	320,99	3,31E-11	1,71E-11	3,71E-12	Reaction Wheels
10	329,77	8,24E-12	1,02E-13	4,18E-11	Reaction Wheels
11	356,20	6,34E-12	1,18E-11	2,08E-11	Reaction Wheels
12	382,66	4,83E-14	5,49E-14	8,83E-14	TTC PCB
13	408,31	2,41E-13	1,86E-13	3,01E-14	FPGA & R.W Driver PCBs
14	415,78	1,79E-16	1,83E-19	5,91E-17	FPGA & R.W Driver PCBs
15	489,70	2,76E-12	1,78E-13	1,30E-13	COM PCB

Upon conducting modal analysis for the free-free configuration, it was discovered that the 7th mode frequency occurs at 291,93 Hz and is characterized by the movement of the reaction wheel mount. This value is higher than the minimum fundamental frequency specified by the LV, which is 115 Hz. The fact that 291,93 Hz is greater than the specified minimum frequency gives a 2,5 safety factor, which indicates that the preliminary design is good.

Modes 8 to 11 remain in the same location and within the 300 Hz range. Additionally, mode 12 has a frequency of 382,66 Hz and is associated with the movement of the TTC PCB. The seventh vibration mode is illustrated in Figure 5.19.

Study name: Frequency 6 (-Default-)
 Plot type: Frequency Amplitude7 (-Res Amp – Mode shape 7-)
 Mode Shape: 7 Value = 291,93 Hz
 Deformation scale: 0,0155298

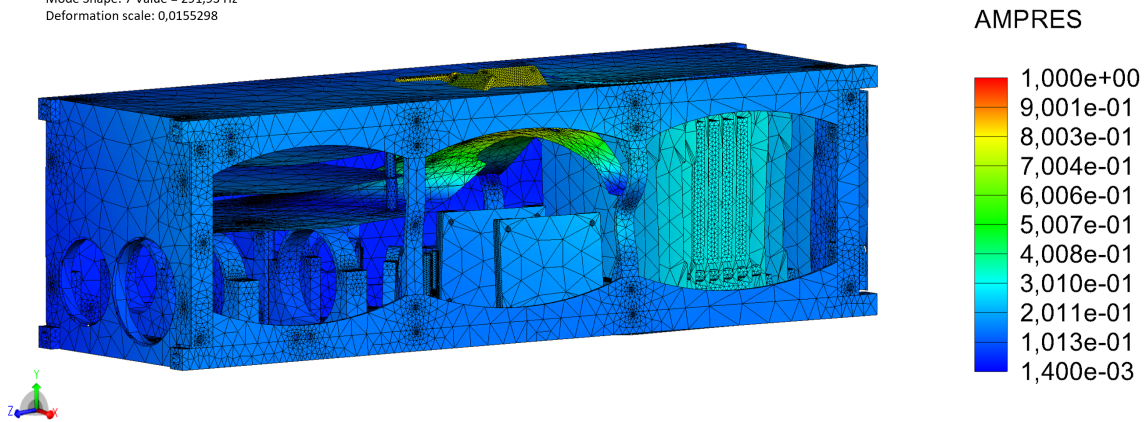


Figure 5.19: Free-Free - 7th vibration mode

5.6.2 Hard-Mounted configuration

The hard-mounted configuration is the most crucial setup as it closely simulates the launch environment. In this analysis, the CubeSat is held in place by its four feet and a roller/slider on rails. As the structure is restrained, there are no rigid body modes and all the modes are elastic. The analysis displays only the first fifteen modes in this configuration.

Table 5.9, shows the first fifteen vibration modes along with their respective locations.

Table 5.9: Fundamental modes in hard-mounted configuration

Mode	Frequency (Hz)	Effective modal mass fraction			Location
		X	Y	Z	
1	283,66	0,018123	0,098460	0,000119	Reaction Wheels
2	310,69	0,003606	0,001898	0,021886	Reaction Wheels
3	318,50	0,000048	0,002277	0,018069	Reaction Wheels
4	330,85	0,000530	0,000041	0,000790	Reaction Wheels
5	344,44	0,034817	0,038475	0,001970	Reaction Wheels
6	377,49	0,000002	0,005298	0,027999	TTC PCB
7	399,52	0,000314	0,184710	0,000177	PCB Stack
8	401,54	0,000016	0,013971	0,000046	FPGA & R.W Driver PCBs
9	415,78	0,000000	0,000001	0,000001	FPGA & R.W Driver PCBs
10	493,29	0,025920	0,001476	0,048291	OBC & EPS & PL PCBs
11	496,92	0,128200	0,002382	0,006317	PCB Stack
12	500,30	0,012218	0,000553	0,002991	Reaction Wheels
13	504,81	0,005511	0,001319	0,007944	COM PCB
14	515,87	0,000055	0,000070	0,016529	OBC & EPS PCBs
15	523,39	0,019782	0,001827	0,006215	Reaction Wheels

In this analysis, the first five modes are related to the reaction wheels mount. However, the 7th mode

of the free-free configuration has a higher frequency. One might expect the first mode frequency of the hard-mounted configuration to be higher due to the increased stiffness of restraining the CubeSat. Nevertheless, restraining the CubeSat changes the effective mass participating in vibration and stiffens the structure behaviour.

According to table 5.9, the first mode frequency is 283,66 Hz, which is significantly above the required frequency of 115 Hz specified by the LV. This fundamental frequency gives a large margin (2,46 safety factor), even with all the simplifications and assumptions made.

Even if the mass of the CubeSat were to increase two-fold, reaching the maximum limit of 6 kg, the fundamental frequency would only decrease to about 70% of its current value, which is approximately 198,56 Hz (assuming the same stiffness). Despite the decrease, the safety factor would still remain at 1,73, ensuring the CubeSat's stability.

The next modes from six to eleven occur on various PCBs on the CubeSat, mainly the ISTSat-1 PCB stack and the FPGA & R.W driver PCBs. These modes start with TTC PCB vibration and then extend to the PCB stack as a whole.

The first vibration mode is shown in figure 5.20

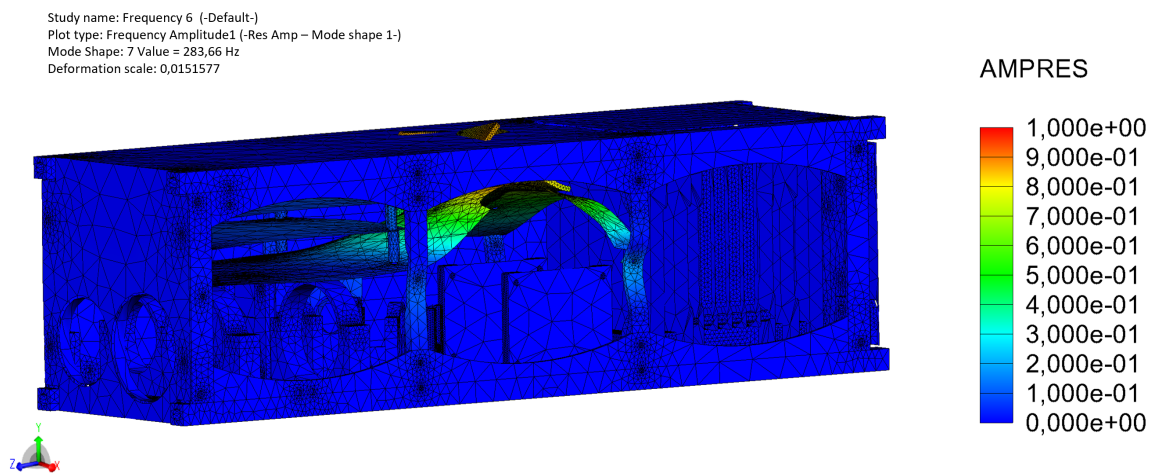


Figure 5.20: Hard-Mounted - 1st vibration mode

In addition, figure 5.21 displays the effective mass participation factor for each axis and mode. This indicates the proportion of the total modal mass that is involved in each mode. The data from the first mode reveals that the Y axis has the largest effective mass participation factor, meaning that approximately 9,8% of the total CubeSat mass is involved in the Y direction. This observation aligns with the information presented in table 5.9.

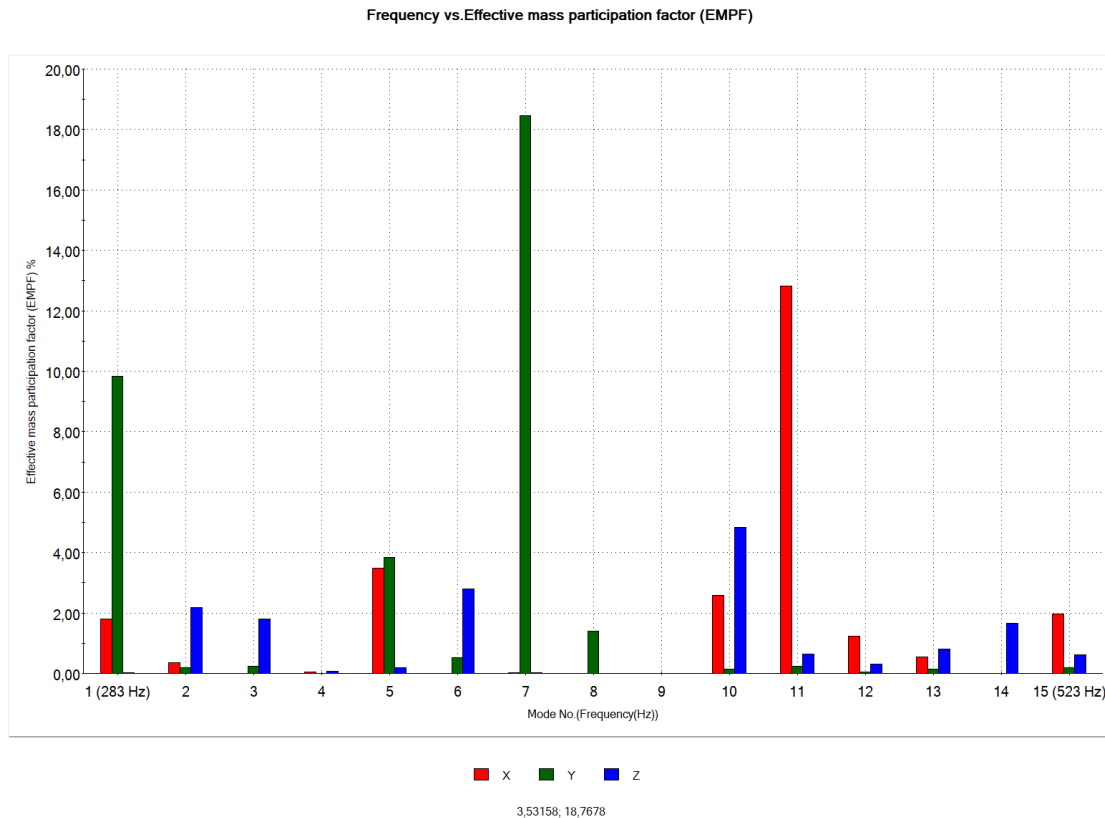


Figure 5.21: Effective mass participation factor

5.7 Random vibrations analysis

To conduct the random vibration analysis, it is necessary to subject the CubeSat to NASA's GEVS ASD. As with the static analysis, the analysis must be conducted in all three axes. However, due to hardware limitations such as RAM and disk space, only the Z-axis simulation will be presented here. The total solution time for this analysis is roughly 7 hours. For this analysis, the boundary conditions remain the same as in the static loading, with four feet fixed and rails used as slider/roller. The damping factor is set to a standard value of 2%. Information on the ASD input can be found in chapter 3 and was sourced from NASA's GEVS [26]. Figure 5.22, shows the maximum RMS von Mises stress.

The highest von Mises stress of 128,79 MPa can be observed in one of the holes located on the side frame, as shown in figure 5.22. This intense stress level may be attributed to the split line section where the roller/slider restraint is applied, leading to a stress concentration. Nonetheless, a more detailed analysis is required to tackle this matter and identify potential areas of singularity.

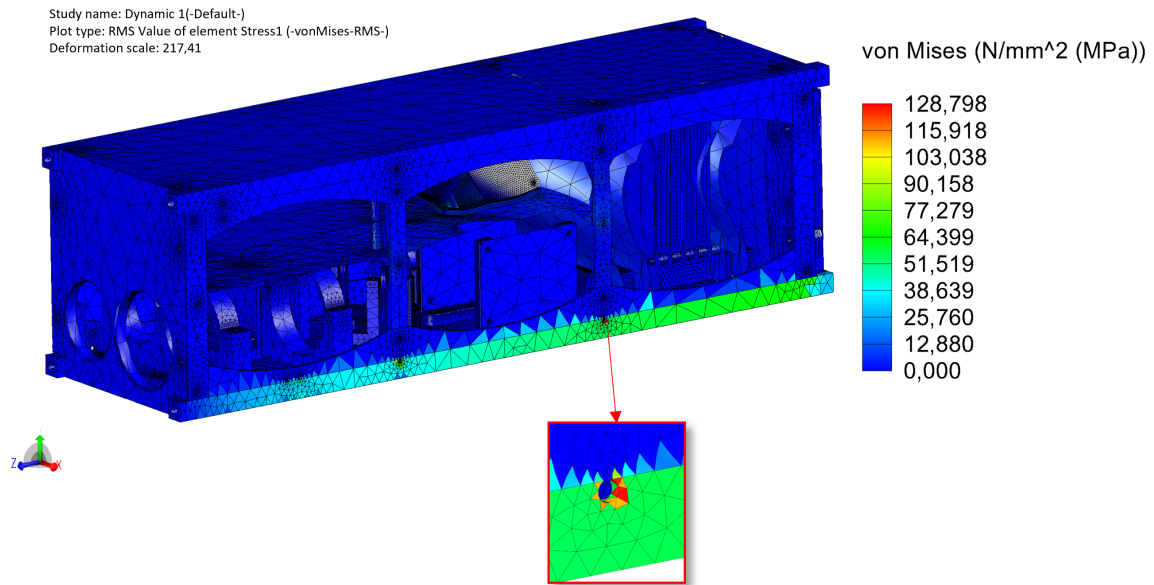


Figure 5.22: CubeSat Random Vibrations loading Z-axis RMS von Mises stress

It's worth noting that the maximum stress value is a root-mean-square value, equivalent to one standard deviation [38]. Consequently, there's a 68% likelihood that the highest RMS von Mises stress remains below 128,79 MPa. Moreover, the value of interest is usually multiplied by 3, signifying that the maximum RMS von Mises stress has a 99,73% chance of being under 386,37 MPa. This provides a safety factor of approximately 1,31.

Figure 5.23 showcases the maximum RMS displacement.

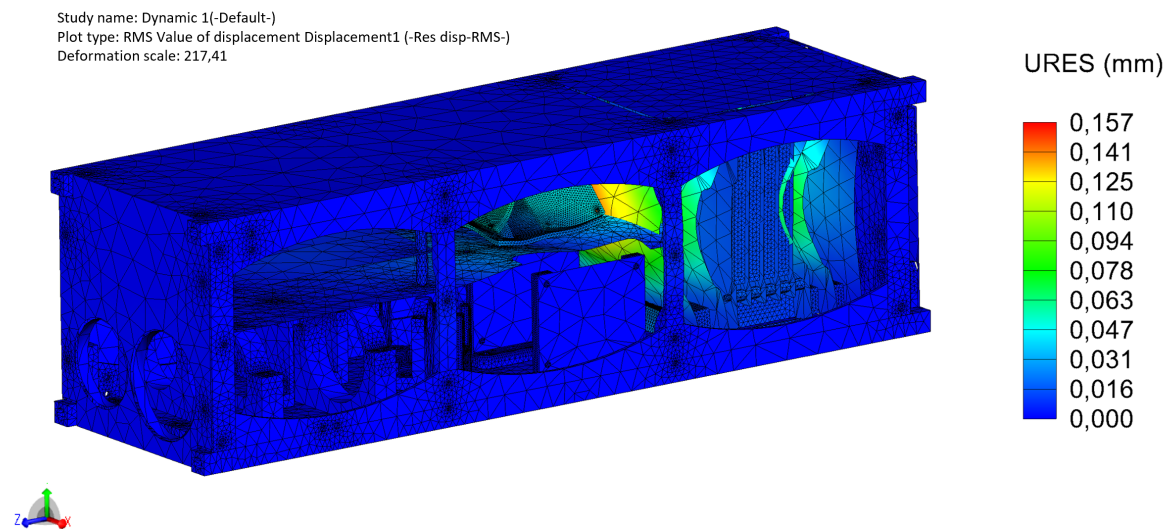


Figure 5.23: CubeSat Random Vibrations loading Z-axis RMS displacement

Based on the analysis conducted, it has been determined that the TTC PCB undergoes a maximum displacement of 0,157 mm. It is highly probable that this value is below the stated amount, with a 68% likelihood. Furthermore, there is an extremely high probability of 99.73% that this displacement is lower than 0,471 mm. However, it should be noted that the presence of stress concentration may affect the reliability of these findings since it was not possible to verify the singularities. To ensure the accuracy of the results, it is necessary to conduct mesh refinements and to simulate the other axes.

6

Conclusions

Contents

6.1	Conclusions	67
6.2	Achievements	68
6.3	Future Work	68

This chapter provides an in-depth analysis of the significant milestones achieved throughout this master's thesis, the challenges encountered, and the main achievements, as well as future work to be done.

6.1 Conclusions

Creating a new CubeSat was an exciting and daunting task, given the multitude of standards and mission requirements that had to be considered. Despite its compact size, the design process for a CubeSat was quite intricate.

This work aims to contribute to the development of a 3U CubeSat with a new quantum communication system, while also utilizing the existing ISTSat-1 mission payload. However, integrating COTS parts not specifically manufactured for CubeSats presented some difficulties. The fiber optic components were not optimized for the CubeSat's size, and the fiber optic cables had trouble connecting each component, leading to several layout revisions. Nonetheless, this design successfully showcased the possibility of using COTS parts for quantum communication in satellites.

The preliminary design phase was a complex and iterative process that required multiple adjustments to incorporate the quantum communication system. The system layout was created per the quantum communication system developed and provided by the Quantum Photonics Laboratory (QuLab) of Instituto de Telecomunicações - Lisboa. Various support structures were designed and customized for the optical system, including the camera, telescope, lasers, and multiple dichroic mirrors crucial to the quantum communication system. New Printed Circuit Boards (PCBs) were developed to accommodate the laser units. The CubeSat underwent several structural analyses, including static, modal, and random vibration analyses.

The CubeSat's preliminary design passed all finite element analyses except for the random vibrations analysis, which could not be accurately assessed due to some limitations on the computational resources. The results obtained for the static analysis, due to quasi-static accelerations, were well below the respective yield stress of the materials, with enough margin to account for potential simplification errors. The modal analysis delivered the lowest fundamental frequency above the minimum required by the LVE in the hard-mounted configuration. The analysis of the Z-axis random vibrations showed that the maximum stress was below the material's yield, and the nearby components were not affected by the resultant displacement.

In this work, the author played a pivotal role in advancing the development of the QuantSat-PT Quantum Communication CubeSat. This groundbreaking project holds the potential to transform the landscape of satellite-based quantum communication. The insights gleaned from this thesis will not only inform subsequent design iterations but will also serve as the cornerstone for an upcoming scientific

publication.

6.2 Achievements

Below are the main achievements of this thesis:

- Developed the preliminary design of a 3U CubeSat for Quantum Communication;
- Established a FE model to perform Static, Modal and Random Vibrations analysis;
- The FE analysis showed that the CubeSat meets the launch authority and the CDS requirements for static loads and minimum fundamental frequency;

6.3 Future Work

It is crucial to focus on the following topics:

- Accurate the current FE model, and include fasteners preloads in all analyses;
- Revise the random vibrations and assess if the qualification level is achieved;
- Conduct a thermoelastic deformation study to assess the deformation caused by the shifts in temperature due to direct sun or earth shadow;
- Perform thermal analysis to find out if the components of the quantum communication system and others survive in operation;
- Verify and assess the ADCS system performance with the current reaction wheels configuration;
- Finally, manufacture a prototype and proceed with experimental tests;

Bibliography

- [1] Wikipedia contributors, "Quantum key distribution — Wikipedia, the free encyclopedia," 2023, [Online; accessed 10-September-2023]. [Online]. Available: https://en.wikipedia.org/w/index.php?title=Quantum_key_distribution&oldid=1170117256
- [2] A. S. Gillis, "What is quantum key distribution (qkd) and how does it work?" Nov 2022, [Online; accessed 28-August-2023]. [Online]. Available: <https://www.techtarget.com/searchsecurity/definition/quantum-key-distribution-QKD>
- [3] B. H. Imran Khan, "Satellite-based qkd," Jan 2018, [Online; accessed 28-August-2023]. [Online]. Available: https://www.optica-opn.org/home/articles/volume_29/february_2018/features/satellite-based_qkd/
- [4] L. Knips, M. Auer, A. Baliuka, O. Bayraktar, P. Freiwang, M. Grünefeld, R. Haber, N. Lemke, C. Marquardt, F. Moll, and et al., "Qube – towards quantum key distribution with small satellites," Jun 2022.
- [5] M. Hutterer, M. Auer, A. Baliuka, C. Marquardt, H. Weinfurter, M. Gall, K. Günther, F. Moll, C. Papadopoulos, J. Pudielko, B. Rödiger, C. Roubal, J. Scharnagl, K. Schilling, and C. Schmidt, "Qube-ii - quantum key distribution with a cubesat," 09 2022.
- [6] E. Kerstel, A. Gardelein, M. Barthelemy, Y. Gilot, E. LeCoarer, J. Rodrigo, T. Sequies, V. Borne, G. Bourdarot, A. Christidis, J. Segura, B. Boulanger, V. Boutou, M. Bouzat, M. Chabanol, L. Fesquet, H. Fourati, M. Moulin, J.-M. Niot, R. P. Bastos, B. Robu, E. Rolland, S. Toru, M. Fink, S. K. Joshi, and R. Ursin, "Nanobob: A cubesat mission concept for quantum communication experiments in an uplink configuration," 2017.
- [7] K. Nozik, "Moving data at the speed of light," Oct 2017, [Online; accessed 2-September-2023]. [Online]. Available: <https://apogeospatial.com/moving-data-at-the-speed-of-light/>
- [8] Wikipedia contributors, "Sputnik 1 — Wikipedia, the free encyclopedia," 2023, [Online; accessed 10-September-2023]. [Online]. Available: https://en.wikipedia.org/w/index.php?title=Sputnik_1&oldid=1174553814

- [9] D. Williams, "Nasa - sputnik 1 - spacecraft - details," [Online; accessed 10-September-2023]. [Online]. Available: <https://nssdc.gsfc.nasa.gov/nmc/spacecraft/display.action?id=1957-001B>
- [10] "Design of the first artificial satellite of the earth," [Online; accessed 10-December-2023]. [Online]. Available: https://www.russianspaceweb.com/sputnik_design.html
- [11] "Bryantech - smallsats by the numbers 2022," [Online; accessed 11-September-2023]. [Online]. Available: https://brycetech.com/reports/report-documents/Bryce_SmallSats_2022.pdf
- [12] CalPoly, "Cubesat design specification rev 14.1, september 2022," [Online; accessed 12-September-2023]. [Online]. Available: <https://static1.squarespace.com/static/5418c831e4b0fa4ecac1bacd/t/62193b7fc9e72e0053f00910/1645820809779/CDS+REV14.1+2022-02-09.pdf>
- [13] E. Kulu, "Nanosats database," [Online; accessed 10-September-2023]. [Online]. Available: <https://www.nanosats.eu/>
- [14] "Satélite istsat-1 já construído," [Online; accessed 1-October-2023]. [Online]. Available: <https://www.idmec.tecnico.ulisboa.pt/2023/06/07/satellite-istsat-1-ja-construido/>
- [15] V. Galetsky and M. Niehus, "Leo small satellite qkd downlink performance: Quantsat-pt case study," 2022.
- [16] "Istsat-1," [Online; accessed 1-October-2023]. [Online]. Available: <http://istsat-one.tecnico.ulisboa.pt/~istsat-one.daemon/>
- [17] F. P. Beer, E. R. Johnston, J. T. DeWolf, and D. F. Mazurek, *Mechanics of Materials*. McGraw-Hill Education, 2020.
- [18] S. S. Rao, *Mechanical vibrations in SI units*. Pearson Education Limited, 2018.
- [19] P. M. Kurowski, *Finite Element Analysis for Design Engineers*. SAE International, 2023.
- [20] P. R. Childs, "Chapter 16 - fastening and power screws," in *Mechanical Design Engineering Handbook*, P. R. Childs, Ed. Oxford: Butterworth-Heinemann, 2014, pp. 677–719. [Online]. Available: <https://www.sciencedirect.com/science/article/pii/B9780080977591000162>
- [21] NASA, *State-of-the-Art Small Spacecraft Technology*, 2021, [Online; accessed 10-September-2023]. [Online]. Available: https://www.nasa.gov/sites/default/files/atoms/files/soa_2021.pdf
- [22] "Anisoprint - 3d printed cubesat frames," Oct 2022, [Online; accessed 15-September-2023]. [Online]. Available: <https://anisoprint.com/cases/3d-printed-cubesat-frames-space-ready-satellites-from-carbon-fiber/>

- [23] "Pumpkin cubesat kit -1u," 2023, [Online; accessed 10-September-2023]. [Online]. Available: <https://www.pumpkinspace.com/uploads/8/2/6/7/82676946/published/cubesatkit-1u-revd-skeletonx1000x1000.jpg?1490978150>
- [24] "Endurosat cubesat kit," 2023, [Online; accessed 10-September-2023]. [Online]. Available: <https://www.endurosat.com/wp-content/uploads/2017/05/3u-cubesat-structure-nanosat-endurosat-2022-1-min.webp>
- [25] A. Harish, "Why the tacoma narrows bridge collapsed," Jun 2023, [Online; accessed 15-September-2023]. [Online]. Available: <https://www.simscale.com/blog/tacoma-narrows-bridge-collapse/>
- [26] NASA, "General environmental verification standard (GEVS) -NASA," [Online; accessed 20-September-2023]. [Online]. Available: https://standards.nasa.gov/sites/default/files/standards/GSFC/B/0/gsfsc-std-7000b_signature_cycle_04_28_2021_fixed_links.pdf
- [27] "Mechanical and Material Requirements for Metric Externally Threaded Steel Fasteners," SAE International, Standard, Mar. 2013.
- [28] R. Lagier, "Ariane 6 user's manual for multi-launch service," [Online; accessed 10-September-2023]. [Online]. Available: <https://smallsats.arianespace.com/assets/globals/MLSs-users-manual.pdf>
- [29] S. M. Arnold, D. Cebon, and M. Ashby, *Materials Selection for Aerospace Systems*, 2012.
- [30] J. Plante and B. Lee, "Environmental conditions for space flight hardware - nasa," 2004. [Online]. Available: <https://nepp.nasa.gov/DocUploads/C5E0869C-0469-4D11-9FAA8012C8F52351/Environmental%20Testing%20Survey.doc>
- [31] D. Barnes, "Optomechanical design, analysis, and testing of the nanosatellite optical downlink experiment," Master's thesis, Massachusetts Institute of Technology, 2018.
- [32] J. Revés, "Attitude determination and control system for the quantsat-pt project," Master's thesis, Instituto Superior Técnico, 2022.
- [33] CubeSpace, "Cubewheel gen 1," [Online; accessed 10-October-2023]. [Online]. Available: <https://www.cubespace.co.za/products/gen-1/actuators/cubewheel/>
- [34] Q. Lam, B. Anderson, and M. Xin, "Preserving spacecraft attitude control accuracy using theta-d controller subject to reaction wheel failures," 04 2010.
- [35] Endurosat, "1u cubesat solar panel x/y," August 2023, [Online; accessed 15-September-2023]. [Online]. Available: <https://www.endurosat.com/cubesat-store/cubesat-solar-panels/1u-solar-panel-x-y/>

- [36] NESC, “Lessons learned from evaluation of loctite® as a secondary locking feature for iss fasteners,” Feb 2013, [Online; accessed 15-October-2023]. [Online]. Available: <https://lis.nasa.gov/lesson/6937>
- [37] L. d. P. S. de Sá, “Modelling and Validation of Finite Elements Structural Analysis of ISTSat-1,” Master’s thesis, Instituto Superior Técnico, 2021.
- [38] P. M. Kurowski, *Vibration Analysis with SolidWorks Simulation 2022*. SDC Publications, 2022.



Static analysis negative orientation

(-x,-y,-z)

Model name: CubeSat 3U Quantum communication - Simulation - Simplified
Study name: Static - minus X axis(-Default-)
Plot type: Static nodal stress Stress1 (-vonMises-)
Deformation scale: 902,117

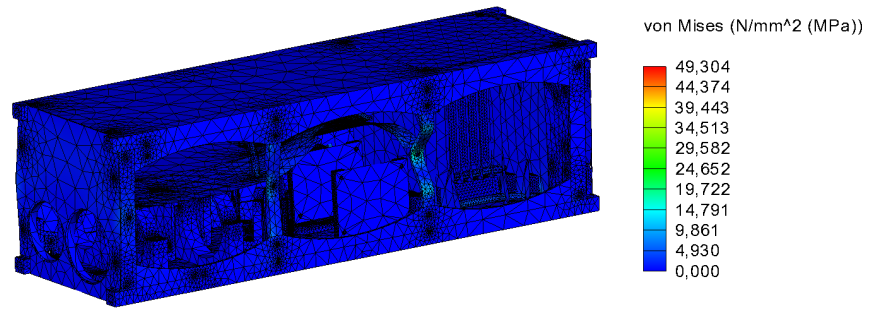


Figure A.1: CubeSat Static loading -X-axis von Mises stress

Model name: CubeSat 3U Quantum communication - Simulation - Simplified
Study name: Static - minus X axis(-Default-)
Plot type: Static displacement Displacement1 (-Res disp-)
Deformation scale: 902,117

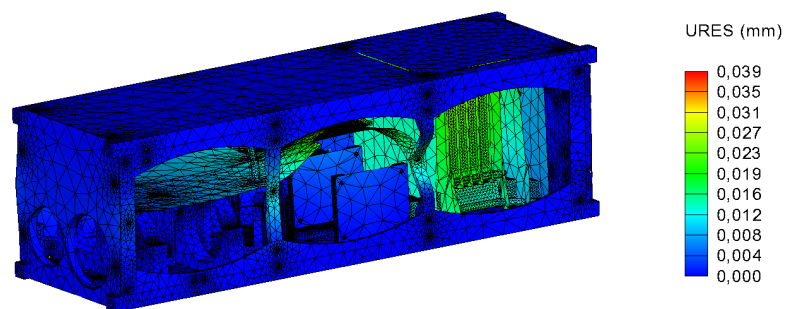


Figure A.2: CubeSat Static loading -X-axis displacement

Model name: CubeSat 3U Quantum communication - Simulation - Simplified
Study name: Static - minus Y axis(-Default-)
Plot type: Static nodal stress Stress1 (-vonMises-)
Deformation scale: 498,395

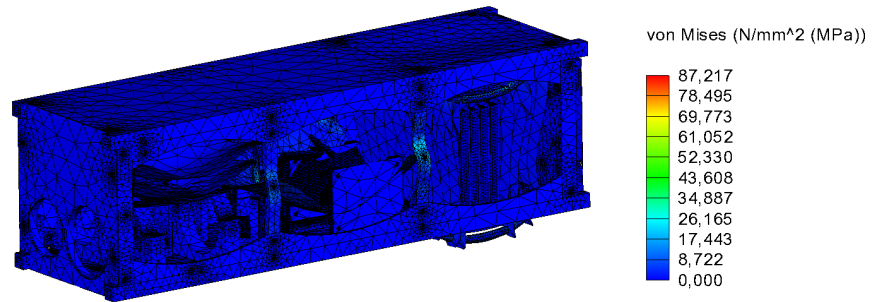


Figure A.3: CubeSat Static loading -Y-axis von Mises stress

Model name: CubeSat 3U Quantum communication - Simulation - Simplified
Study name: Static - minus Y axis(-Default-)
Plot type: Static displacement Displacement1 (-Res disp-)
Deformation scale: 498,395

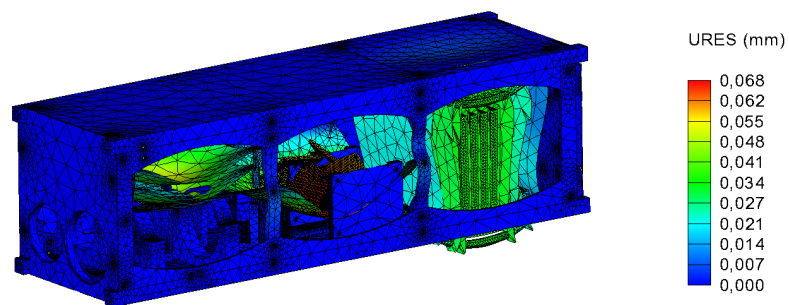


Figure A.4: CubeSat Static loading -Y-axis displacement

Model name: CubeSat 3U Quantum communication - Simulation - Simplified
Study name: Static 6 - minus Z axis(-Default-)
Plot type: Static nodal stress Stress1 (-vonMises-)
Deformation scale: 614,926

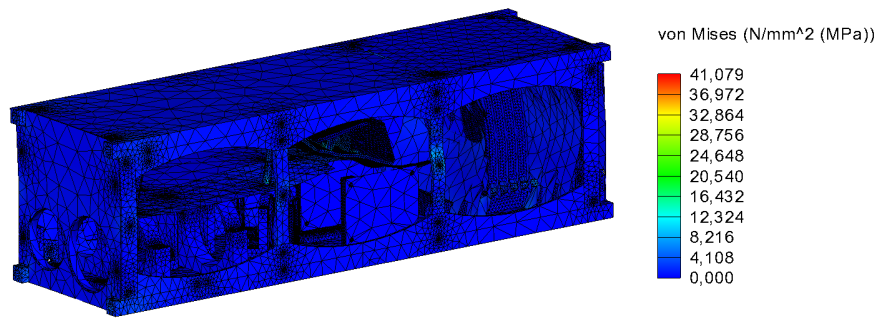


Figure A.5: CubeSat Static loading -Z-axis von Mises stress

Model name: CubeSat 3U Quantum communication - Simulation - Simplified
Study name: Static 6 - minus Z axis(-Default-)
Plot type: Static displacement Displacement1 (-Res disp-)
Deformation scale: 614,926

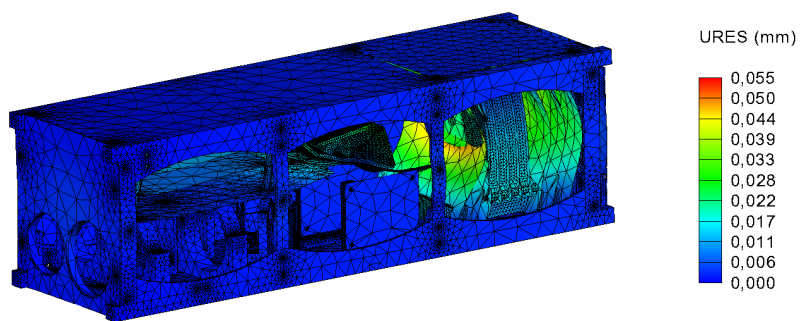


Figure A.6: CubeSat Static loading -Z-axis displacement

B

Modes - Hard mounted

Model name: CubeSat 3U Quantum communication - Simulation - Simplified
Study name: Frequency 6 (Default-)
Plot type: Frequency Amplitude2 (-Res Amp - Mode Shape 2-)
Mode Shape :2. Value = 310,69 Hz
Deformation scale: 0,0075

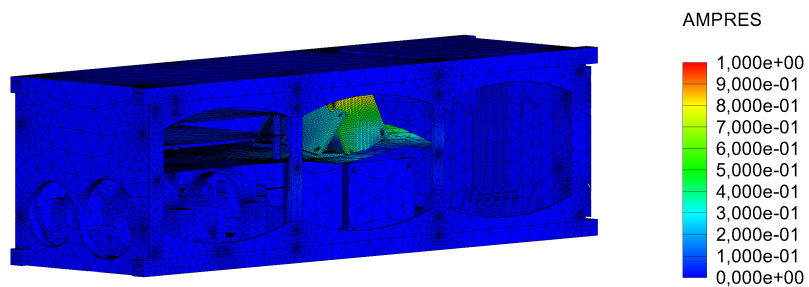


Figure B.1: Mode 2 - 310,69 Hz

Model name: CubeSat 3U Quantum communication - Simulation - Simplified
Study name: Frequency 6(-Default-)
Plot type: Frequency Amplitude3 (-Res Amp - Mode Shape 3-)
Mode Shape :3 Value = 318,5 Hz
Deformation scale: 0,0075

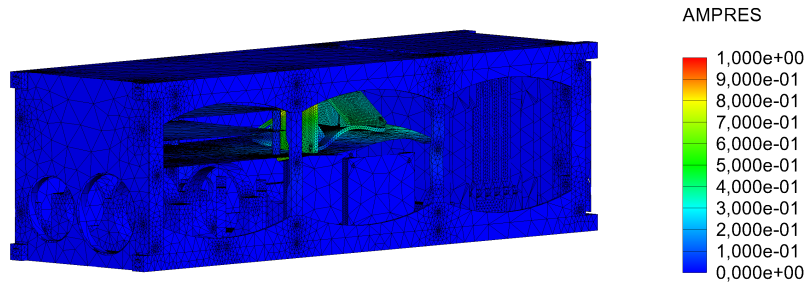


Figure B.2: Mode 3 - 318,50 Hz

Model name: CubeSat 3U Quantum communication - Simulation - Simplified
Study name: Frequency 6(-Default-)
Plot type: Frequency Amplitude4 (-Res Amp - Mode Shape 4-)
Mode Shape :4 Value = 330,85 Hz
Deformation scale: 0,0075

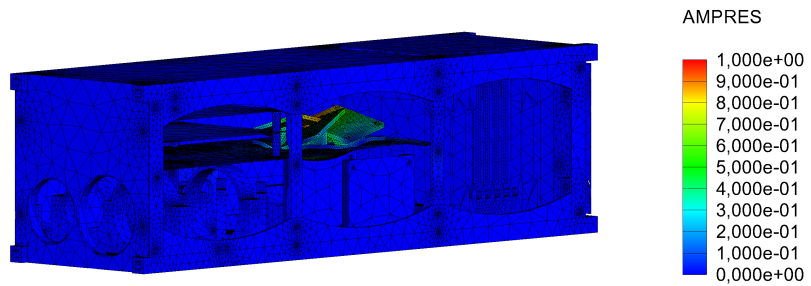


Figure B.3: Mode 4 - 330,85 Hz

Model name: CubeSat 3U Quantum communication - Simulation - Simplified
Study name: Frequency 6(-Default-)
Plot type: Frequency Amplitude5 (-Res Amp - Mode Shape 5-)
Mode Shape :5 Value = 344,44 Hz
Deformation scale: 0,0075

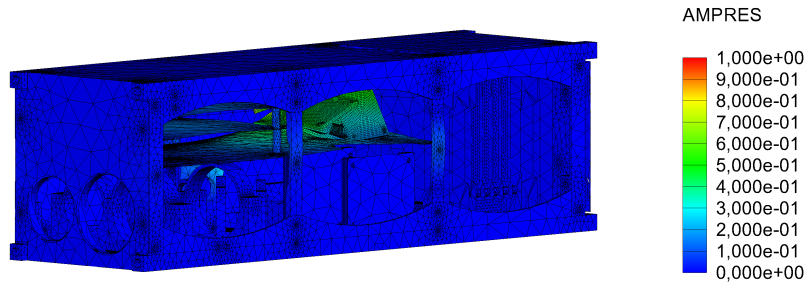


Figure B.4: Mode 5 - 344,44 Hz

Model name: CubeSat 3U Quantum communication - Simulation - Simplified
Study name: Frequency 6(-Default-)
Plot type: Frequency Amplitude6 (-Res Amp - Mode Shape 6-)
Mode Shape :6 Value = 377,49 Hz
Deformation scale: 0,0075

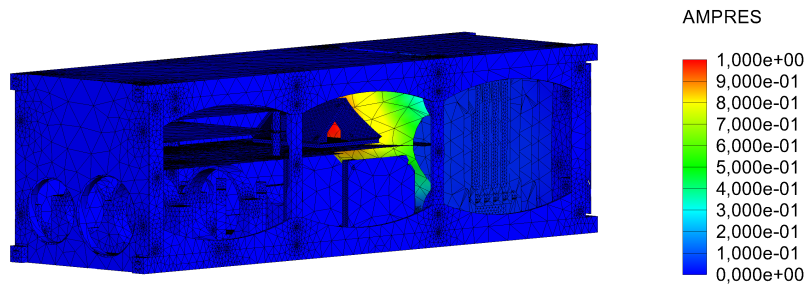


Figure B.5: Mode 6 - 377,49 Hz

Model name: CubeSat 3U Quantum communication - Simulation - Simplified
Study name: Frequency 6(-Default-)
Plot type: Frequency Amplitude7 (-Res Amp - Mode Shape 7-)
Mode Shape :7 Value = 399,52 Hz
Deformation scale: 0,0075

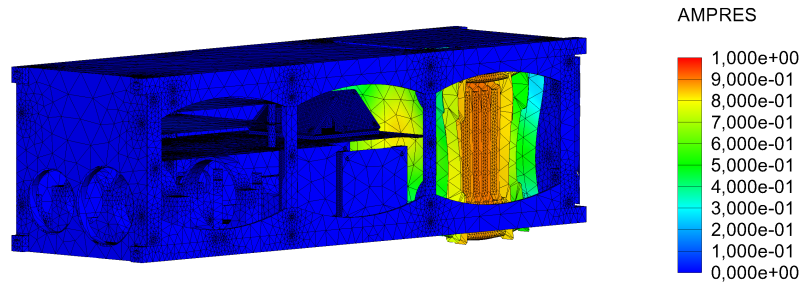


Figure B.6: Mode 7 - 399,52 Hz

Model name: CubeSat 3U Quantum communication - Simulation - Simplified
Study name: Frequency 6(-Default-)
Plot type: Frequency Amplitude8 (-Res Amp - Mode Shape 8-)
Mode Shape :8 Value = 401,54 Hz
Deformation scale: 0,00433495

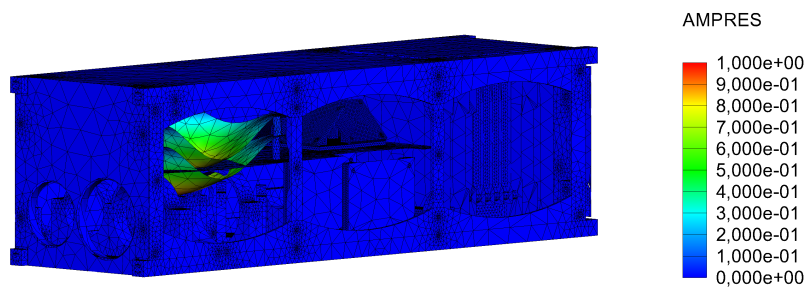


Figure B.7: Mode 8 - 401,54 Hz

Model name: CubeSat 3U Quantum communication - Simulation - Simplified
Study name: Frequency 6(-Default-)
Plot type: Frequency Amplitude9 (-Res Amp - Mode Shape 9-)
Mode Shape : 9 Value = 415,78 Hz
Deformation scale: 0,00421464

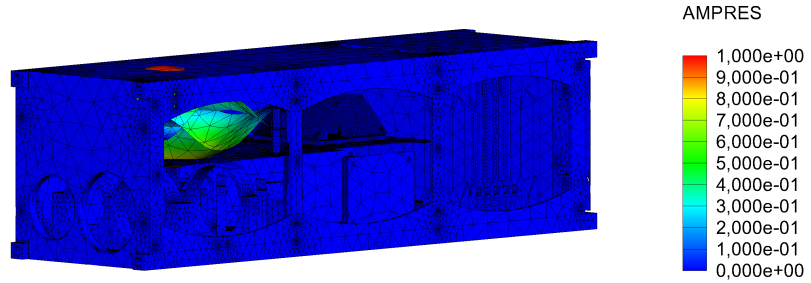


Figure B.8: Mode 9 - 415,78 Hz

Model name: CubeSat 3U Quantum communication - Simulation - Simplified
Study name: Frequency 6(-Default-)
Plot type: Frequency Amplitude10 (-Res Amp - Mode Shape 10-)
Mode Shape : 10 Value = 493,29 Hz
Deformation scale: 0,00540867

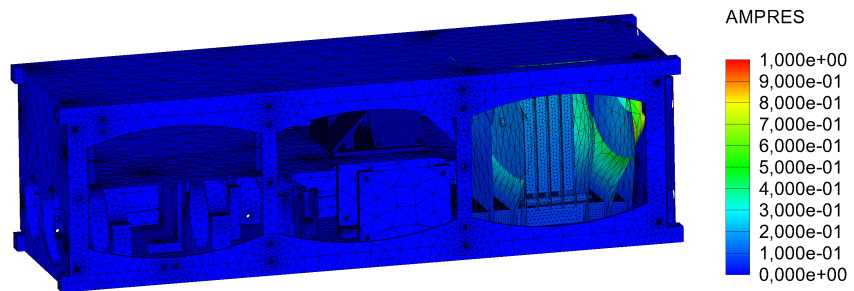


Figure B.9: Mode 10 - 493,29 Hz

Model name: CubeSat 3U Quantum communication - Simulation - Simplified
Study name: Frequency 6(-Default-)
Plot type: Frequency Amplitude11 (-Res Amp - Mode Shape 11-)
Mode Shape : 11 Value = 496,92 Hz
Deformation scale: 0,00958685

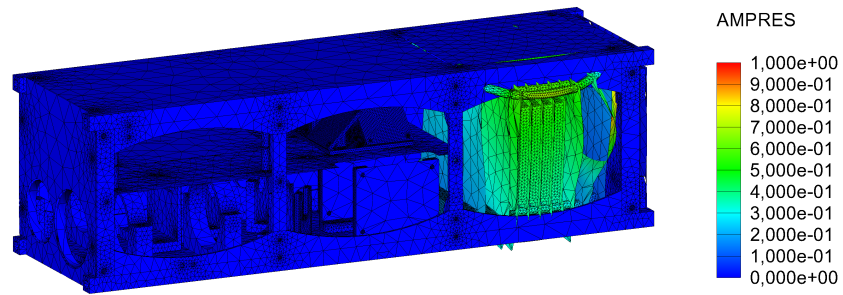


Figure B.10: Mode 11 - 496,92 Hz

Model name: CubeSat 3U Quantum communication - Simulation - Simplified
Study name: Frequency 6(-Default-)
Plot type: Frequency Amplitude12 (-Res Amp - Mode Shape 12-)
Mode Shape : 12 Value = 500,3 Hz
Deformation scale: 0,0162143

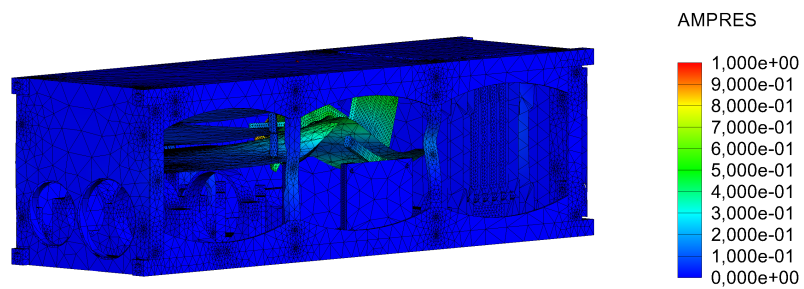


Figure B.11: Mode 12 - 500,30 Hz

Model name: CubeSat 3U Quantum communication - Simulation - Simplified
Study name: Frequency 6(-Default-)
Plot type: Frequency Amplitude13 (-Res Amp - Mode Shape 13-)
Mode Shape :13 Value = 504,81 Hz
Deformation scale: 0,00464311

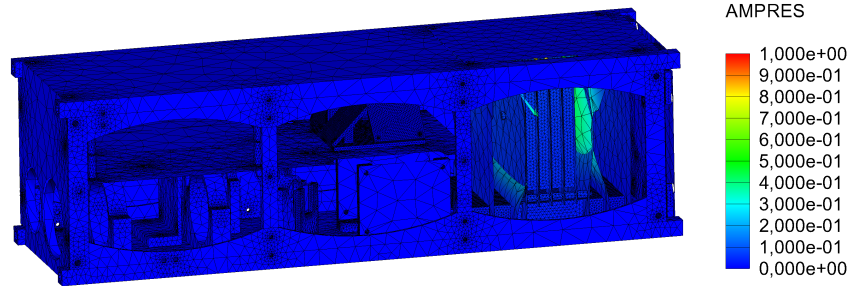


Figure B.12: Mode 13 - 504,81 Hz

Model name: CubeSat 3U Quantum communication - Simulation - Simplified
Study name: Frequency 6(-Default-)
Plot type: Frequency Amplitude14 (-Res Amp - Mode Shape 14-)
Mode Shape :14 Value = 515,87 Hz
Deformation scale: 0,00449224

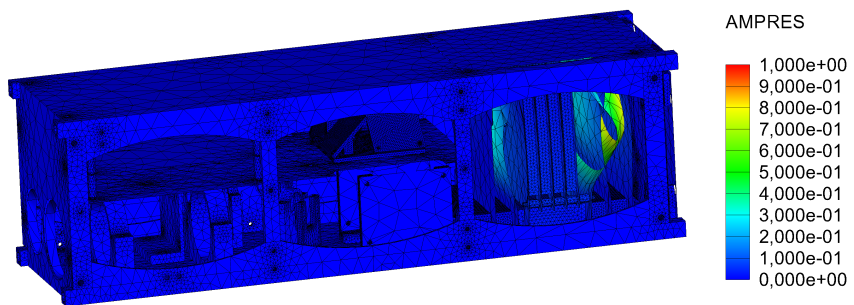


Figure B.13: Mode 14 - 515,87 Hz

Model name: CubeSat 3U Quantum communication - Simulation - Simplified
Study name: Frequency 6(-Default-)
Plot type: Frequency Amplitude15 (-Res Amp - Mode Shape 15-)
Mode Shape : 15 Value = 523,39 Hz
Deformation scale: 0,0177696

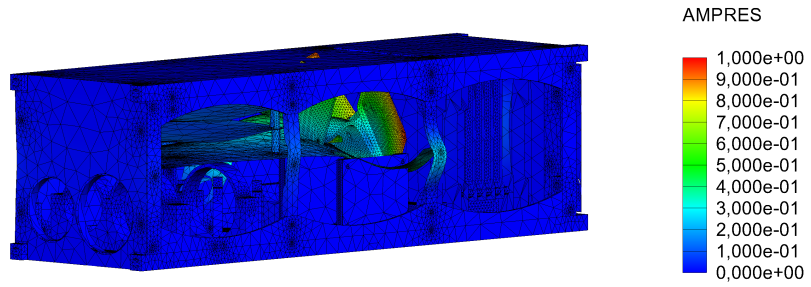
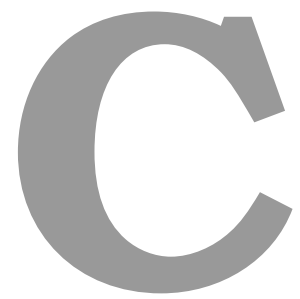


Figure B.14: Mode 15 - 523,39 Hz



Remote loads

Table C.1: Remote loads

Remote load 1 - Reaction Wheel						Remote load 6 - EOPM							
Location	Moment of Inertia ($kg.m^2$)				Mass (kg)	Location	Moment of Inertia ($kg.m^2$)				Mass (kg)		
X	10,88	Lxx	9,82E-06	Lxy	6,00E-08	0,060	X	-30,71	Lxx	1,69E-06	Lxy	0,00E+00	0,013
Y	28,39	Lyy	1,01E-05	Lyz	-4,20E-07		Y	7,25	Lyy	1,74E-06	Lyz	1,00E-08	
Z	14,67	Lzz	1,03E-05	Lxz	6,00E-08		Z	72,89	Lzz	7,00E-08	Lxz	-9,00E-08	
Remote load 2 - Reaction Wheel						Remote load 7 - Camera							
Location	Moment of Inertia ($kg.m^2$)				Mass (kg)	Location	Moment of Inertia ($kg.m^2$)				Mass (kg)		
X	26,08	Lxx	1,03E-05	Lxy	-4,20E-07	0,060	X	-23,51	Lxx	2,78E-05	Lxy	-2,00E-08	0,180
Y	28,39	Lyy	1,01E-05	Lyz	-6,00E-08		Y	-21,54	Lyy	2,77E-05	Lyz	5,00E-08	
Z	-22,29	Lzz	9,82E-06	Lxz	-6,00E-08		Z	120,67	Lzz	9,81E-06	Lxz	2,00E-08	
Remote load 3 - Reaction Wheel						Remote load 8 - Telescope							
Location	Moment of Inertia ($kg.m^2$)				Mass (kg)	Location	Moment of Inertia ($kg.m^2$)				Mass (kg)		
X	-10,88	Lxx	9,82E-06	Lxy	-6,00E-08	0,060	X	18	Lxx	1,10E-05	Lxy	0,00E+00	0,180
Y	28,39	Lyy	1,01E-05	Lyz	4,20E-07		Y	-21,5	Lyy	1,10E-05	Lyz	0,00E+00	
Z	-37,49	Lzz	1,03E-05	Lxz	6,00E-08		Z	113,75	Lzz	4,43E-06	Lxz	0,00E+00	
Remote load 4 - Reaction Wheel						Remote load 9 - Collimator							
Location	Moment of Inertia ($kg.m^2$)				Mass (kg)	Location	Moment of Inertia ($kg.m^2$)				Mass (kg)		
X	-26,08	Lxx	1,03E-05	Lxy	4,20E-07	0,060	X	-31	Lxx	4,32E-06	Lxy	0,00E+00	0,026
Y	28,39	Lyy	1,01E-05	Lyz	6,00E-08		Y	-19,66	Lyy	3,88E-06	Lyz	-1,20E-07	
Z	-0,53	Lzz	9,82E-06	Lxz	-6,00E-08		Z	-23	Lzz	2,04E-06	Lxz	0,00E+00	
Remote load 5 - EOAM													
Location	Moment of Inertia ($kg.m^2$)				Mass (kg)								
X	25,85	Lxx	6,00E-06	Lxy	0,00E+00	0,013							
Y	10,06	Lyy	6,13E-06	Lyz	0,00E+00								
Z	70,3	Lzz	2,90E-07	Lxz	2,00E-08								

D

Technical drawing

